Characterization of the Structures of Small Peptides and their Interactions with Inorganic Minerals

Erika Louise Buckle

A dissertation

submitted in partial fulfillment of the

requirements for the degree of

Doctor of Philosophy

University of Washington

2018

Reading Committee:

Gary Drobny, Chair

Niels Andersen

Robert Synovec

Program Authorized to Offer Degree:

Chemistry

University of Washington

Abstract

Characterization of the Structures of Small Peptides and their Interactions with Inorganic Minerals

Erika Louise Buckle

Chair of the Supervisory Committee:
Professor Gary Drobny
Department of Chemistry

Proteins mediate the nucleation and growth of many biominerals, yet the specifics of these protein-mineral interactions are often poorly understood. The focus of this dissertation is to better understand these interactions via small peptide systems. The approach to this problem is multifaceted; peptide-mineral interactions are explored through various biomineralization systems and through surface adsorption. The biomineralization studies begin with R5, a well-studied biosilicification peptide that can produce uniform nanostructures of both silica (SiO_2) and titania (TiO_2). Then, model serine-lysine (S-K) peptides are investigated to further the understanding of biomimetic TiO_2 formation. Surface adsorption studies are focused on the structure of SNa15, a mutated fragment of statherin (a salivary protein) as a function of mineral surface: hydroxyapatite (HAP), SiO_2, and TiO_2. Solid-state NMR (ssNMR) experiments used in

the investigation of R5, the S-K peptides, and SNa15 are detailed here. 1D ^{13}C CP MAS, 1D ^{15}N CP MAS, and 2D ^{13}C-^{13}C DARR experiments are utilized, resulting in peptide structures for both the neat and mineral-complexed forms. Furthermore, side-chain chemical shifts are used to assess the degree to which various residues are in close proximity to the mineral phases.

TABLE OF CONTENTS

LIST OF FIGURES

LIST OF TABLES

List of Abbreviations

CP: Cross-polarization

CS: Chemical Shift

CSA: Chemical Shift Anisotropy

ΔCS: Perturbation of Chemical Shift

DARR: Dipolar Assisted Rotational Resonance

DFT: Density Functional Theory

DLS: Dynamic Light Scattering

DNP: Dynamic Nuclear Polarization

FMOC: Fluorenylmethoxycarbonyl

HAP: Hydroxyapatite

HCl: Hydrochloric acid

HETCOR: Heteronuclear Correlation

ICP-OES: Inductively Coupled Plasma- Optical Emission Spectrometry

KSSKK-TiO_2: KSSKK embedded within the titania co-precipitate

NEXAFS: Near Edge X-Ray Absorption Fine Structure

MAS: Magic Angle Spinning

PD: Poly-L-aspartic acid

PG: Poly-L-glutamic acid

PLL: Poly-L-lysine

R5-SiO_2: R5 embedded within the silica co-precipitate

R5-TiO_2: R5 embedded within the titania co-precipitate

REDOR: Rotational Echo Double Resonance

RF: Radio Frequency

RP-HPLC: Reverse Phase- High-performance Liquid Chromatography

SEM: Scanning Electron Microscopy

SFG: Sum Frequency Generation

SKSK$_3$SKS-TiO$_2$: SKSK$_3$SKS embedded within the titania co-precipitate

SNa15-HAP: SNa15 adsorbed onto the hydroxyapatite surface

SNa15-SiO$_2$: SNa15 adsorbed onto the silica surface

SNa15-TiO$_2$: SNa15 adsorbed onto the titania surface

ssNMR: Solid-state Nuclear Magnetic Resonance

TBP: Titanium binding peptide

TiBALDH: Titanium bis(ammonium lactato)dihydroxide

TFA: Trifluoroacetic acid

TIS: Triisopropylsilane

TMS: Tetramethylsilane

UV: Ultraviolet

ACKNOWLEDGEMENTS

First and foremost, I would like to thank my advisor, Dr. Gary Drobny, for being a great mentor and for his interest in my research projects, education, and career goals. I would also like to thank all of the members of the Drobny group for their support and encouragement throughout the years, especially Dr. Adrienne Roehrich, Dr. Prashant Emani, Dr. Stephen Davidowski, and Rachel Gebhart.

I would like to give a huge thank-you to all my friends for supporting me through the difficult times and for celebrating my successes with me. A special thanks to Dr. David Pinkerton, who kept me sane during graduate school; I feel very lucky to know you and to call you one of my best friends. And Thom, there are not enough words to describe how much I appreciate you. Thank you for your continued love and support.

I would also like to thank my parents and my sister for always being there for me. You taught me to pursue my passions and encouraged me to continue when that seemed too difficult. I am lucky to have such great role models, and I could not be where I am today without you.

Chapter 1. INTRODUCTION[1]

1.1 BIOMINERALIZATION.

Inorganic minerals, such as silica (SiO_2) and titania (TiO_2), are versatile materials with widespread applications including use as pigments, insulators, textile coatings, catalysts, medical devices, and solar cell components. [1–10] Each specific application requires a uniquely tuned set of physical properties for the material, such as particle size, crystallinity, and morphology. However, the anthropogenic synthesis of such minerals often requires extreme temperature, pressure, and pH, while maintaining limited control over crystallinity and morphology.[11–15] Hence, new synthetic routes that allow for more fine-tuned control are necessary.

In contrast to synthetic methods, many biological organisms produce inorganic materials, such as bone, teeth, exoskeletons, and shells, through a process known as biomineralization. Specialized proteins are commonly used to direct mineral formation with precise control over the size, structure, and morphology all under ambient temperature and biological pH. Understanding the molecular mechanisms involved in biomineralization processes may aid in the discovery of novel synthetic routes for the production of complex inorganic materials.

Diatoms are a unicellular microalgae that produce SiO_2 under mild conditions from the precursor silicic acid, resulting in material of tailored size and structure.[16–22] One of the most widely studied silicifying organisms is the marine diatom *Cylindrotheca fusiformis.* The protein implicated in regulating the process of SiO_2 biomineralization is silaffin sil1p, shown in Figure

---

[1] Portions of this chapter have been adapted from (1) Buckle, E.L.; Roehrich, A.; Vandermoon, B.; Drobny, G.P. Comparative Study of Secondary Structure and Interactions of the R5 Peptide in Silicon Oxide and Titanium Oxide Coprecipitates Using Solid-State NMR Spectroscopy. *Langmuir* **2017**, 33 (40), 10517-10524. and (2) Buckle, E.L.; Lum, J.; Roehrich, A.; Stote, R.; Vandermoon, B.; Dracinsky, M.; Filocamo, S.; Drobny, G.P. Serine-Lysine Peptides as Mediators for the Production of Titanium Dioxide: Investigating the Effects of Primary and Secondary Structure Using Solid-State NMR Spectroscopy and DFT Calculations. *J. Phys. Chem. B.* Manuscript JP-2018-00745p, *currently submitted.*

1.1. The primary structure of sil1p has a repetitive peptide sequence between residues 108 and 271, composed of seven units.[21] The fifth of these repeating units, a 19 amino acid peptide known as R5 (SSKKSGSYSGSKGSKRRIL), has the ability to precipitate SiO_2 nanospheres in a manner similar to its parent silaffin (sillafin-1A) without the need for post-translational modifications.[21] Figure 1.2 shows SEM images of SiO_2 precipitates formed with silaffin-1A (Figure 1.2a) and R5 (Figure 1.2b).

								M	K	L	T	A	I	F	P	L	L	F	T				12
	A	V	G	Y	C	A	A	Q	S	I	A	D	L	A	A	A	N	L	S				31
	T	E	D	S	K	S	A	Q	L	I	S	A	D	S	S	D	D	A	S				50
	D	S	S	V	E	S	V	D	A	A	S	S	D	V	S	G	S	S	V				69
	E	S	V	D	V	S	G	S	S	L	E	S	V	D	V	S	G	S	S				88
	L	E	S	V	D	D	S	S	E	D	S	E	E	E	E	L	R	I	L				107
R1	S	S	K	K	S	G	S	Y	Y	S	Y	G	T	K	K								122
					S	G	S	Y	S	G	Y	S	T	K	K	S	A	S	R	R	I	L	140
R2	S	S	K	K	S	G	S	Y	S	G	Y	S	T	K	K	S	G	S	R	R	I	L	162
R3	S	S	K	K	S	G	S	Y	S	G	S	K	G	S	K	R	R	I	L				181
R4	S	S	K	K	S	G	S	Y	S	G	S	K	G	S	K	R	R	N	L				200
R5	S	S	K	K	S	G	S	Y	S	G	S	K	G	S	K	R	R	I	L				219
R6	S	S	K	K	S	G	S	Y	S	G	S	K	G	S	K	R	R	N	L				238
R7	S	S	K	K	S	G	S	Y	S	G	S	K	G	S	K	R	R	I	L				257
	S	G	G	L	R	G	S	M															265

Figure 1.1. The primary structure of sil1p. The sequence is depicted in a way to emphasize residue homology. The repeats within residues 108-271 are labeled R1 to R7, and are indicated by the red box. The R5 fragment is shown in red. Adapted from Kröger, Deutzmann, and Sumper.[19]

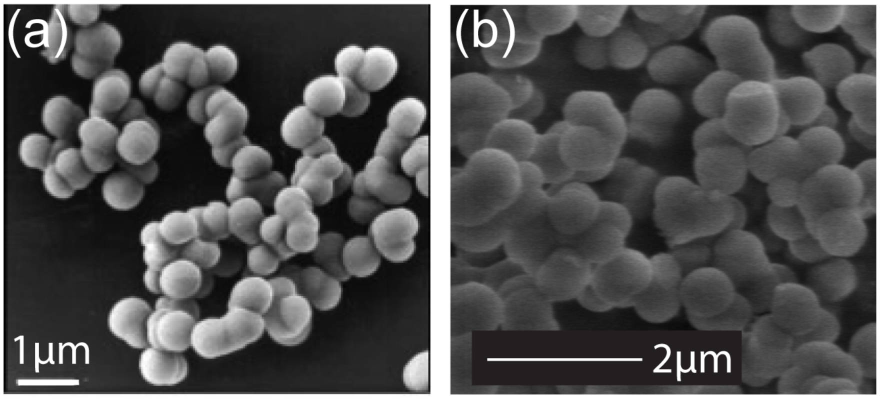

Figure 1.2. SEM images of SiO_2 precipitated by (a) silaffin-1A (adapted from Kröger, Deutzmann, and Sumper[19]) and (b) R5[23]. Protein and peptide concentration are 5 mg/ml.

Much of the literature focuses on silicifying organisms (i.e. diatoms and sponges), identifying proteins involved in biosilicification (i.e. R5), and biotechnological and materials science applications of silicifying proteins and the resultant SiO_2 material.[16,19,20,24–31] There are some atomic-level studies of silicifying peptides, LKα14 for example, but to a lesser extent.[32] This thesis builds on these atomic-level studies while focusing on not only biomimetic SiO_2 formation, but also biomimetic TiO_2 formation. The role of R5 in both SiO_2 and TiO_2 formation will be investigated in Chapter 2, focusing on molecular-level interactions, such as secondary structural changes and peptide side-chain interactions. Various serine-lysine (S-K) peptides are designed and tested for TiO_2-precipitating activity in Chapter 3, and two of these peptides are also investigated on a molecular level.

1.2 SURFACE ADSORPTION.

Molecular interactions at the organic-inorganic interface determine important behaviors, such as protein adsorption onto mineral surfaces and cell adhesion to biomaterials (i.e. medical implant devices). These protein-mineral interfaces are quite complex, and, despite their importance, are poorly understood at a molecular and mechanistic level. An improved understanding of how proteins recognize and adhere to mineral surfaces could provide insight into the improvement of biomaterials and biocompatibility.

The growth of biominerals (i.e. bone, teeth, and shells) is controlled by specialized proteins. Many of the proteins that are involved in biomineral nucleation and growth contain an abundance of acidic residues, with few exceptions. Statherin, a small 43-residue salivary protein with the sequence DpSpSEEKFLRRIGRFGYGYGPYQPVPEQPLYPQPYQPQYQQYTF, inhibits the precipitation of calcium phosphate minerals and hydroxyapatite (HAP) crystal growth. The N-terminus of statherin contains acidic residues, including phosphoserine (pS), aspartic acid (D), and glutamic acid (E). The first five residues have been shown to be essential for HAP binding.[33] Furthermore, the first 15 residues of statherin, referred to as SN15, show nearly the same binding affinity for HAP, even when the phosphoserine residues are replaced by aspartic acid (SNa15).[33] Statherin has been widely studied and its structure is known neat and adsorbed onto HAP.[33–36] However, SNa15 has been studied far less extensively.

This thesis examines the binding of SNa15 onto hydroxyapatite (HAP), silicon dioxide (SiO_2), and titanium dioxide (TiO_2) in Chapter 5. Binding isotherms are paired with an atomic-level investigation of the binding of SNa15 to each mineral surface. ssNMR is used to elucidate the structure of SNa15 and to probe its interactions with the mineral surfaces.

1.3 SOLID-STATE NMR EXPERIMENTATION.

Solid-state nuclear magnetic resonance (ssNMR) spectroscopy is used to study these proposed systems on an atomic level. Often, proteins and peptides are examined through X-ray crystallography or solution NMR. However, these techniques cannot be used to investigate the structures of mineral-associated peptides. ssNMR, however, is uniquely suited for use in these types of systems and has been used readily to study protein-mineral complexes such as statherin[34–40] and amelogenin[41,42], as well as peptide-mineral complexes such as LKα14[32], pentalysine clusters[43], and titania binding peptide (TBP).[44] This thesis uses ssNMR to study a variety of peptide-mineral complexes. The basics of the experimentation used in this thesis will be discussed below. This thesis will not discuss NMR theory, which can be found in focused texts elsewhere.[45,46]

1.3.1 *Magic-Angle Spinning.*

One of the difficulties posed by ssNMR is broad lineshapes, resulting from orientation-dependent interactions, or anisotropy, and dipolar couplings. In ssNMR, the samples most often studied are powders, which contain molecules with random orientations. The different molecular orientations all result in slightly different spectral frequencies, which overlap and result in broad lines. This lack of resolution renders the data virtually unusable. Therefore, it is necessary to apply techniques to overcome this barrier and to achieve high-resolution spectra.

Magic-angle spinning (MAS) is the solution to this problem; it is routinely used in the majority of ssNMR experiments to remove the line-broadening effects of anisotropy. The basic principles of MAS were discovered by E.R. Andrew.[47] He found that by introducing artificial motion, via spinning the sample at 54.74° with respect to the applied magnetic field, the $(3\cos^2\theta-1)$ term in the dipolar coupling Hamiltonian averages out to zero, reducing line broadening.[46,47] The chemical shift anisotropy (CSA) averages out to a non-zero term, reducing its effects, yet some line-broadening still remains. Figure 1.3 shows the basic set-up of an MAS experiment.

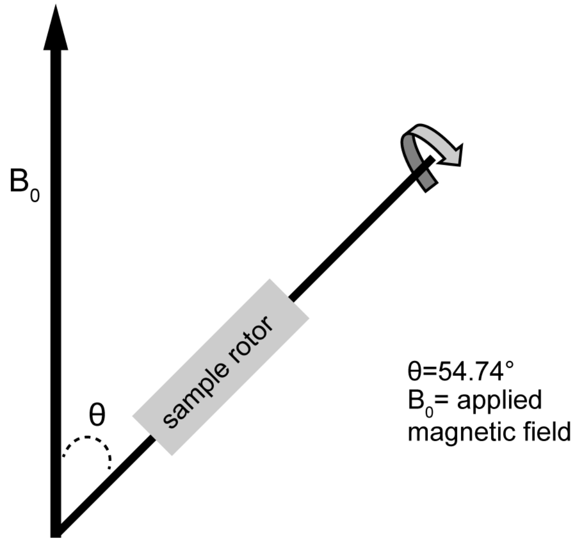

Figure 1.3. The basics of a magic-angle spinning experiment. The sample is spun rapidly in the rotor about a spinning axis θ with respect to the magnetic field B_0. MAS removes the effects of CSA and heteronuclear dipolar coupling to decrease line-broadening.

An example of the effects of MAS is shown in Figure 1.4. In the static spectrum, the line-shape is so broad it is impossible to obtain any analytical information. However, as the sample is spun, the peak shape narrows. At slow spinning speeds, sets of spinning sidebands are evident; these are peaks separated from the isotropic chemical shift by the spinning speed. As the spinning speed is increased, the number of spinning sidebands decreases. In order for spinning sidebands to be eliminated, the sample must be spun at a rate 3-4 times faster than the anisotropy. This may not be possible with many probes due to their physical limitations. Even at a spin rate of 15 kHz, some side-bands are still evident (Figure 1.4).

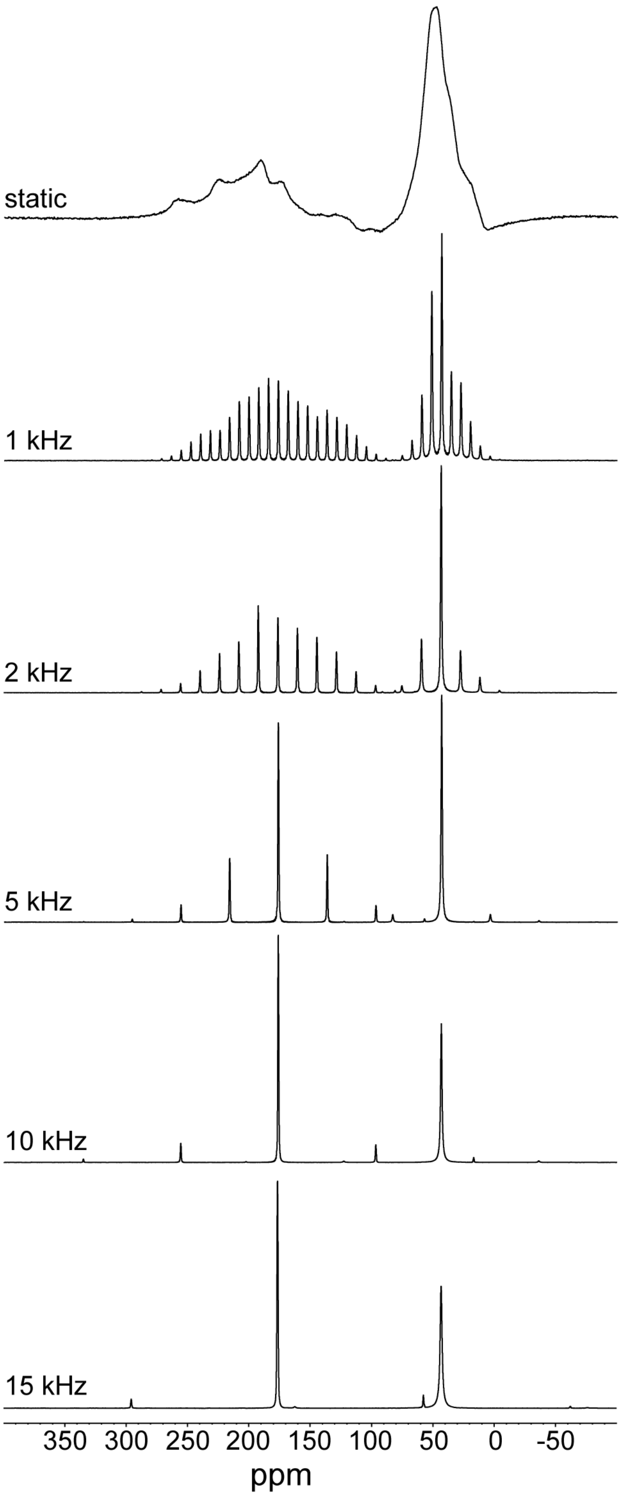

Figure 1.4. 1D ^{13}C CP MAS of ^{13}C-enriched glycine at differing spinning speeds.

1.3.2 *Cross Polarization.*

Cross-polarization (CP) is a technique used to assist in the observation of dilute spins, or spins with a low natural abundance. The observation of dilute spins poses problems, including low signal-to-noise and long relaxation times. Both problems can be solved using CP, where the polarization of an abundant spin (i.e. ^{1}H) is transferred to a dilute spin (i.e. ^{13}C and ^{15}N).

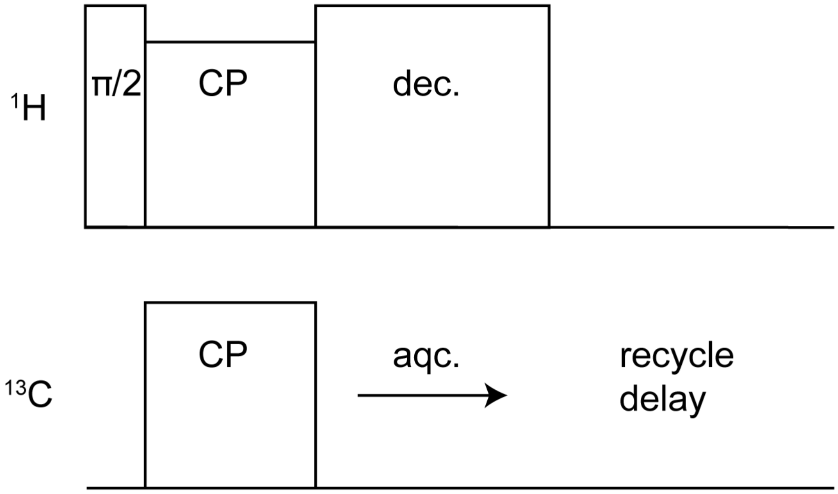

Figure 1.5. A basic 1D CP MAS pulse program with acquisition of ^{13}C. Each block is a radio-frequency (RF) pulse and is labeled with the type (i.e. π/2, CP, decoupling).

Figure 1.5 shows a basic CP pulse program. The abundant nucleus, in this case ^{1}H, is excited by a π/2 RF pulse. Then, during contact time, both the abundant and dilute spins are subjected to RF pulses, labeled CP in Figure 1.5. It is during this contact time that polarization is transferred. The polarization transfer is possible due to the matching of Hartmann-Hahn conditions. The contact pulse amplitudes must be set so that the energy gaps between the rotating frame spin states of the abundant (^{1}H) and dilute (^{13}C) spins are equal, as shown in Figure 1.6.

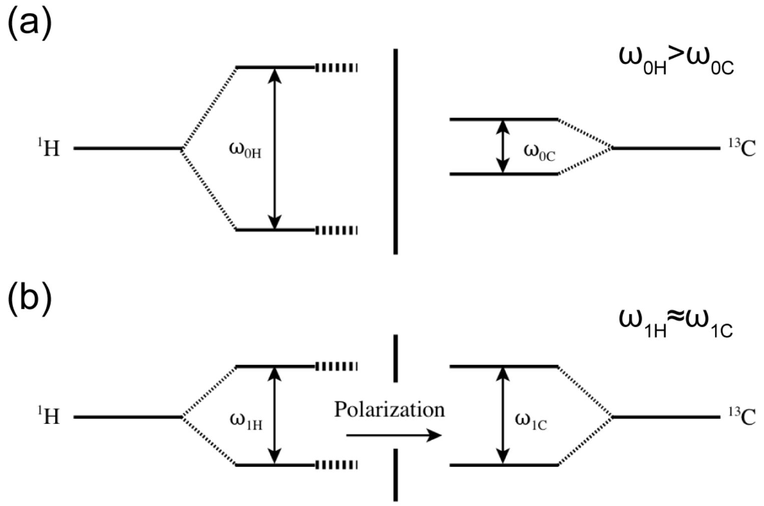

Figure 1.6. (a) The typical difference between ^1H and ^{13}C rotational frequencies. (b) The Hartmann-Hahn matching of energy levels and rotational frequencies of ^1H and ^{13}C. The matching of rotational frequencies enables the transfer of polarization from ^1H to ^{13}C spins.

This thesis utilizes 1D CP MAS experiments to observe both ^{13}C and ^{15}N spins. However, even with the benefits of CP, these 1D spectra are not always sufficient. Often, the line-shapes in peptide-mineral complexes remain broad, and overlap of multiple peaks is common. In these scenarios, 2D spectroscopy is necessary.

1.3.3 *2D Dipolar Assisted Rotational Resonance Experiments.*

In the solid-state, 1D spectra often lack the resolution to resolve peaks with similar chemical shifts. Under these circumstances, 2D correlation experiments are necessary. Correlation experiments can be heteronuclear or homonuclear, and many different pulse sequences are used. This thesis focuses on Dipolar Assisted Rotational Resonance (DARR)[48,49] experiments, a homonuclear dipolar coupling experiment.

A typical pulse program for DARR is shown in Figure 1.7. The π/2 pulse on the ^{1}H channel excites the protons, and the polarization is transferred to the ^{13}C spins during the CP pulse. After the evolution period (t_1), a π/2 pulse places magnetization along the z-axis. Then, during the mixing time, spins interact and exchange magnetization, resulting in the cross-peaks in the 2D spectrum. There is no decoupling during the mixing time. A final π/2 pulse returns magnetization to the transverse plane, where the acquisition takes place. With short mixing times, intra-residue interactions are observed exclusively. At longer mixing times, inter-residue peaks can be observed, making DARR a versatile experiment.[48,50,51]

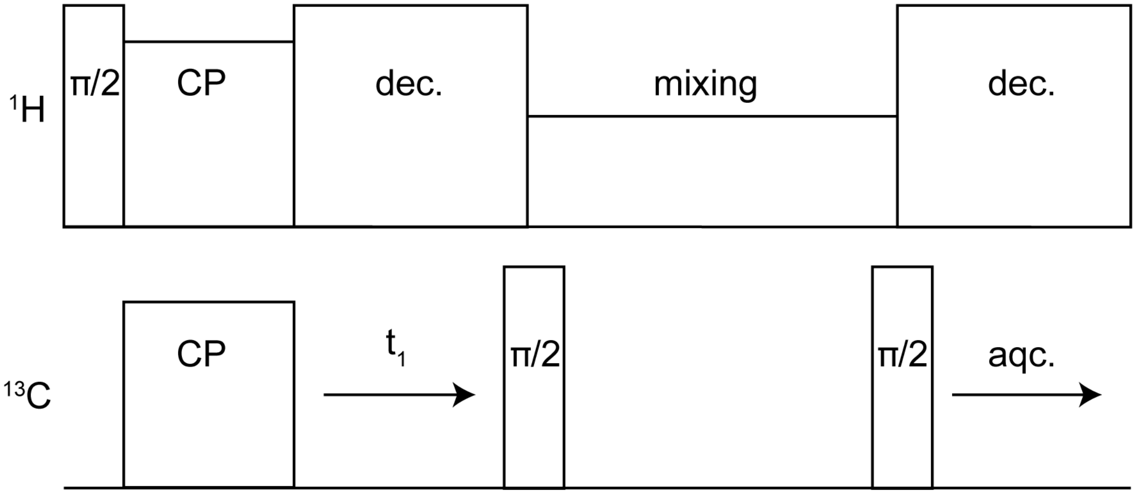

Figure 1.7. A typical pulse program for a DARR experiment. Each block is a radio-frequency (RF) pulse and is labeled with the type (i.e. π/2, CP, decoupling). Adapted from Takegoshi, et. al. [48,50]

^{13}C spins that are close in space experience the effects of dipolar coupling. This results in the formation of cross-peaks in the 2D spectrum. A DARR spectrum of ^{13}C-enriched glycine is shown in Figure 1.8. The diagonal peaks result from contributions of magnetization that have not been changed by mixing, meaning they are from contributions which remain on the same nucleus. These diagonal peaks act to divide the spectrum into two symmetrical halves. On either side of the diagonal are the cross-peaks, which result from the interaction of two distinct nuclei, originating when magnetization is exchanged during mixing time. Therefore, the cross-peaks contain the essential information in a 2D spectrum. The cross-peaks allow for the unambiguous assignment of chemical shifts.

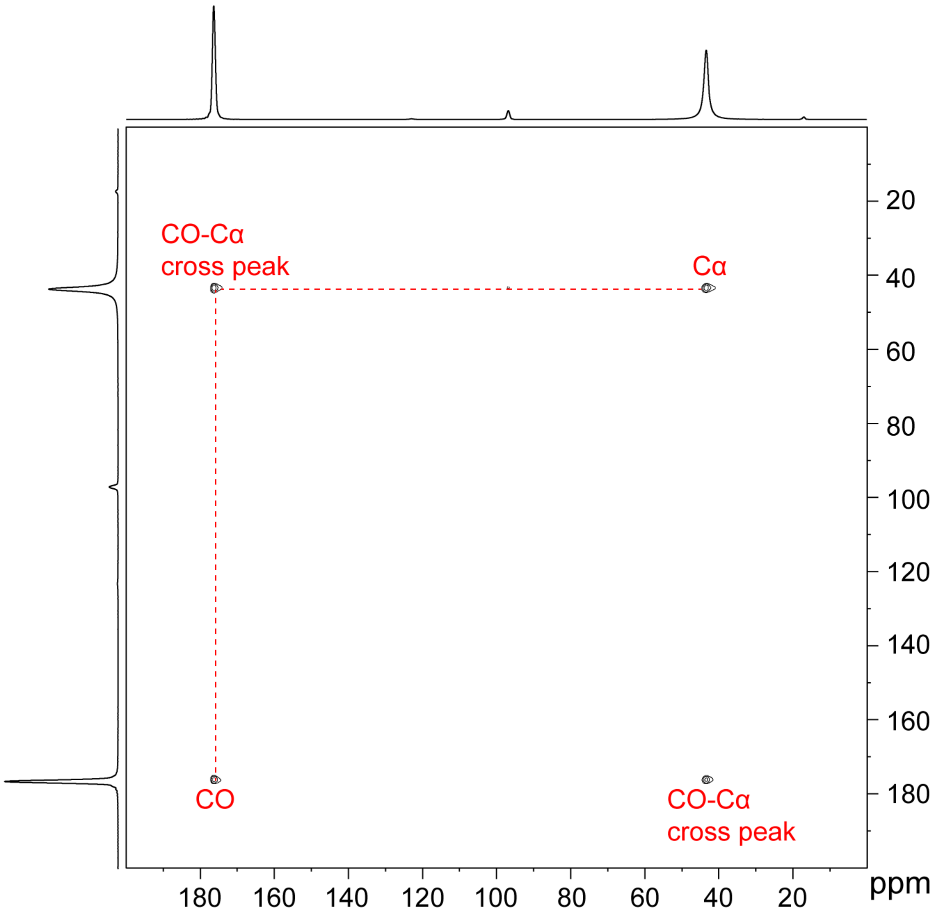

Figure 1.8. ^{13}C-^{13}C DARR spectrum of ^{13}C-enriched glycine.

1.3.4 *Chemical Shifts.*

The isotropic chemical shift is defined as the resonant frequency of a spin in reference to a standard, either directly or indirectly, typically tetramethylsilane (TMS) for ^{13}C experiments. The isotropic chemical shift is expressed mathematically as:

$$\delta_{iso}(ppm) = 10^6 x \frac{\nu - \nu_{ref}}{\nu_{ref}} \tag{1.1}$$

where ν is the spectral frequency of the spin of interest and ν_{ref} is the spectral frequency of the standard. Chemical shifts (CS) are typically reported in parts per million (ppm).

The CS for a particular spin is affected by its local magnetic environment. Because of this, analysis of CS can provide information on the local electronic environment of the spin in question, and chemical shifts of typical spins fall in identified regions of the spectra. For solid-state ^{13}C ssNMR of peptides, the downfield region (deshielded, higher ppm) contains the carbonyl spins, while the upfield region (shielded, lower ppm) contains the aliphatic spins. Furthermore, it is widely accepted that the chemical shifts of backbone ^{13}C spins (^{13}CO, ^{13}Cα, and ^{13}Cβ) are affected by the secondary structure of the peptide.[52–58] Therefore, structural information can be gleaned through analysis of chemical shifts and chemical shift perturbations.

1.4 TALOS-N.

Once chemical shift assignments have been made, a means of interpreting them is necessary. A couple different methods of interpretation will be used in this thesis. First, ΔCS (the difference in chemical shifts for a particular spin in a neat versus mineral-complexed peptide) will be evaluated. ΔCS help quantify the degree to which the mineral perturbs the peptide structure. The changes in chemical shift can indicate a change in conformation, environment, and/or mobility, and is particularly helpful in the understanding of side-chain behavior. Second, we will use TALOS-N, a program that predicts protein/peptide backbone torsion angles from experimentally-obtained NMR chemical shifts.[59]

TALOS-N uses database-derived empirical methods along with an artificial neural network to make ϕ and ψ torsion angle assignments. It makes the assumption that homologous peptide sequences have similar chemical shifts. It searches a database (comprised of a plethora of proteins pared with complete backbone NMR chemical shifts and atomic information extracted from the BMRB[60], PDB[61], and X-ray structures) for the 10 best matches to the chemical shifts of a residue along with the residue's immediate neighbors. TALOS-N also provides error for its assignments and rates each assignment based on consistent matching within a single area of the Ramachandran plot (Figure 1.10).[62,63]

The torsion angles predicted by TALOS-N allow for the determination and visualization of peptide secondary structure. The torsion angles are input into Chimera[64], a program used to visualize and analyze molecular structures. With the use of TALOS-N and Chimera, we are able to produce three-dimensional images of the peptides studied via ssNMR.

1.5 PROTEIN STRUCTURE.

It is necessary to include a brief overview of protein structure considering the significant emphasis placed on it in this thesis. The primary structure of a protein is the amino acid sequence. Each amino acid is linked together via a peptide bond, which joins the amino group of one residue to the carboxyl group of the neighboring residue through a dehydration reaction. The primary structure directs the intramolecular bonding and thus the protein folding, determining the 3D conformation of the protein.

The secondary structure is the 3D structure in localized regions of the protein. Hydrogen bonds form between amino groups and carboxyl groups in neighboring regions, and often result in specific folding patterns, such as α-helices and β-sheets. The torsion angles ϕ and ψ (Figure 1.9) essentially dictate the protein folding, causing the backbone to adopt a specific conformation. The torsion angle ω is essentially flat and is fixed at 180°.

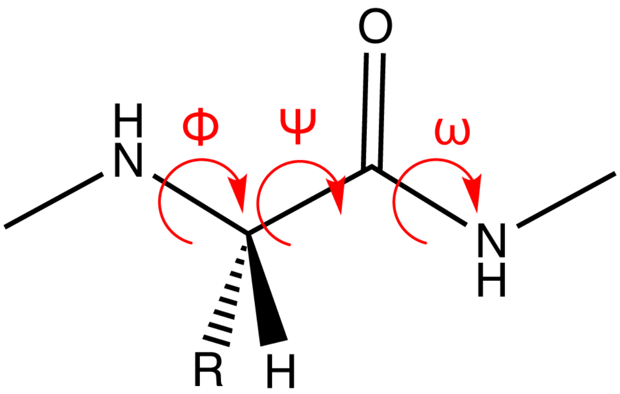

Figure 1.9. A fragment of a peptide backbone showing the torsion angles ϕ, ψ, and ω. R represents an amino acid side-chain.

The torsion angles ϕ and ψ are restricted to a set of values, as shown in the Ramachandran plot (Figure 1.10). Theoretically, the average ϕ and ψ values for α-helices are -57 and -47, respectively and the average ϕ and ψ values for β-sheets are -80 and +150, respectively. Experimental values are often clustered around these averages but can also diverge from the norms. For example, glycine ϕ/ψ angles often differ from the accepted values. Glycine does not have a side-chain, allowing for more flexibility along the peptide backbone. This makes otherwise forbidden ϕ/ψ angles acceptable. For this reason, glycine residues are often found in regions containing loops or turns.

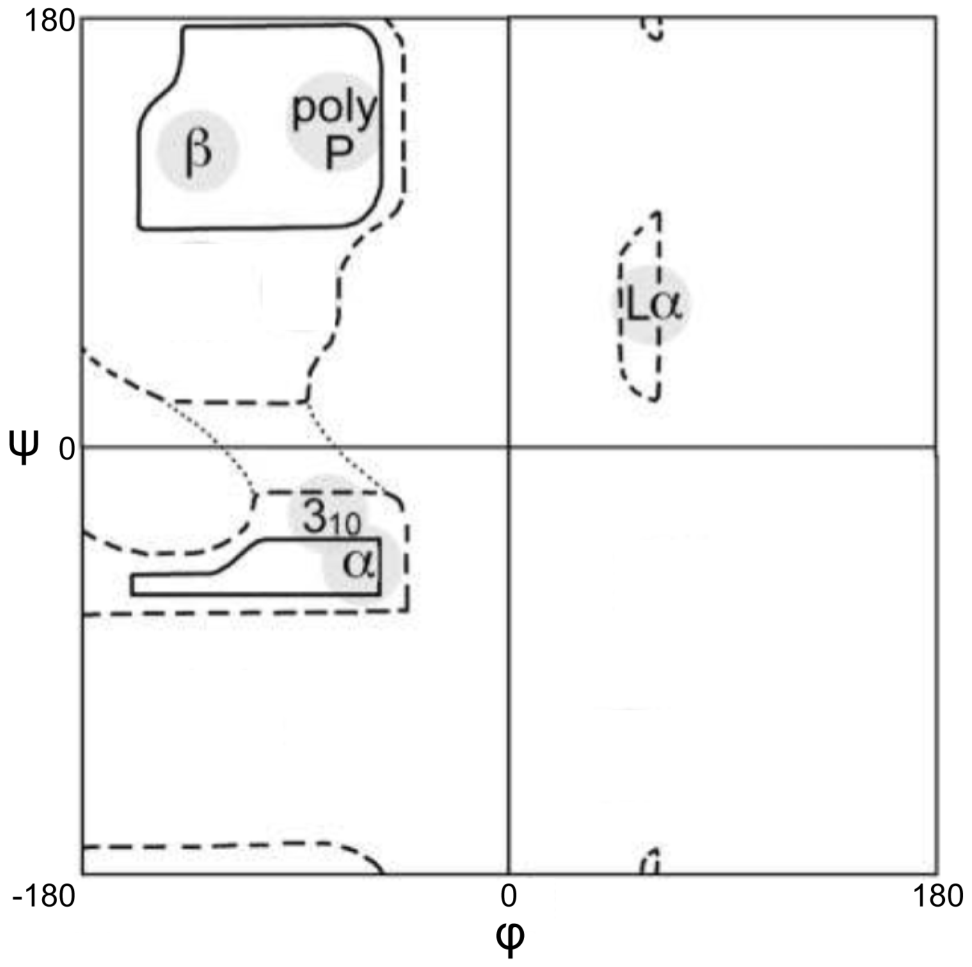

Figure 1.10. A traditional Ramachandran plot. The horizontal axis shows ϕ values while the vertical axis shown ψ values. The defined boundaries show the torsion angles allowed for each type of secondary structure: α-helix (α), β-sheet (β), and left-handed α-helix (Lα). Figure adapted from Lovell, et. al.[65]

The tertiary structure of a protein is the folding of the entire protein chain, including each secondary structure. The tertiary structures of proteins are often held together through the interactions of amino acid side-chains via ionic interactions, hydrogen bonds, van der Waals forces, or disulfide bridges. This thesis will not discuss tertiary structure, as the peptides studied are too small to have a tertiary structure.

Quaternary structure is the assembly or aggregation of multiple protein units. This thesis does not focus on quaternary structure, per se, but does discuss peptide aggregation.

1.6 SUMMARY.

This thesis will use the ssNMR techniques described along with TALOS-N to probe the secondary structures of biomineralization/biomimetic peptides and surface-adsorbed peptides.

Chapter 2 will focus on the role of peptide structure on silica (SiO_2) and titania (TiO_2) morphologies, which was investigated through the R5 peptide domain. R5 produces uniform SiO_2 and TiO_2 nanostructures from the precursors silicic acid and titanium bis(ammonium lactato)dihydroxide (TiBALDH), respectively. The resulting biosilica and biotitania nanostructures are characterized using scanning electron microscopy (SEM). To investigate the process of R5-mediated SiO_2 and TiO_2 formation, we carry out 1D and 2D ssNMR studies on R5 samples with uniformly ^{13}C- and ^{15}N-labeled residues to determine the backbone and side-chain chemical shifts. ^{13}C chemical shift data are in turn used to determine peptide backbone torsion angles and secondary structure for the R5 peptide neat, *in silica*, and *in titania*. We are thus able to assess the impact of the different mineral environments on peptide structure, and we can further elucidate from ^{13}C chemical shifts changes the degree to which various side-chains are in proximity to the mineral phases.

Chapter 3 focuses on the identification of a series of serine-lysine (S-K) peptides as candidates for the biomimetic production of TiO_2 nanostructures. We have assayed various S-K peptides for TiO_2-precipitating activity upon exposure to TiBALDH and have characterized the resulting co-precipitates using SEM. A subset of these assayed peptides efficiently facilitates the production of TiO_2 nanospheres. This thesis investigates the process of TiO_2 nanosphere formation mediated by the S-K peptides KSSKK and $SKSK_3SKS$ using 1D and 2D ssNMR, which is used to assign ^{13}C chemical shifts site-specifically in each free peptide and TiO_2 co-precipitated peptide. The chemical shifts are used to derive secondary structures in the neat and TiO_2 co-precipitated states. The backbone ^{13}C chemical shifts are used to assess secondary structural changes undergone during the co-precipitation process. Side-chain ^{13}C chemical shift changes are analyzed with Density Functional Theory (DFT) calculations and used to determine side-chain conformational changes that occur upon co-precipitation with TiO_2 and to determine surface orientation of lysine side-chains in TiO_2-peptide composites.

Chapter 4 focuses on how SNa15 interacts with a variety of mineral surfaces. Adsorption isotherms characterize the binding of SNa15 to HAP, SiO_2, and TiO_2. 1D ^{13}C CP MAS, 1D ^{15}N CP MAS, and 2D ^{13}C-^{13}C DARR experiments on SNa15 samples with uniformly ^{13}C- and ^{15}N-enriched residues are used to assign backbone and side-chain chemical shifts. Backbone ^{13}C chemical shift data are used to determine ϕ/ψ torsion angles. The torsion angles are used to visualize secondary structures for neat and adsorbed SNa15. We are able to evaluate the impact of the surfaces on SNa15 structure through the analysis of secondary structure and backbone chemical shift perturbations. Furthermore, we use side-chain ^{13}C and ^{15}N chemical shift data to assess the degree to which various side-chains are close to and interacting with each surface, and we hypothesize a binding domain for SNa15.

Chapter 2. BIOMINERALIZATION AND THE R5 PEPTIDE.[2]

R5 is a fragment of the silaffin sil1p, the protein implicated in regulating the process of SiO_2 biomineralization in the diatom *Cylindrotheca fusiformis*. The primary structure of sil1p has a repetitive peptide sequence between residues 108 and 271, composed of seven units.[21] The fifth of which is a 19 amino acid peptide known as R5, with the sequence SSKKSGSYSGSKGSKRRIL.

2.1 R5 PRECIPITATES SILICA AND TITANIA NANOSPHERES.

R5 has the ability to precipitate SiO_2 nanospheres in a manner similar to its parent silaffin without the need for post-translational modifications.[21] Mutation studies by Knecht and Wright[21] have shown that R5 self-assembles to produce SiO_2, and that the C-terminal RRIL motif is integral to this process. The authors suggest that the RRIL motif encourages a micellar self-assembly due to the arginine's guanidinium groups in close proximity to hydrophobic leucine and isoleucine residues.[21] Although this claim has been questioned recently by Senior et. al.,[66] whose DLS study found no evidence of aggregate formation in solutions of R5, mutation studies by Lechner and Becker[67] support the need for the RRIL motif, however not necessarily at the C-terminal position or in the native order. Lechner and Becker also demonstrated the importance of the amino groups of the lysine residues in SiO_2 formation. Their study found the structure of the resulting SiO_2 is dependent on the number as well as position of lysine residues within the R5 sequence.[67] An alternative mechanism of R5-SiO_2 precipitation involves R5 self-assembly driven by salt bridges that form between the guanidine groups of arginine residues and phosphate

---

[2] This chapter has been reproduced from Buckle, E.L.; Roehrich, A.; Vandermoon, B.; Drobny, G.P. Comparative Study of Secondary Structure and Interactions of the R5 Peptide in Silicon Oxide and Titanium Oxide Coprecipitates Using Solid-State NMR Spectroscopy. *Langmuir* **2017**, 33 (40), 10517-10524.

anions. Cationic amino groups then bring silicic acid and SiO_2 particles into close proximity, which promotes the condensation reaction.[21,67] Additionally, peptides rich in lysine and various cationic polymers have been used to facilitate SiO_2 production with various morphologies.[68–71]

Biomimetic approaches are also being applied to the synthesis of non-biological materials, specifically TiO_2, using the precursor titanium bis(ammonium lactato)dihydroxide (TiBALDH).[72–79] An example of such an approach is that of Sewell and Wright,[79] who have shown that R5 can produce TiO_2 nanospheres under mild conditions when introduced to solutions containing TiBALDH.

Although much effort has been put forth to characterize the mechanism of R5's role in SiO_2 precipitation, significantly less work has been done to elucidate the role it plays in TiO_2 precipitation. Elucidating the structure of R5 within both SiO_2 and TiO_2 co-precipitates of similar morphology is an important first step in understanding how R5 directs the formation of TiO_2. This study is focused upon the following questions:

- What is the secondary structure of R5 within each mineral co-precipitate (SiO_2 and TiO_2)?
- How do the co-precipitated structures differ from free, neat R5?
- Which residues interact with the surrounding SiO_2 or TiO_2?
- To what degree do the structural principles that underlie the TiO_2-precipitating activity resemble those of the SiO_2-precipitating activity?

By comparing the lesser-studied R5-TiO_2 to R5-SiO_2, we augment our understanding of the R5-TiO_2 system. These questions will be explored further in this chapter through analysis via ssNMR and other methods.

2.2 EXPERIMENTAL METHODS.

All natural and uniformly labeled ^{13}C and ^{15}N amino acids were purchased from Sigma Aldrich (St. Louis, MO). Preloaded FMOC-protected Wang resin was purchased from EMD Millipore (Billerica, MA). All other reagents were purchased from Sigma Aldrich (St. Louis, MO) and used without purification.

2.2.1 *Peptide Synthesis.*

Peptides were synthesized on a CEM Liberty Blue peptide synthesizer using a standard 9-fluorenylmethoxycarbonyl (FMOC) and *tert*-butyl protection scheme. Preloaded FMOC-protected Wang resin was used for solid phase synthesis. Peptides were cleaved from the resin in a 10 mL solution of 95:2.5:2.5 trifluoroacetic acid (TFA): triisopropylsilane (TIS): water mixture per 1.0 gram of peptide/resin. The resulting filtrate was added dropwise into cold tert-butyl methyl ether, followed by centrifugation and three rinses of the resulting solids with 40 mL of cold tert-butyl methyl ether. Peptides were purified using RP-HPLC (Varian ProStar HPLC, Alltima WP C4 column, 5 mL/min, eluent A: water with 0.2% TFA, eluent B: acetonitrile with 0.2% TFA), using a gradient of 15-35% B over 40 minutes. Chromatograms were generated by observing the UV absorbance at 274 nm, and the analyte was verified by mass spectrometry. The fractions were then lyophilized, resulting in the pure peptide.

2.2.2 *SiO_2 Precipitation.*

Orthosilicic acid ($Si(OH)_4$) was freshly made before each precipitation by dissolving 0.15 mL tetramethyl orthosilicate in 0.85 mL 1 mM HCl to form 1 M $Si(OH)_4$. Orthosilicic acid (100 μL per 5 mg R5) was added to a solution of R5 dissolved in phosphate-citrate buffer (1.00 mL, 100 mM, pH=7.0) and vortexed. The solution was incubated for 5 minutes at room temperature. The precipitated R5-SiO_2 was separated from the mixture via centrifugation at 15000 x g for 10 minutes. The resulting precipitate was rinsed with Millipore water 3 times and dried *in vacuo*.

2.2.3 *TiO_2 Precipitation.*

TiBALDH (100 μL per 5 mg R5, 1M) was added to a solution of R5 of varying concentrations dissolved in phosphate-citrate buffer (1.00 mL, 100 mM, pH=7.0) and vortexed. The solution was incubated for 30 minutes at room temperature. The precipitated R5-TiO_2 was separated from the mixture via centrifugation at 15000 x g for 10 minutes. The resulting precipitate was rinsed with Millipore water 3 times and dried *in vacuo*.

2.2.4 *SiO_2 and TiO_2 Morphology Characterization.*

SEM images were taken on a FEI Sirion XL30 scanning electron microscope operating at variable voltages. Precipitates were dispersed onto a carbon tap, mounted on aluminum studs, and sputter-coated for 60-90 seconds with Au/Pd.

2.2.5 *Solid-state NMR.*

All solid-state NMR experiments were conducted using a 16.4 T magnetic field (proton resonant field of 700.18 MHz) on a Bruker Avance III spectrometer fitted with a ^{1}H {^{13}C,^{15}N} 3.2 mm MAS probe. The ^{13}C NMR signal was enhanced using cross-polarization (CP) with a ^{1}H-^{13}C contact time of 1.1 ms, and a magic angle spinning (MAS) rate of 10-15 kHz ± 5Hz was maintained with a Bruker MAS controller unit. One-dimensional ^{13}C CP-MAS experiments were performed with a proton 90 degree pulse time of 2.75 μs and a recycle delay of 2s. The number of scans for the neat R5 and the R5-TiO_2 complex ranged from 2k-32k. To obtain the resolution needed to confidently assign all the chemical shifts in the R5 samples, 2D ^{13}C-^{13}C dipolar assisted rotational resonance (DARR)[48] experiments were performed. The 2D spectra were collected with 30 or 60 ms mixing times and a recycle delay of 1.5s, with 128 points in the indirectly detected dimension and 512 points in the directly detected dimension. All chemical shifts reported were indirectly referenced to tetramethylsilane (TMS) in the solid-state using adamantane (δ=38.48).[80]

2.3 PEPTIDE-MINERAL PRECIPITATION.

Figure 2.1 displays SEM images of the R5-TiO_2 (Figure 2.1a) and R5-SiO_2 (Figure 2.1d) co-precipitates. Both peptide-mineral co-precipitates are approximately spherical, but with varying average diameters; an average diameter of 734 ± 180 nm for the R5-TiO_2 co-precipitates and 594 ± 93 nm for the R5-SiO_2 co-precipitates. The size distribution histograms for both the R5-TiO_2 co-precipitates (Figure 2.1b) and R5-SiO_2 co-precipitates (Figure 2.1e) are shown. The spherical morphologies of the R5-TiO_2 particles are consistent with those observed by Sewell and Wright[79], although the average size of the R5-TiO_2 particles we observe is larger than they report. The average size of the R5-SiO_2 particles we observe is consistent with those observed in the literature.[17,21,67]

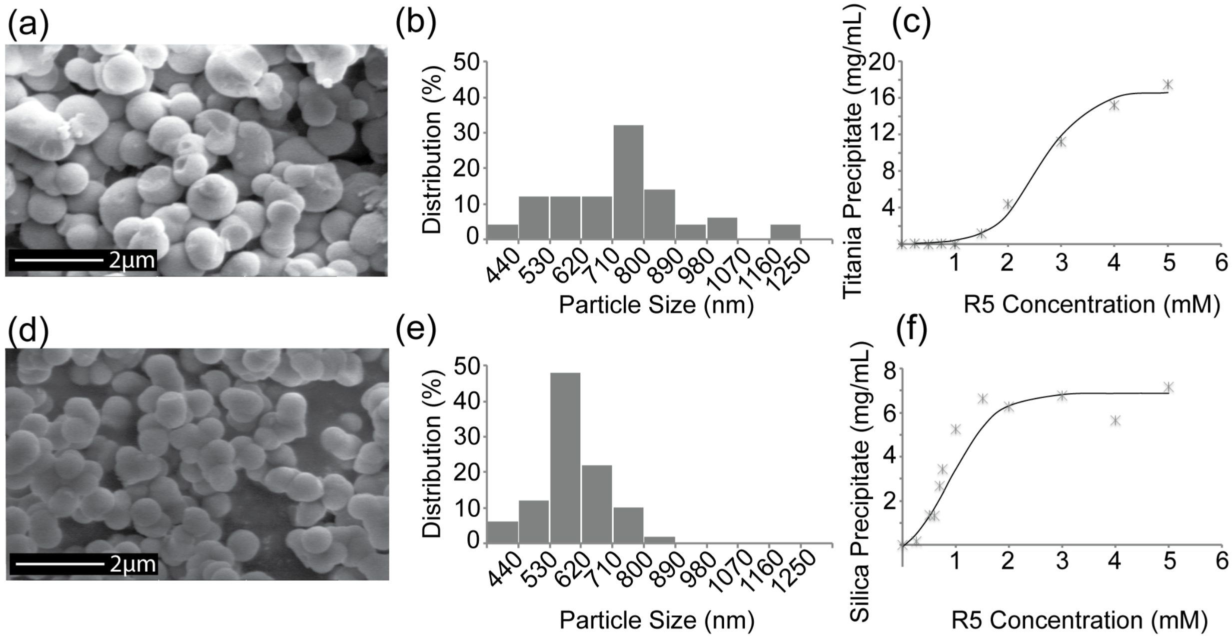

Figure 2.1. (a) SEM image of R5-TiO_2 co-precipitates showing spherical morphologies with a mean diameter of 734 ± 180 nm. (b) Size distribution histogram for R5-TiO_2 co-precipitates. Particle sizes are measured using ImageJ.[81] (c) TiO_2 produced as a function of R5 concentration. The concentration of TiBALDH was held constant at 0.1 M. Data are a mean from two independent repeats. (d) SEM image of R5-SiO_2 co-precipitates showing spherical morphologies with a mean diameter of 596 ± 93 nm. (e) Size distribution histogram for R5-SiO_2 co-precipitates. Particle sizes are measured using ImageJ.[81] (f) SiO_2 produced as a function of R5 concentration. The concentration of $Si(OH)_4$ was held constant at 0.1 M. Data are a mean from two independent repeats.

Figure 2.1c and Figure 2.1f illustrate the differences in R5 activity between the TiO_2 and SiO_2 systems. TiO_2 is only precipitated above 1 mM R5, while SiO_2 is precipitated above 0.5 mM R5. While both systems appear cooperative in nature based on the shape of the curves, it is more pronounced for the R5-TiO_2 system, suggesting that in order to induce TiO_2 formation, more R5 molecules must aggregate. This is consistent with the larger particle sizes seen for R5-TiO_2 co-precipitates, see Figure 2.1b and Figure 2.1e. There may also be significant electrostatic contributions to the larger amounts of SiO_2 precipitation at lower concentrations; the cationic R5 may have a stronger attraction to the more anionic SiO_2 than to TiO_2.[82] SiO_2 precipitation levels out at a much lower concentration of R5 than TiO_2 precipitation, which also produces more product at the highest concentration tested.

Both R5-TiO_2 and R5-SiO_2 consist of R5 peptide that is embedded in a mineral nanostructure. Inductively coupled plasma optical emission spectrometry (ICP-OES) (Table 2.1) reveals that phosphorus is present in both mineral co-precipitates after extensive washing of the precipitated samples. The only source of phosphorous is phosphate anions present in the buffer, so logically it must be attributed to phosphate embedded within the co-precipitate, indicating an incorporation of the phosphate-citrate buffer within the co-precipitates. Examining the secondary structures of R5-TiO_2 and R5-SiO_2 can provide insight into how R5 interacts with the phosphates present in each mineral environment.

Table 2.1. Percentages (m/m %) of the elements phosphorous, silicon, and titanium in the R5 –silica and –titania co-precipitates as determined by ICP-OES.

Sample	Phosphorous (m/m %)	Silicon (m/m %)	Titanium (m/m %)
R5-TiO2	11.2	N/A	32.8
R5-SiO2	17.5	32.1	N/A

2.4 CHEMICAL SHIFT ASSIGNMENTS.

1D ^{13}C CP MAS experiments were performed in conjunction with 2D ^{13}C-^{13}C DARR experiments in order to obtain site-specific chemical shift assignments. We resolved and assigned most of the ^{13}C spectrum of R5 in TiO_2 containing up to three uniformly ^{13}C- and ^{15}N-enriched amino acids. The structures of the amino acids examined are shown in Figure 2.2.

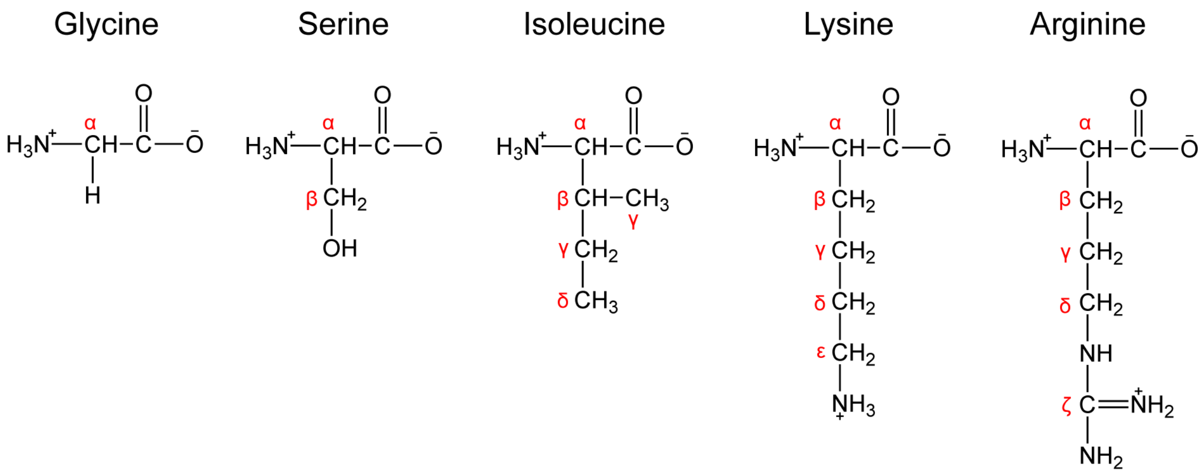

Figure 2.2. Structures of the amino acids for which chemical shift assignments are made in R5. Structures are shown for neutral pH (pH=7). Conventional side-chain atom labels are shown.

To assign the chemical shifts for the entire peptide, seven isotopically enriched samples were analyzed, as shown in Table 2.2. The only amino acids not assigned by this study were S7, Y8 and the C-terminal L19. Roehrich and Drobny[17] conducted the same set of experiments on the same seven enriched samples for both the neat R5 peptide and on the R5-SiO_2 co-precipitate, to which comparisons will be made.[17]

Table 2.2. R5 peptides synthesized in this study. (*) Indicates that the preceding amino acid is uniformly ^{13}C and ^{15}N enriched.

Sample Name	Label Position
R5-S	S*SKKSGSYSGSKGSKRRIL
R5-SK	SS*K*KSGSYSGSKGSKRRIL
R5-KSG	SSKK*S*G*SYSGSKGSKRRIL
R5-GSKm	SSKKSGSYSG*S*K*GSKRRIL
R5-GSKc	SSKKSGSYSGSKG*S*K*RRIL
R5-R	SSKKSGSYSGSKGSKR*RIL
R5-SRI	SSKKSGSYS*GSKGSKRR*I*L

All 1D ^{13}C spectra are shown in Appendix A. Stacked plots allow for the direct comparison of chemical shift and peak shape between the three peptide states: neat, R5-SiO_2, and R5-TiO_2. The downfield region (larger ppm) contains the carbonyl ^{13}C spins, and the upfield region (smaller ppm) contains the aliphatic ^{13}C spins (^{13}Cα, ^{13}Cβ, ^{13}Cγ, ^{13}Cδ, ^{13}Cε, and ^{13}Cζ).

The overlap of the carbonyl ^{13}C spins and many of the aliphatic ^{13}C spins illustrates the need for 2D spectroscopy. Figure 2.3 shows a typical DARR spectrum obtained from the selectively ^{13}C labeled peptide R5-GSKc TiO_2, which demonstrates the assignment of the ^{13}C spins in G13, S14, and K15. The horizontal and vertical lines delineate cross-peaks, which indicate networks of dipolar-coupled ^{13}C spins. To ensure the observation of only intra-residue cross-peaks, DARR spectra were taken with mixing times of 30 ms and 60 ms. In a few cases, however, unique chemical shifts could not be assigned; for example, it was not possible to assign the two δ ^{13}C shifts for I18.

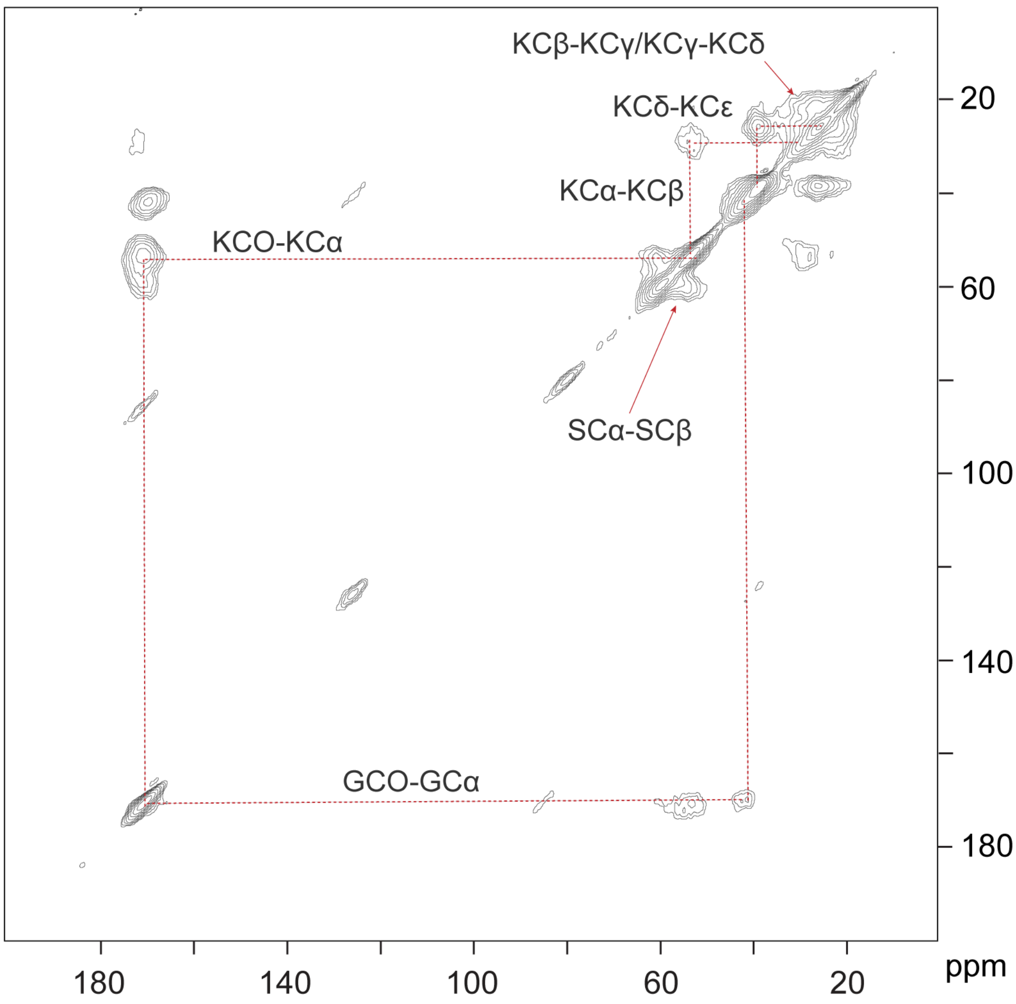

Figure 2.3. ^{13}C-^{13}C DARR spectrum for the R5-GSKc in the TiO_2 co-precipitate. Vertical and horizontal lines indicate assignments of ^{13}C spins in G13, S14, and K15.

Changes in chemical shift (ΔCS) for backbone and side-chain ^{13}C nuclei in the neat versus in co-precipitated samples occur to varying degrees at sites along the peptide backbone and side-chains. The ^{13}C chemical shift perturbations of the backbone ^{13}CO, $^{13}C\alpha$, and ^{13}Cb chemical shifts are associated with a change in secondary structure as a result of precipitation with SiO_2 or TiO_2. To study systematically the degree to which R5 peptide ^{13}C chemical shifts have been perturbed upon co-precipitation with SiO_2 and TiO_2, ΔCS values are obtained by subtracting the chemical shift of the ^{13}C spin in neat R5 from the corresponding ^{13}C spin in the R5-TiO_2 or R5-SiO_2 co-precipitate. A positive ΔCS indicates a downfield perturbation of the chemical shift (higher ppm, less shielded) in the co-precipitate versus the neat solid peptide, while a negative ΔCS indicates an upfield perturbation of the chemical shift (lower ppm, more shielded). Bar charts of backbone ΔCS values are shown in Figure 2.4. In both R5-SiO_2 and R5-TiO_2, significant perturbations are observed in the S1, S2, and I18 ^{13}CO shifts, the K3, K4, and S5 ^{13}Cα shifts, and the S5, S14, and R17 ^{13}Cβ shifts. The chemical shift perturbations in R5-TiO_2 and R5-SiO_2 are similar for the S1 ^{13}CO, S2 ^{13}CO, and K4 ^{13}Cα shifts, indicating similar structural changes in R5 in both systems in these regions. The perturbations in the I18 ^{13}CO, the S5 ^{13}Cβ, and the R17 ^{13}Cβ are larger in magnitude for R5-SiO_2 than for R5-TiO_2, while the perturbations in the K3 ^{13}Cα, and the S14 ^{13}Cβ are larger in magnitude in R5-TiO_2 than in R5-SiO_2.

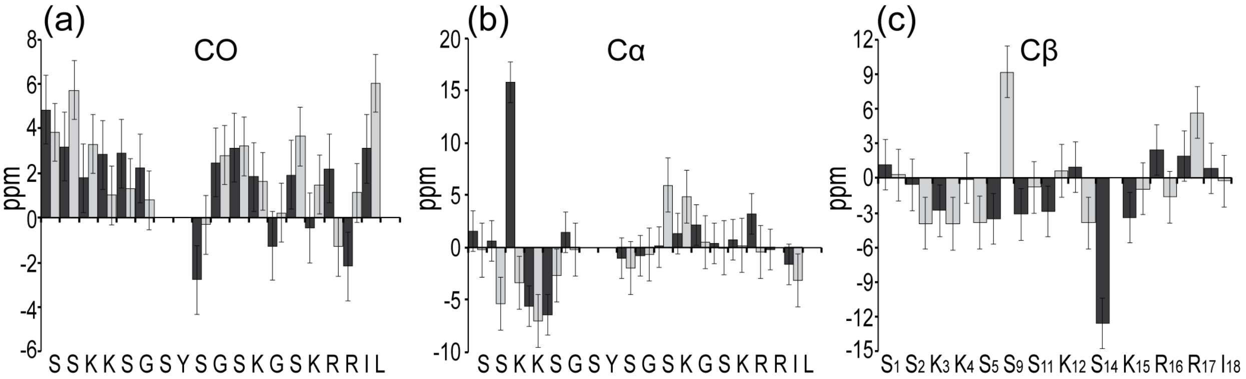

Figure 2.4. Backbone ΔCS plots showing chemical shift perturbations for (a) ^{13}CO shifts, (b) ^{13}Cα shifts, and (c) ^{13}Cβ shifts. ΔCS for R5 co-precipitated with TiO_2 (black) and SiO_2 (gray) are in reference to the neat peptides. Positive changes indicate a downfield shift while negative changes indicate an upfield shift relative to the neat peptide.

Bar charts of side-chain ΔCS values are shown in Figure 2.5 for both the R5-SiO_2 and R5-TiO_2 systems. In R5-TiO_2, K3 ΔCS > 6 ppm for the ^{13}Cε, while in R5-SiO_2 ΔCS values for

^{13}Cγ, ^{13}Cδ, and ^{13}Cε range from 0 ppm to -2 ppm. In previous ssNMR studies of poly-lysine adsorbed onto SiO_2,[83] an upfield perturbation of lysine ^{13}Ce spin chemical shift was attributed to proximity to the negatively-charged SiO_2 surface. Downfield perturbation of the side-chain ^{13}C spin chemical shifts has been similarly interpreted as indicating proximity to positive charge centers in mineral surfaces.[83] Side-chain chemical shift trends in R5-SiO_2 and R5-TiO_2 suggest similar close associations between amino acid side-chains and the inorganic oxide components. Based on these data, K3 is likely interacting with the mineral in both the SiO_2 and TiO_2 systems. In contrast, the ^{13}Cγ/^{13}Cδ/^{13}Cε spins for K12 and K15 in R5-SiO_2 show much smaller or negligible ΔCS. However, we observe a significant upfield shift for ^{13}Cδ of K15 in R5-TiO_2, which is not present in R5-SiO_2.

As mentioned earlier, previous work has shown the arginine residues in R5 are necessary for peptide self-assembly, either by the arginine side-chain's involvement with adjacent hydrophobic residues to effect micelle-like self-assembly[21] or by formation of phosphate salt bridges between the arginine guanidinium groups.[67] The occurrence of guanidinium-phosphate interactions would be expected to perturb the electronic environment of the arginine side-chains. Accordingly, significant chemical shift perturbations are observed in R5-SiO_2 and R5-TiO_2 for ^{13}Cγ, ^{13}Cδ, and ^{13}Cζ in R16 and R17.

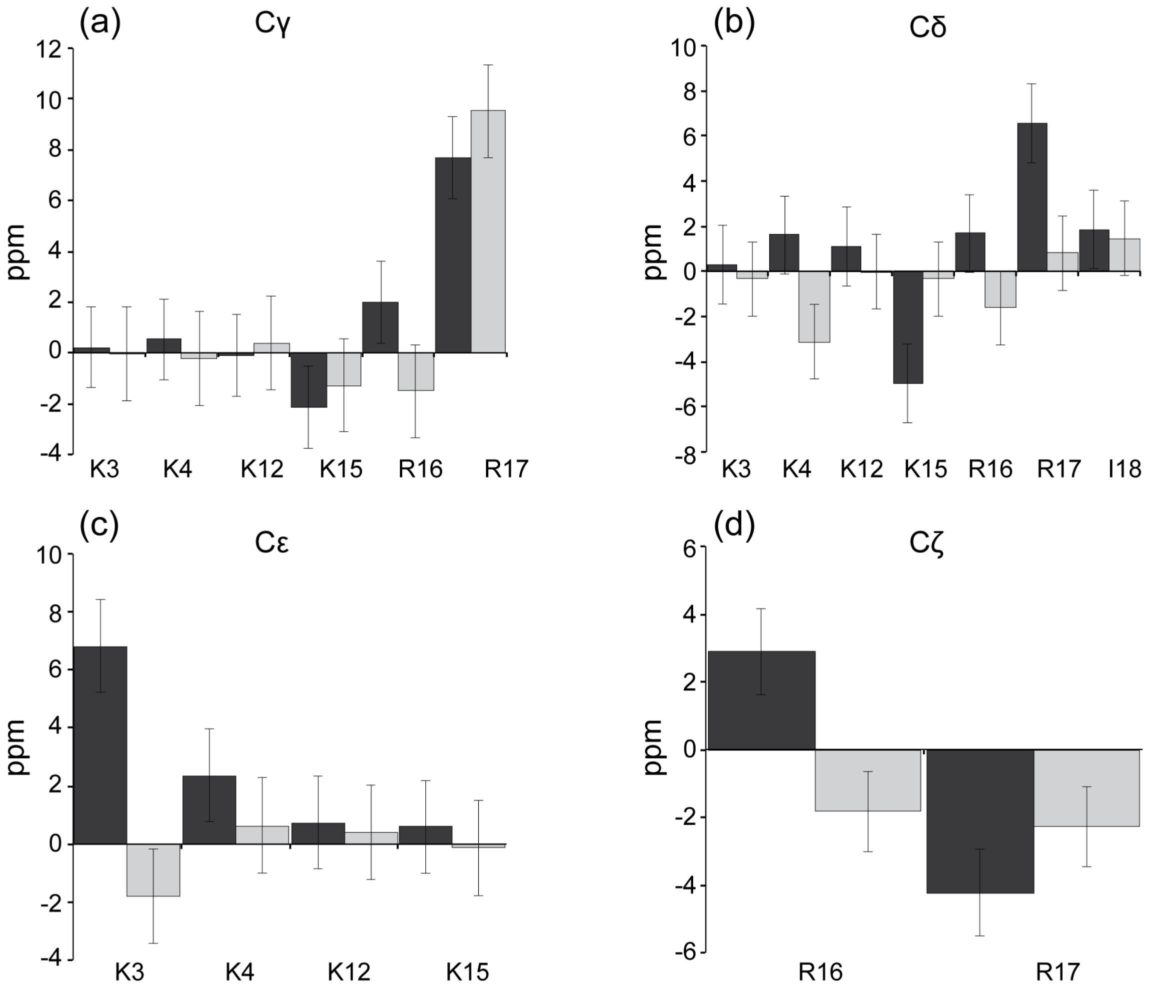

Figure 2.5. Side-chain ΔCS plots showing chemical shift perturbations for (a) ^{13}Cγ shifts, (b) ^{13}Cδ shifts, (c) ^{13}Cε shifts, and (d) ^{13}Cζ ΔCS for R5 co-precipitated with TiO_2 (black) and SiO_2 (gray) are in reference to the neat peptides. Positive changes indicate a downfield shift while negative changes indicate an upfield shift relative to the neat peptide.

2.5 COMPARISON OF PEPTIDE STRUCTURE.

The chemical shifts obtained from the ^{13}CO, ^{13}Cα, and ^{13}Cβ spins in neat R5, R5-TiO_2, and R5-SiO_2 DARR spectra were used to produce TALOS-N[59] input files. TALOS-N[59] output files consist of predicted torsion angles, which were used to visualize the changes in secondary structures for both R5 neat, R5-TiO_2, and R5-SiO_2 peptides using Chimera[64] (Figure 2.6). ϕ/ψ torsion angle values for R5-SiO_2 and R5-TiO_2 generated by TALOS-N[59] are shown in Appendix A. Based on the TALOS-N[59] analysis of ^{13}CO, ^{13}Cα, and ^{13}Cβ chemical shifts, the majority of ϕ torsion angles occur between -80 degrees and -150 degrees in the neat R5 peptide. Furthermore, the majority of ψ torsion angles occur between 40 and 180 degrees. Outliers occur at K4-S5, and near the glycine residues G6-S7 and G10-S11. Aside from these amino acids, the majority of the peptide chain of the neat R5 peptide from S7 to I18 is in an extended conformation. The observed secondary structures for R5 in TiO_2 and SiO_2 are relatively similar and deviate from the neat structure in similar ways. In particular, R5 in SiO_2 and in TiO_2 both have significant changes in ϕ values at the K3-K4 and K4-S5 positions. There is also a significant change in both ϕ/ψ at G13-S14. In general, most of the aforementioned large torsion angle changes in R5-TiO_2 are matched by R5-SiO_2, with the exception of K3-K4 where the change in the ϕ torsion angle in SiO_2 is not as large as in TiO_2. As a result of these torsion angle changes, both forms of mineral-associated R5 adopt extended structures of the N-terminal S2-K3-K4-S5 segment, but deviate from an extended conformation in the G6-I18 region.

In both R5-SiO_2 and R5-TiO_2, perturbations in the backbone torsion angles near S2, K3, K4, and S5 are accompanied by a large ΔCS for the side-chain of K3 and to a somewhat lesser extent in the side-chain of K4 (Figure 2.5c). It is also interesting to note that the ΔCS for the ^{13}Cζ spins in the side-chains of R16 and R17 in R5-SiO_2 and R5-TiO_2 (Figure 2.5d) are also accompanied by structural changes of the backbone in the immediate vicinity of these residues, but appear to be more modest than the structural changes that occur at and around K3 and K4. Although chemical shifts of side-chain ^{13}C spins beyond ^{13}Cβ are not correlated with protein secondary structure, a large ΔCS for these more distal sites do reflect changes in electronic environment associated with peptide precipitation with SiO_2 and TiO_2. While we cannot quantify the origins of the ΔCS for ^{13}Cγ/^{13}Cδ/^{13}Cε/^{13}Cζ spins to the degree that we can quantify the ΔCS for ^{13}CO/^{13}Cα/^{13}Cβ, we can combine our ΔCS results with data from other studies of peptide interactions with SiO_2 and TiO_2 to obtain insight into how R5 interacts with SiO_2 and TiO_2 precursors. This will be discussed further in the next section.

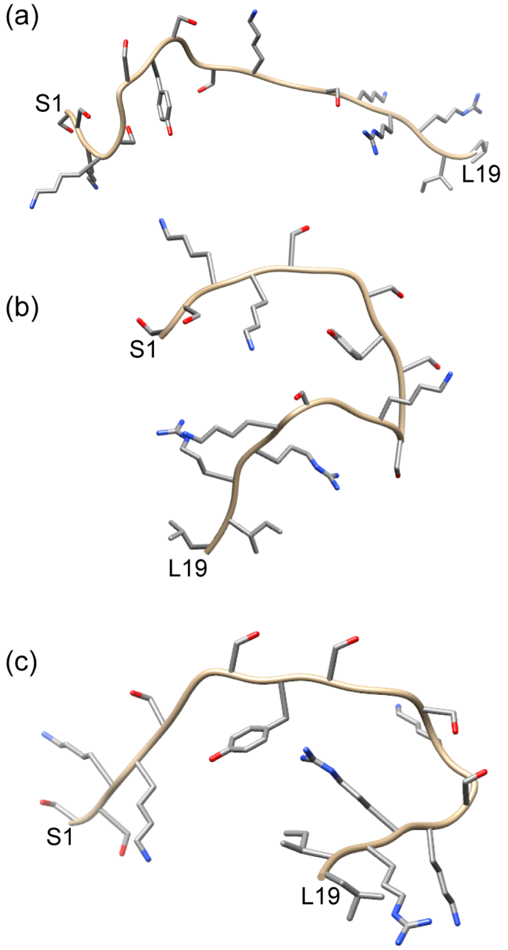

Figure 2.6. Chimera[64]-generated models of (a) R5-neat, (b) R5-TiO_2, and (c) R5-SiO_2 using TALOS-N[59]-generated torsion angles from experimentally obtained chemical shifts. The models are shown with ϕ of -119 and ψ of 113 (values consistent with the ϕ/ψ angles of surrounding residues and localized secondary structure) for the S7, Y8, and L19 positions, since the backbone chemicals shifts for these residues were not determined in this study.

2.6 DISCUSSION.

Solid-state NMR has been used extensively to study the structure and interactions of peptides in biosilica composites.[17,32,43,84–86] This is due in part to the occurrence of spin ½ nuclei in the peptide side-chains, and the occurrence of ^{29}Si, a spin ½ species with 4% natural abundance, in the mineral component, which together enable the study of peptide-silica interactions by solid-state NMR heteronuclear correlation methods. The interactions of peptides with the non-biological oxide TiO_2 are also of great interest, but solid-state NMR studies of such interactions is complicated by the fact that recoupling to ^{47}Ti and ^{49}Ti nuclei is impractical, making the heteronuclear correlation approach used in peptide-silica studies infeasible. In addition to a comparative study of R5 secondary structure in SiO_2 versus TiO_2, we have also used ^{13}C chemical shifts to probe how the R5 peptide interacts with SiO_2 and TiO_2 in the respective R5-mineral composites, as well as the degree to which the R5 peptide interacts with other components of the composite, including phosphate ions and other peptides.

The presence of the spin ½ nucleus ^{29}Si in SiO_2 makes possible direct determination of peptide-mineral contacts using heteronuclear NMR correlation methods (HETCOR), which in turn provides a means to interpret directly ΔCS trends for R5 in SiO_2 and to infer environmental origins for similar ΔCS trends for R5 in TiO_2. Several NMR studies have shown that molecules containing amine and/or amino groups make close contact with SiO_2 surfaces via these functional groups. Schmidt and coworkers[84] used ^{15}N{^{29}Si} REDOR to show that monomeric amino acids interact with SiO_2 surfaces via the NH_3^+ functional group. Brunner and coworkers[85] used ^{1}H-^{13}C-^{29}Si double CP-based HETCOR NMR techniques to show that organic polyamines in biosilica from the diatom species *Thalassiosira pseudonana* are closely associated with SiO_2. And recently Goobes and coworkers[43] used ^{1}H-^{29}Si HETCOR experiments in combination with

NMR signal enhancement via Dynamic Nuclear Polarization (DNP) to show that lysine side-chain amine protons in the peptide PL12 (KAAKLFKPKASK) co-precipitated with SiO_2 are also in close contact with the SiO_2. These NMR studies generally support the hypothesis that the ΔCS observed in the K3 and K4 side-chains of R5 in SiO_2 originate from interactions between these side-chains and the negatively charged SiO_2 surface. The general absence of significant ΔCS in the side-chains of K12 and K15 in R5-SiO_2 in turn indicate absence of interactions with SiO_2 at these sites. Furthermore, it is possible that the secondary structural rearrangements observed in the N-terminus of R5-SiO_2 co-precipitates, occur to optimize contacts between K3, K4, and the adjacent SiO_2 interface.

Significant ΔCS trends are also observed for the ^{13}Cζ spins of R16 and R17 in SiO_2. The upfield shift for the ^{13}Cζ spins in the arginine guanidinium groups may be due to SiO_2 contacts, but the absence of similar contacts at the adjacent K15 argues against this scenario. Given the affinity of guanidinium groups for phosphate ions,[86,87] the fact that R5 and other unmodified silaffin peptides will not precipitate SiO_2 in the absence of phosphate,[29] and the apparent role played by arginine residues in R5 self-assembly via phosphate bridges,[67] it is reasonable to assume that the upfield shifts we observe for the ^{13}Cζ spins in R16 and R17 in R5-SiO_2 are due to interactions with phosphate ions.

The ΔCS map for R5-TiO_2 is somewhat more complicated to interpret than that of R5-SiO_2. Studies of peptide binding to oxidized titanium surfaces find that the surface oxide film consists of amorphous and non-stoichiometric TiO_2.[72,88] In contrast to surface SiO_2 where surface hydroxyl groups have pKa's of 2.8, and thus exist predominantly as O^- at neutral pH, hydroxyl groups in TiO_2 have pKa's of 2.9 and 12.7, and thus exist as O^- and OH_2^+ at neutral pH.[72,88,89] The fact that amorphous surface films of TiO_2 will accumulate both positively charged lysine[90] and negatively charged aspartate[91] supports the amphoteric nature of TiO_2. Thus, while ^{13}C spins in the distal positions of peptide side-chains interact predominantly with acidic hydroxyl groups in SiO_2 at neutral pH, in TiO_2 peptide side-chains are exposed to a more complicated electronic environment consisting of both acidic and basic hydroxyl groups. Accordingly, there are similarities and differences in the ΔCS maps for ^{13}C spins located at the distal positions of lysine and arginine side-chains in R5-SiO_2 versus R5-TiO_2. As in R5-SiO_2, structural changes in the N-terminus of R5-TiO_2 correlate with the ΔCS in the K3 and K4 side-chains, indicating that a secondary structural change may occur to optimize contacts between peptide side-chains and TiO_2 precursors. Also, as in R5-SiO_2, the $^{13}C\zeta$ spins in the guanidinium groups of R16 and R17 in R5-TiO_2 display significant ΔCS but only modest structural changes.

There are some differences between the ΔCS observed for the $^{13}C\varepsilon$ lysine spins of K3 and K4 in R5-TiO_2 versus R5-SiO_2 that indicate differences in the two peptide-mineral interfaces. For example, while $^{13}C\varepsilon$ of K3 shows a ΔCS of almost -2 ppm in SiO_2, the same spin has a ΔCS of +6 ppm in TiO_2. Downfield chemical shift changes observed for ^{13}C spins in peptides adsorbed onto inorganic surfaces have been attributed to proximity to positive charge centers.[84] A possible explanation for the downfield shift observed for the $^{13}C\varepsilon$ in TiO_2 is that the distal portion of the lysine side-chain of K3 is laterally oriented relative to the TiO_2 surface, exposing the NH_3^+ group of the lysine side-chain to an acidic hydroxyl group, while the $^{13}C\varepsilon$ is oriented closer to a basic hydroxyl group or a Ti^{4+} ion. The same orientation of the lysine side-chain on a SiO_2 surface would result in exposure of both the NH_3^+ and the $^{13}C\varepsilon$ to acidic hydroxyl groups and an upfield shift of $^{13}C\varepsilon$ would result, as observed. The $^{13}C\zeta$ spins in R16 and R17 also have a more complicated ΔCS pattern in R5-TiO_2 than R5-SiO_2. Unlike the R5-SiO_2 system, R5 will precipitate TiO_2 in the absence of phosphate, albeit at lower levels.[79] This raises the possibility that there are alternative mechanisms for the interaction of R5 with TiBALDH, and the upfield and downfield shifts observed for the $^{13}C\zeta$ spins in R16 and R17 may result from interactions between guanidinium groups and phosphate in addition to direct interactions with TiO_2 precursors.

2.7 CONCLUSION.

This is the first solid-state NMR study of the structure and interactions of the silicifying peptide R5 in both in a biosilica composite, i.e. R5-SiO_2, and in a non-biological metal oxide composite, i.e. R5-TiO_2. This study has produced site-specific chemical shifts assignments for the majority of ^{13}CO, $^{13}C\alpha$, and $^{13}C\beta$ spins in the neat peptide, and for the peptide in the two inorganic oxides, enabling a comparative study of R5 structure in all three environments. Numerous studies conclude that lysine residues in R5 are necessary for interactions with SiO_2/TiO_2 precursors. Thus the curvatures induced in the peptide structures in the two mineral environments, which we derive from a TALOS-N[59] analysis of the ^{13}CO, $^{13}C\alpha$, and $^{13}C\beta$ chemical shifts, may function to maximize exposure of the K3 and K4 side-chains at the surface of the peptide aggregate to SiO_2/TiO_2 precursors.

This study has also acquired chemical shift assignments for the majority of the side-chain ^{13}C spins in neat R5 and for R5-SiO_2 and R5-TiO_2. The ΔCS trends for the lysine $^{13}C\varepsilon$ spins and the arginine $^{13}C\zeta$ spins in the R5-SiO_2 precipitate are interpreted using a model in which the N-terminal lysines are exposed at the surface of the peptide aggregate while the lysine $^{13}C\varepsilon$ spins nearer the C-terminus show smaller ΔCS, suggesting K12 and K15 are removed from SiO_2 contacts, while the arginine $^{13}C\zeta$ spins show ΔCS that most likely indicate contacts with phosphate anions. While the secondary structure of R5 in TiO_2 resembles the structure of the peptide in SiO_2, ΔCS trends observed for lysine $^{13}C\varepsilon$ and arginine $^{13}C\zeta$ spins in R5-TiO_2 indicate contact with a more complicated electrostatic environment, perhaps arising from proximity of some of these side-chains to acidic hydroxyl groups and others to positive charge centers.

Chapter 3. DESIGNING SERINE-LYSINE PEPTIDES FOR BIOMIMETIC TITANIA FORMATION.[3]

The demonstrated ability of peptides, such as R5, with basic and polar residues to precipitate silica and/or titania prompted the investigation into serine-lysine (S-K) peptides and titania formation. The design of short S-K peptides offers the opportunity to focus on certain peptide qualities (i.e. peptide length, primary structure, K:S ratio, contiguity of K residues, and secondary structure) and their affect on TiO_2 precipitation.

The comparative study of R5-SiO_2 and R5-TiO_2 determined that the structure of R5 within the SiO_2 and TiO_2 co-precipitates, while similar to each other, differ from the structure of neat R5. However, do to the complexity of the systems, it is difficult to assign what exactly is contributing to the structural changes; peptide-peptide interactions, peptide-buffer interactions, peptide-mineral interactions, and structural changes are all possibilities. A simpler system may aid in the understanding of the nuances of peptide-mineral interactions.

3.1 DESIGNING THE S-K PEPTIDES.

While some silaffins and segments thereof have low sequence homology, R5 is rich in both serine and lysine residues, which are essential to R5's silica-precipitating activity *in vitro*.[21,66,92] Kroger and coworkers have identified lysine rich motifs conserved in many silaffins. When examining the silaffin Sil3 from *Thalassiosira pseudonana*, they found peptide segments in both the N-terminal and C-terminal domains that exhibit a high density of five lysine residues,

---

[3] This chapter has been reproduced from Buckle, E.L.; Lum, J.; Roehrich, A.; Stote, R.; Vandermoon, B.; Dracinsky, M.; Filocamo, S.; Drobny, G.P. Serine-Lysine Peptides as Mediators for the Production of Titanium Dioxide: Investigating the Effects of Primary and Secondary Structure Using Solid-State NMR Spectroscopy and DFT Calculations. *J. Phys. Chem. B.* Manuscript JP-2018-00745p, *currently submitted.*

all with similar spacing.[93] These peptides follow the sequence KxxKxxKyKxxK, where y=1-3 residues, and are referred to as pentalysine clusters. The remaining silaffins (Sil1, Sil2, and Sil4) of *T. pseudonana* also contain pentalysine clusters. Through extensive mutation studies, Kroger found that PLC1, a pentalysine cluster from Sil1, exhibited efficient silica-targeting activity.[93] PLC1 has a higher number of hydroxylated resides than other mutants with lower silica-targeting activity, which is corroborated by the activity of T6, a highly efficient silica-targeting peptide rich in serine. They designed an artificial pentalysine cluster PLCart (KSSKSSKSSKSSK), which also demonstrates silica-targeting efficiency.[93] Goobes and coworkers precipitated silica in vitro using PL12 (KAAKLFKPKASK), a pentalysine cluster from Sil3.[43]

In addition to silaffins and their peptide fragments, many silicification methods involve the use of poly-L-lysine (PLL) chains[94,95], polyamines[20,73,96,97], peptides rich in amino groups, or amphiphilic peptides rich in lysines, such as LKα14.[32,98,99] The results of these varied silicification procedures indicate the importance of lysine residues in these processes.

Biomimetic approaches are being applied to production of other oxides, with a specific emphasis on TiO_2.[31,72–77,79,100–102] Many of these methods include the use of lysine-rich peptides or small organic amines, and have shown the importance of clusters of lysine (and arginine) residues in these SiO_2- and TiO_2- precipitating systems.[21,92,103,52] The design of the S-K peptides was inspired by these lysine-rich systems frequently encountered in the literature.

Here, we investigate the effects of primary structure of S-K peptides on TiO_2 precipitation. The relative numbers of S and K residues within the primary sequence result in TiO_2 co-precipitates of varied size and morphology. To understand how these S-K peptides direct formation of specific TiO_2 morphologies, we pair a molecular-level solid-state NMR investigation of peptide structure with resultant TiO_2 morphology and precipitation isotherm studies. We use an iterative process in which peptide sequences are modified and resulting morphologies are determined, followed by solid-state NMR (ssNMR) to characterize the structures of a selection of the S-K peptides both in their neat form and within the TiO_2 co-precipitate. We use ^{13}C cross-polarization magic-angle spinning (CP MAS) in one-dimensional (1D) and two-dimensional (2D) experiments, allowing for the assignment of chemical shifts (CS) to backbone and side-chain ^{13}C spins. The CS data is input into TALOS-N[59], which predicts torsion angles and thus provides secondary structures for these selected peptides. A comparison of CS data and secondary structure differences provides information on whether TiO_2 co-precipitation induces any changes in the peptides while also providing information on the proximity of side-chains to the TiO_2 surface. The latter properties are determined from changes in lysine side-chain ^{13}C chemical shifts observed upon precipitation with TiO_2 and quantified using Density Functional Theory (DFT) calculations. The structural forms and interactions of S-K peptides in TiO_2 composites with spherical morphology are compared to the corresponding properties of peptides in biosilica composites with similar morphology.

3.2 EXPERIMENTAL METHODS.

Trizma hydrochloride (Tris HCl) and titanium(IV)bis-(ammonium lactato)-dihydroxide (TiBALDH, 50 wt% in water) were purchased from Sigma Aldrich (St. Louis, MO) and used as received. Tiron® reagent was purchased from Fisher Scientific (Waltham, MA). When purchased, S-K peptides were custom made and supplied at > 85% purity by New England Peptide, LLC (Gardner, MA). A Thermo Scientific Megafuge 40R Centrifuge (equipped with BIOLiner microplate holders) at 4 °C for 30 minutes was used in quantification procedures. An EON microplate reader (BioTek U.S., Winooski, Vermont) was utilized to measure absorbance values. All natural and uniformly labeled ^{13}C and ^{15}N amino acids were purchased from Sigma

Aldrich (St. Louis, MO). Preloaded FMOC-protected Wang resin was purchased from EMD Millipore (Billerica, MA). All other reagents were purchased from Sigma Aldrich (St. Louis, MO) and used without purification.

3.2.1 *Peptide Synthesis.*

Peptides were either purchased from New England Peptide or synthesized on a CEM Liberty Blue peptide synthesizer using a standard 9-fluorenylmethoxycarbonyl (FMOC) and *tert*-butyl protection scheme. Preloaded FMOC-protected Wang resin was used for solid phase synthesis. Peptides were cleaved from the resin in a 10 mL solution of 95:2.5:2.5 trifluoroacetic acid (TFA): triisopropylsilane (TIS): water per 1.0 gram of peptide/resin. The resulting filtrate was added dropwise to cold *tert*-butyl methyl ether, followed by centrifugation and three rinses with 40 mL of cold *tert*-butyl methyl ether. Peptides were then dissolved in Millipore water and lyophilized, resulting in pure peptide.

3.2.2 *TiO_2 Assay.*

15 μL of TiBALDH (1% v/v) was added to a solution of 15 μL of S-K peptide (final concentration of 1 mg/mL) in 45 μL of 25 mM Tris buffer, pH 7.2 (final solution volume in microplate well is 75 μL.) The solution was incubated for 23 hours, upon which 75 μL of Tris buffer was added to double the volume (for quantification only), and the solution was incubated for an additional hour. The microplates were spun down for 30 minutes at 4 °C, and 20 μL of supernatant were removed from each well three times. The supernatant solutions were added to 180 μL of 5 mM Tiron reagent prepared with 1 M Sodium Acetate buffer, pH 4.7. Ti^{IV} depletion was monitored for 60 minutes, visualized by the formation of a yellow complex between Ti^{IV} and Tiron.[78,104] Solutions were equilibrated for one hour before absorbance values were

measured at 380 nm using an EON microplate reader (BioTek U.S., Winooski, Vermont). Data are a mean from three independent repeats.

3.2.3 *KSSKK-TiO_2 Precipitation.*

TiBALDH (1M, 0.2% by volume) was added to a solution of peptide (1 mg/mL) dissolved in 25 mM TRIS buffer, pH=7.2, and agitated for 24 hours. After centrifugation at 2500 rpm for 10 minutes, the solution was decanted. The resulting precipitate was rinsed with Millipore water 3 times and dried *in vacuo*.

3.2.4 *$SKSK_3SKS$-TiO_2 Precipitation.*

TiBALDH (1M, 10% by volume) was added to a solution of peptide (20 mg/mL) dissolved in 25 mM TRIS buffer, pH=7.2, and agitated for 24 hours. After centrifugation at 2500 rpm for 10 minutes, the solution was decanted. The resulting precipitate was rinsed with Millipore water 3 times and dried *in vacuo*.

3.2.5 *TiO_2 Nanoparticle Characterization.*

SEM images were taken on a FEI Sirion XL30 scanning electron microscope operating at variable voltages. Precipitates were dispersed onto carbon tape, mounted on aluminum studs, and sputter-coated for 60 seconds with Au/Pd.

3.2.6 *Solid-state NMR.*

All ssNMR experiments were conducted using a 16.44 T magnetic field (proton resonant field of 700.18 MHz) on a Bruker Avance III spectrometer fitted with a ^{1}H {^{13}C, ^{15}N} 3.2 mm MAS probe. The ^{13}C NMR signal was enhanced using cross-polarization (CP) with a ^{1}H-^{13}C contact time of 1.1ms and a magic-angle spinning (MAS) rate of 10 kHz ± 5 Hz was maintained with a Bruker MAS controller unit. One dimensional ^{13}C CPMAS experiments were performed with a proton 90 time of 2.75 μs and a recycle delay of 2s. The number of scans for the neat and TiO_2 complex ranged from 2k-16k. DARR[48] experiments were run with 60 ms mixing times and a recycle delay of 1.5s, with 2048 slices in the F2 dimension and 512 in F1. All chemical shifts reported were indirectly referenced to tetramethylsilane (TMS) in the solid-state using adamantane (δ=38.48).[80]

3.2.7 *Density Functional Theory (DFT) Calculations.*

The geometry of protonated *N*-acetyl-L-lysine-methylamide was optimized at the DFT level of theory, using B3LYP functional[105,106] and a standard 6-31+G(d,p) basis set. The NMR parameters were calculated using the GIAO method with polarizable continuum model used for implicit water solvation[107,108] The Gaussian16 program package was used throughout this study.[109] To estimate the effect of side-chain conformation on carbon chemical shifts, the conformation of L-lysine was systematically modified from all-*trans* conformation to a conformer with a selected C–C–C–C or C–C–C–N torsion angle changed to + or –*gauche* conformation and the geometry of the resulting structure was optimized and NMR parameters were calculated at the same computational level as described above.

A model of the TiO_2 surface was based on anatase structure. A cluster of six Ti atoms and 18 O atoms was cut out of the structure and nine hydrogen atoms were put on dangling oxygen atoms on the ‘inner face’ of the cluster, no hydrogen atoms were put on three ‘surface face’ oxygens leaving the total charge of the cluster –3.

3.3 EFFECTS OF PRIMARY STRUCTURE ON TiO_2 PRECIPITATION.

The effects of K:S ratio and contiguity of K residues on TiO_2 precipitation activity are explored through the design of a series of S-K peptides and their corresponding TiO_2 precipitation activity. The array was designed to test the impact of (1) an increasing number of lysine residues with a constant number of serine residues and (2) the number of contiguous lysine residues, achieved by changing the position of the serine residues. Ti^{IV} depletion was monitored for 60 minutes using a colorimetric assay, visualized by the formation of a yellow complex between Ti^{IV} and Tiron.[78,104] Absorbance values were measured at 380 nm and used to determine the percentage of reacted Ti^{IV}. The results of the TiO_2 precipitation assays are summarized in Table 3.1, along with the resultant morphologies determined via SEM (images not shown).

Table 3.1. Peptide Sequences with their Percentage of Reacted TiBALDH and Resultant TiO_2 Morphologies upon Co-precipitation.

Peptide	**K:S Ratio**	**Contiguous K Residues**	**% TiBALDH reacted (stdev)**	**TiO_2 Morphology**
$SKSK_3SKS$	1.25	3	97 (1)	spheres
KSSKK	1.5	2	22 (5)	spheres
$(SKSK_3)_2$	2	3	49 (22)	fused particles
$(SK_4S)_2$	2	4	34 (13)	amorphous
K_3SKSK_3	3.5	3, 3	42 (18)	fused particles
SK_8S	4	8	74 (2)	fused particles
S_2K_8	4	8	73 (4)	fused particles
S_2K_9	4.5	9	38 (14)	amorphous
SK_9S	4.5	9	44 (16)	amorphous
SK_5SK_4	4.5	5, 4	39 (15)	amorphous
SK_2SK_7	4.5	2, 7	57 (21)	amorphous
$SKSK_9$	5	9	44 (17)	fused particles
SK_5SK_5	5	5, 5	57 (19)	spheres

With the exception of $SKSK_3SKS$, peptides with a higher K:S ratio show greater TiO_2 precipitation activity, especially when the K residues are localized (i.e. SK_8S). $SKSK_3SKS$ seems to be an anomaly as the most efficient peptide tested, converting 97% of TiBALDH into TiO_2. Only three of the peptides assayed, KSSKK, SK_5SK_5, and $SKSK_3SKS$, produce consistent spherical morphologies, making them of special interest. Two of these peptides, $SKSK_3SKS$ and KSSKK, both of which form spherical morphologies but display the highest ($SKSK_3SKS$) and lowest (KSSKK) percentages of TiBALDH reacted, are investigated further.

Figure 3.1 shows an SEM image of the KSSKK-TiO_2 co-precipitate (Figure 3.1a) and a corresponding size distribution histogram (Figure 3.1b). The co-precipitates are approximately spherical with a mean diameter of 201 ± 46 nm. The $SKSK_3SKS$-TiO_2 co-precipitates are also approximately spherical (Figure 3.1d), but have a mean diameter of 511 ± 202 nm, on average 300 nm larger than the KSSKK-TiO_2 nanostructures. Although many of the $SKSK_3SKS$-TiO_2 particles fall within a size range of 400-600 nm (Figure 3.1e), the nanospheres are relatively polydisperse in comparison to those of the KSSKK-TiO_2 co-precipitates.

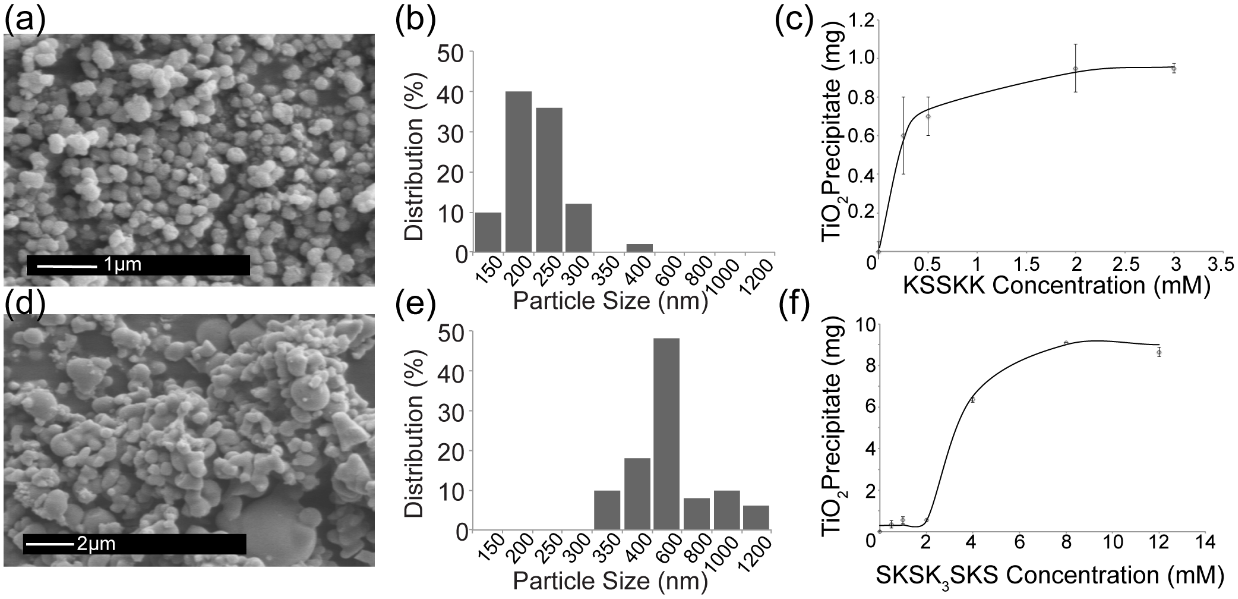

Figure 3.1. (a) SEM image of KSSKK-TiO_2 co-precipitates showing spherical morphologies with a mean diameter of 201 ± 46 nm. (b) Size distribution histogram for KSSKK-TiO_2 co-precipitates. Particle sizes are measured using ImageJ.[81] (c) TiO_2 produced as a function of KSSKK concentration. The concentration of TiBALDH was held constant at 2 mM. Data are a mean of two independent repeats. (d) SEM image of $SKSK_3SKS$-TiO_2 co-precipitates showing spherical morphologies with a mean diameter of 511 ± 202 nm. (e) Size distribution histogram for $SKSK_3SKS$-TiO_2 co-precipitates. Particle sizes are measured using ImageJ.[81] (e) TiO_2 produced as a function of $SKSK_3SKS$ concentration. The concentration of TiBALDH was held constant at 0.1 M. Data are a mean of two independent repeats.

Precipitation curves were also obtained for varying concentrations of KSSKK and $SKSK_3SKS$, with TiBALDH held at constant concentrations of 2mM and 0.1 mM, respectively. These precipitation curves are shown in Figure 3.1c and Figure 3.1f. A striking feature of these data is that the precipitation curves have markedly different forms. The KSSKK precipitation curve in Figure 3.1c has roughly hyperbolic form with TiO_2 precipitate appearing at relatively low concentrations of peptide. In contrast the $SKSK_3SKS$ data in Figure 3.1f appear to follow sigmoidal behavior with little or no precipitate appearing until peptide concentration reaches

2mM, and then rises rapidly. Hyperbolic and sigmoidal precipitation curves are generally attributed to non-cooperative and cooperative mechanisms, respectively. These data are discussed further below.

3.4 SKSK$_3$SKS CHEMICAL SHIFT ASSIGNMENTS AND STRUCTURE ANALYSIS.

In order to gain insight into the secondary structure of SKSK$_3$SKS-neat and SKSK$_3$SKS embedded within the TiO$_2$ co-precipitate, we make site-specific ^{13}C chemical shift assignments for the entire peptide using five ^{13}C and ^{15}N enriched samples (Table 3.2). Both 1D ^{13}C CP MAS and 2D DARR ^{13}C-^{13}C experiments were performed on SKSK$_3$SKS -neat and -TiO$_2$. All 1D ^{13}C CP MAS spectra are show in Appendix B. The downfield region (larger ppm) contains the carbonyl ^{13}C spins, and the upfield region (smaller ppm) contains the aliphatic ^{13}C spins (^{13}Cα, ^{13}Cβ, ^{13}Cγ, ^{13}Cδ, and ^{13}Cε). Stacked plots allow for the direct comparison of chemical shift and peak shape between the two peptide states: neat and co-precipitated with TiO$_2$.

Table 3.2. SKSK$_3$SKS peptides synthesized in this study. (*) Indicates that the preceding amino acid is uniformly ^{13}C and ^{15}N enriched.

Sample Name	**Label Position**
S1K2	S*K*SKKKSKS
S3K4	SKS*K*KKSKS
K5	SKSKK*KSKS
K6S7	SKSKKK*SKS
K8	SKSKKKSK*S

The stacked 1D plots highlight the peak broadening upon co-precipitation with TiO$_2$. When broadening this severe occurs, it is not possible to unambiguously assign all chemical shifts; 2D spectroscopy is required. This need for 2D spectroscopy is further emphasized through Figure 3.2. In the 1D CP MAS (Figure 3.2a), we are not able to resolve each shift, as there is overlap in both the carbonyl and aliphatic regions. However, with 2D ^{13}C-^{13}C DARR (Figure 3.2b), we can resolve and assign all of the ^{13}C shifts, which are provided in Appendix B.

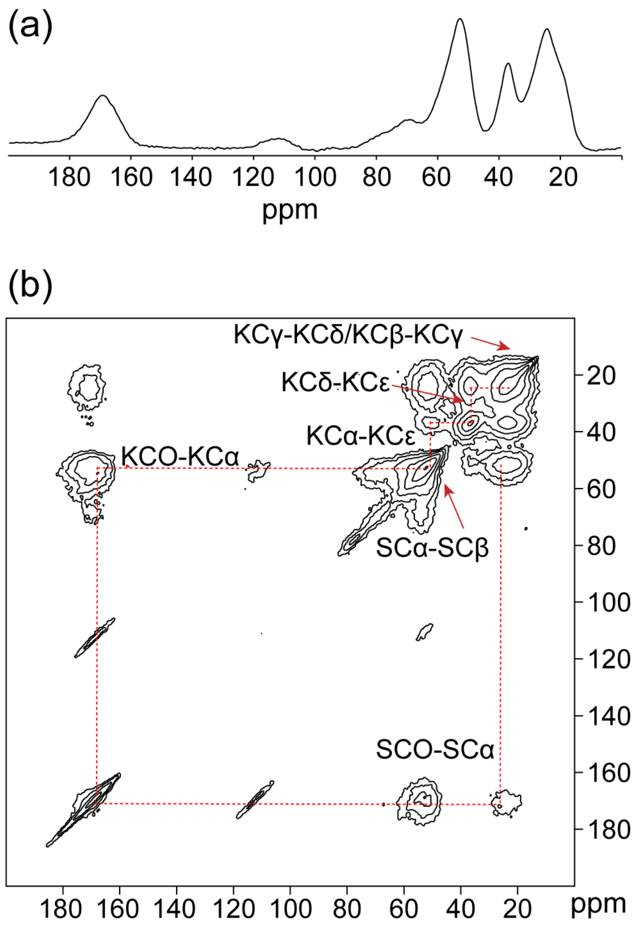

Figure 3.2. (a) ^{13}C CP MAS NMR of SKSK$_3$SKS S1K2 TiO$_2$. (b) ^{13}C-^{13}C DARR of SKSK$_3$SKS S1K2 TiO$_2$. Cross peaks are labeled for ease of identification.

Once all ^{13}C shifts are assigned for both the neat and TiO$_2$-embedded peptide, changes in backbone and side-chain chemical shifts (ΔCS) are analyzed. ^{13}C chemical shift perturbations of the backbone carbons (^{13}CO, ^{13}Cα, and ^{13}Cβ) are typically associated with a change in secondary structure, which can result from co-precipitation with TiO$_2$, while side-chain perturbations can be attributed to peptide aggregation, proximity to the TiO_2 surface, or buffer effects. To study the degree of perturbation of ^{13}C chemical shifts, ΔCS values are obtained by subtracting the CS of the ^{13}C spin in neat $SKSK_3SKS$ from the corresponding ^{13}C spin in the $SKSK_3SKS$-TiO_2 co-precipitate. A positive ΔCS indicates a downfield perturbation (higher ppm, less shielded), while a negative ΔCS indicates an upfield perturbation (lower ppm, more shielded). Bar charts of both backbone and side-chain ΔCS values are shown in Figure 3.3.

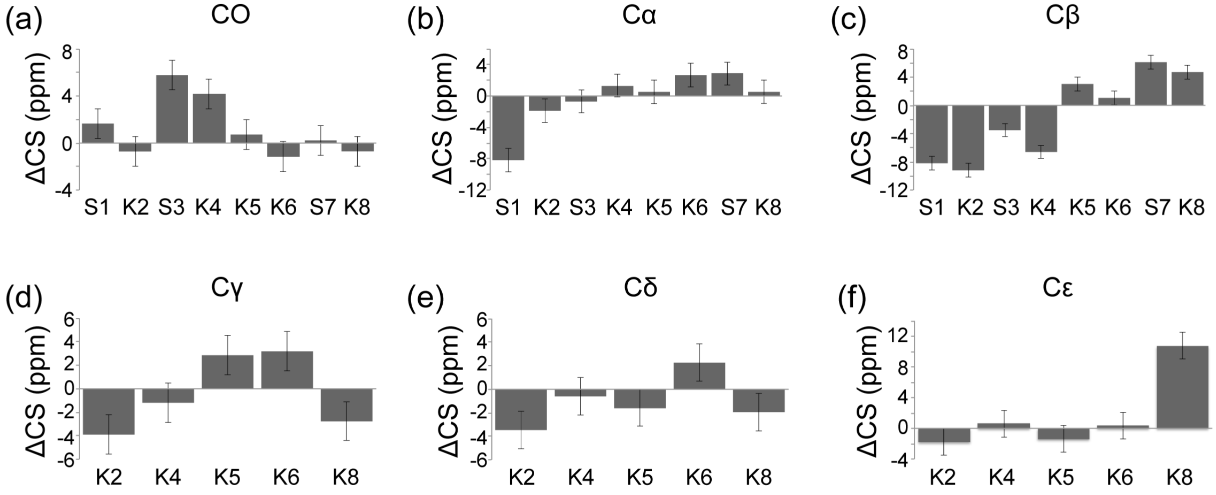

Figure 3.3. ΔCS plots for $SKSK_3SKS$ showing chemical shift perturbations for (a) ^{13}CO shifts, (b) $^{13}C\alpha$ shifts, (c) $^{13}C\beta$ shifts, (d) $^{13}C\gamma$ shifts, (e) $^{13}C\delta$ shifts, and (f) $^{13}C\varepsilon$ shifts. ΔCS values for $SKSK_3SKS$ co-precipitated with TiO_2 are in reference to the neat peptide. Positive changes indicate a downfield shift while negative changes indicate an upfield shift.

There are significant backbone CS perturbations upon co-precipitation with TiO_2, occurring at the S1 $^{13}C\alpha$, S3 ^{13}CO, K4 ^{13}CO, K6 $^{13}C\alpha$, S7 $^{13}C\alpha$, and all $^{13}C\beta$ shifts except K6. These ΔCS values are quite large in magnitude, indicating significant structural changes in these regions, particularly around the N-terminus. There are also significant ΔCS for the side-chains of

SKSK$_3$SKS. ^{13}Cγ perturbations occur at K2, K5, K6, and K8, ^{13}Cδ perturbations occur at K2 and K6, and ^{13}Cε perturbations occur at K8, which has a large downfield shift of 10.7 ppm.

The CS values for the ^{13}CO, ^{13}Cα, and ^{13}Cβ spins are input into TALOS-N[59], which generates output files containing predicted torsion angles (Appendix B). These torsion angles are used to visualize the secondary structure of SKSK$_3$SKS-neat and SKSK$_3$SKS-TiO$_2$ using Chimera[64] (Figure 3.4). In the neat peptide, the entire chain is extended in random coil. However, upon co-precipitation with TiO$_2$, the chain kinks at K2, causing S1 and S3 to fold inwards, exposing the K2 side-chain. These perturbations are accompanied by large ΔCS for S1 backbone ^{13}C spins as well as K2 ^{13}Cβ, ^{13}Cγ, and ^{13}Cδ (see Figure 3.3). It is interesting to note that K2 does not experience a significant ΔCS perturbation at ^{13}Cε. The S7 and K8 residues at the C-terminus also experience CS perturbations accompanied by structural changes, albeit more modest than

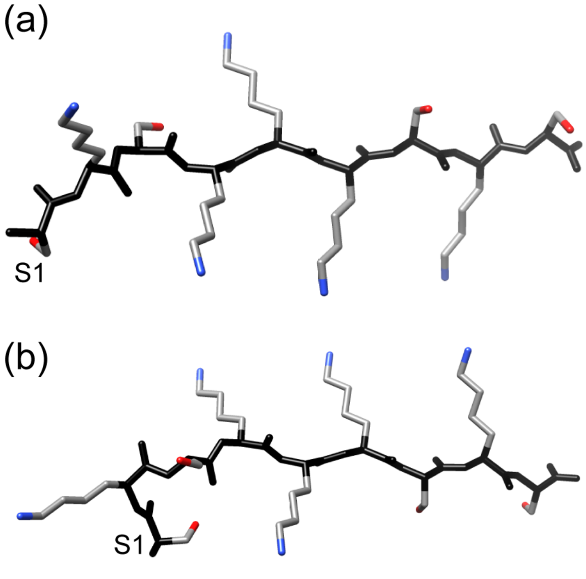

Figure 3.4. Chimera[64]-generated models of (a) SKSK$_3$SKS neat and (b) SKSK$_3$SKS-TiO$_2$ using TALOS-N[59] –generated torsion angles from experimentally obtained chemical shifts.

those observed at S1-K3. These structural changes could result in a greater exposure of the K8 side-chain, which experiences a large ΔCS at ^{13}Cε, a perturbation typically associated with interactions with a mineral surface.[37,57,58] In addition, the side-chains of K4, K6, and K8 are all oriented on the same side of the peptide, which could be conducive to TiO_2 binding.

3.5 KSSKK CHEMICAL SHIFT ASSIGNMENTS AND STRUCTURE ANALYSIS.

Analogous to the $SKSK_3SKS$ system, 1D ^{13}C CP MAS and 2D DARR ^{13}C-^{13}C experiments are utilized to make site-specific ^{13}C chemical shift assignments (Appendix B) for the both the KSSKK-neat and KSSKK-TiO_2 peptides using two isotopically enriched samples (Table 3.3).

Table 3.3. KSSKK peptides synthesized in this study. (*) Indicates that the preceding amino acid is uniformly ^{13}C and ^{15}N enriched.

Sample Name	**Label Position**
K1S2	K*S*SKK
S3K4	KSS*K*K

Figure 3.5 shows the 1D ^{13}C CP MAS spectra for KSSKK in both peptide states: neat and co-precipitated with TiO_2. The peak shapes remain very similar for the neat and co-precipitated form for both the K1S2 and S3K4 samples. The extent of line broadening is not as severe as for the $SKSK_3SKS$ spectra upon co-precipitation with TiO_2, yet there is still peak overlap in the carbonyl and aliphatic regions. In order to unambiguously assign all ^{13}C spins, 2D ^{13}C-^{13}C DARR spectra are collected. As with the $SKSK_3SKS$ peptide, ΔCS are used to gain insight into the structural conformations and perturbations of the neat and embedded peptides.

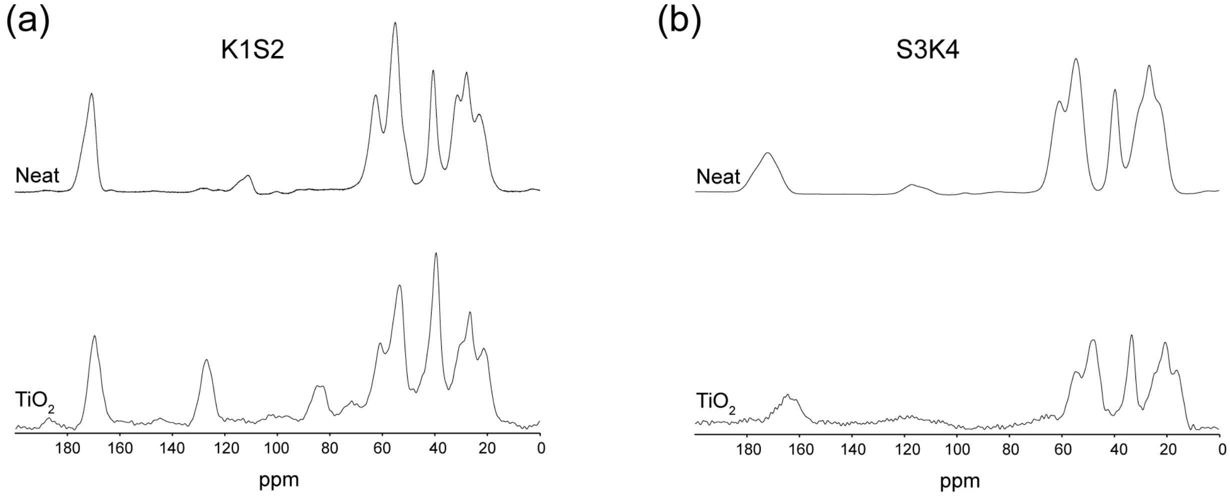

Figure 3.5. Stacked 1D ^{13}C CP MAS spectra for (a) K1S2 and (b) S3K4 in their neat and TiO$_2$ co-precipitated forms.

The ΔCS plots for KSSKK are shown in Figure 3.6. No significant ΔCS values are observed for any of the ^{13}CO spins. Many of the remaining backbone ΔCS range from 0-2 ppm, but more significant perturbations are observed for the S2 ^{13}Cα (5.9 ppm), S2 ^{13}Cβ (9.1 ppm), the S3 ^{13}Cα (4.4 ppm), and the K4 ^{13}Cβ (-2.8 ppm) shifts, indicating secondary structure changes around S2 and K4, changes that are seen in a similar region of the SKSK$_3$SKS peptide. In addition, there is a side-chain perturbation of -4.2 ppm in the K4 ^{13}Cδ shift. Interestingly, although the ^{13}Cε of K1 shows an upfield shift of about 1 ppm, there is virtually no change in the chemical shift of the ^{13}Cε spin of K4 upon co-precipitation with TiO$_2$. This apparent difference in the surface orientations of closely spaced lysine side-chains will be considered in the section on DFT calculations.

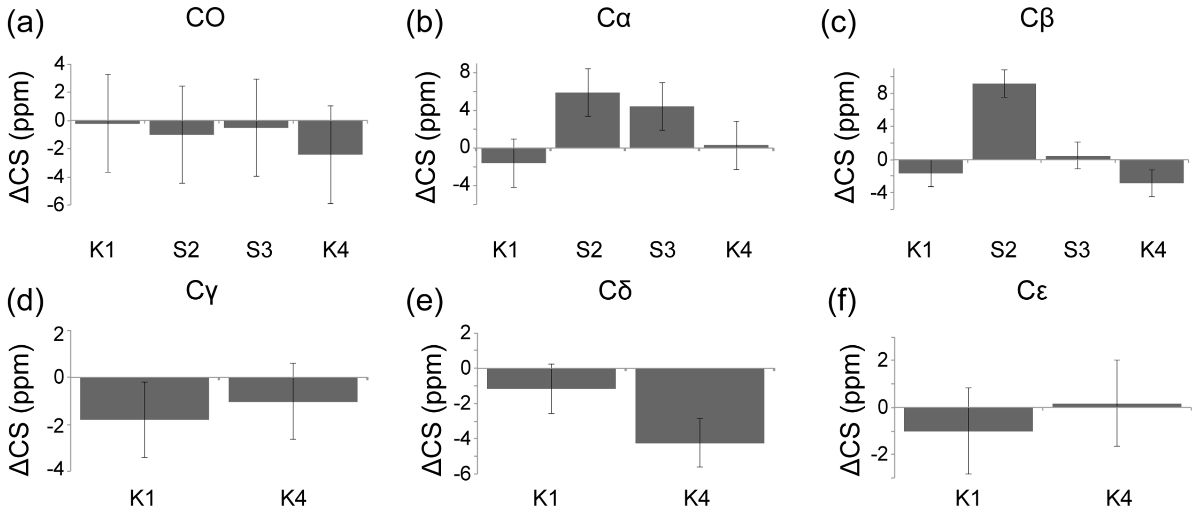

Figure 3.6. ΔCS plots for KSSKK showing chemical shift perturbations for (a) ^{13}CO shifts, (b) ^{13}Cα shifts, (c) ^{13}Cβ shifts, (d) ^{13}Cγ shifts, (e) ^{13}Cδ shifts, and (f) ^{13}Cε shifts. ΔCS values for KSSKK co-precipitated with TiO_2 are in reference to the neat peptide. Positive changes indicate a downfield shift while negative changes indicate an upfield shift.

TALOS-N[59] and Chimera[59] are used to visualize the secondary structure of KSSKK-neat and KSSKK-TiO_2 (Figure 3.7). φ/ψ torsion angle values are shown in the Appendix B. The N-terminus around S2 and K3 shows a mild conformational change, consistent with the observed backbone ΔCS, while the C-terminus remains relatively unchanged. The overall conformational changes upon co-precipitation with TiO_2 are minor, and do not seem to alter the exposure of any side-chains. This is reflected in the ΔCS, where few significant perturbations are observed in the K1 or K4 side-chain ^{13}C spins, the exception being the K4 ^{13}Cδ shift. Perhaps due to the small size of the peptide, significant conformational changes are not required to catalyze the nucleation of TiO_2, and side-chains are already oriented in a way to maximize exposure.

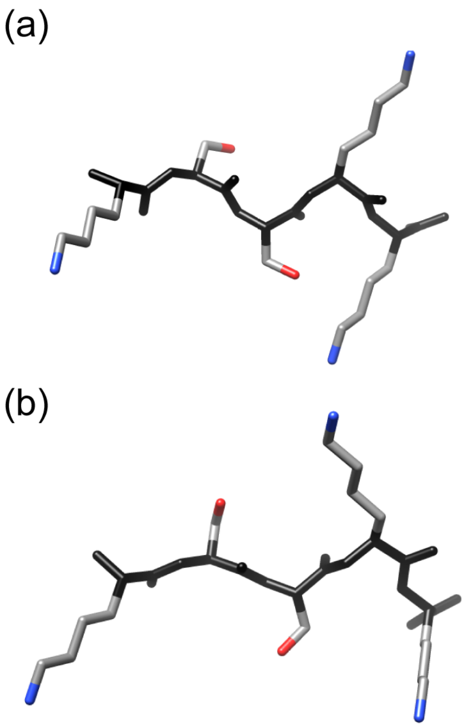

Figure 3.7. Chimera[59]-generated models of (a) KSSKK neat and (b) KSSKK-TiO_2 using TALOS-N[59] –generated torsion angles from experimentally obtained chemical shifts.

3.6 DFT CALCULATIONS.

The secondary structures and interactions of peptides in co-precipitates with SiO_2 have been studied extensively with ssNMR techniques. [31,37,57,58,60-62] A common approach in ssNMR studies of peptides in biosilica composites is to use heteronuclear correlation methods to directly determine peptide-SiO_2 contacts. ^{29}Si is a spin ½ nucleus with a natural abundance of 4.7 %,[43,85] so it is frequently used in heteronuclear correlation as a target nucleus within the oxide component for recoupling to ^{13}C and ^{15}N spins in protein side-chains. However, ssNMR studies of peptide-TiO_2 composites are more problematical due in part to lack of a nuclear spin within the inorganic oxide, which can serve as a target for dipolar recoupling experiments. ^{47}Ti and ^{49}Ti are both NMR-active Ti isotopes, but have small gyromagnetic ratios, low natural abundances, and relatively large quadrupole moments, all resulting in low detection sensitivity. Due to these factors, direct measurements of peptide interactions with the TiO_2 surface via heteronuclear dipolar recoupling experiments from spin ½ nuclei in protein side-chains, such as ^{13}C or ^{15}N, to ^{47}Ti and ^{49}Ti are not practical.

To probe peptide – TiO_2 interactions in S-K peptides we use ΔCS data obtained from ^{13}C spins in peptide side-chains to detect changes in the electronic environment of the peptide upon co-precipitation with TiO_2. Because TiO_2 activity is observed to scale with the number of primary amines in the R5 peptide[21] we concentrate analysis on ΔCS effects observed for $^{13}C\gamma$, $^{13}C\delta$, and $^{13}C\varepsilon$ spins of lysine side-chains. We assume however that ΔCS effects in peptide-inorganic oxide composites can have a number of origins, so to clarify the physical circumstances that give rise to these side-chain chemical shift perturbations we use Density Functional Theory calculations. Protein side-chains may undergo conformational changes when adapting to mineral surfaces. In Table 3.4 are compiled DFT calculations of chemical shift changes for lysine side-chain $^{13}C\gamma$, $^{13}C\delta$, and $^{13}C\varepsilon$ spins that result from conformational changes of the side-chain. In Table 3.4, $\gamma\pm60$ indicates a change of the CαCβ-CγCδ dihedral angle by ±60 degrees. Similarly, $\delta\pm60$ and $\varepsilon\pm60$ indicate ±60 degree changes of the CβCγ−CδCε and CγCδ−CεNζ dihedral angles, respectively. All entries are in ppm, with positive numbers indicating downfield chemical shift changes and negative numbers indicating upfield chemical shift changes relative to the all-trans side-chain conformation.

Table 3.4. The influence of lysine side-chain conformation on the chemical shifts of the ^{13}Cγ, ^{13}Cδ, and ^{13}Cε spins (ppm). Positive table entries indicate downfield chemical shift perturbations with respect to the all trans conformation.

	γ-60	γ60	δ-60	δ60	ε-60	ε60
Cγ	-3.53	0.95	-0.64	-0.75	-0.74	-0.84
Cδ	-3.18	-2.77	-1.07	-0.99	-1.29	-1.27
Cε	0.48	0.37	-0.77	-0.60	0.62	0.54

In ssNMR studies of surface adsorbed amino acids and peptides, upfield perturbations of lysine side-chain ^{13}C chemical shifts (i.e. $\Delta CS<0$), and ^{13}Cε in particular, have been attributed to interactions with negative charges in mineral surfaces.[57,58] Recently, Guo and Holland used a combination of ssNMR and DFT calculations to elucidate the adsorption state of lysine on fumed silica surfaces.[110] They modeled the interaction of lysine with the silica surface as a lysine-silanol complex and calculated ^{15}N and ^{13}C chemical shifts for lysine free and in the complex. Based on a comparison between calculated and experimental chemical shifts it was concluded that the lysine amine is the dominant hydrogen bonding interaction with the surface silanol groups.[110]

To address the possibility that lysine amines in KSSKK and SKSK$_3$SKS similarly form interactions with hydroxyl groups in peptide-TiO$_2$ composites, DFT calculations of lysine side-chain ^{13}C chemical shift perturbations were performed for varying distances between the side-chain amine nitrogen and the nearest surface hydroxyl oxygen. These calculations were made for two side-chain orientations relative to the TiO$_2$ surface. Results are shown in Figure 3.8. Figure 3.8a shows chemical shift perturbations as a function of distance between amine nitrogen and surface hydroxyl oxygen for a perpendicular alignment of the lysine side-chain relative to the TiO$_2$ surface. For this surface orientation, a DFT calculation shows a 2-3 ppm upfield perturbation of the ^{13}Cε chemical shift and weaker downfield perturbations of the ^{13}Cγ and ^{13}Cδ chemical shifts when the amine N to surface hydroxyl O distance approaches 4 Angstroms. Figure 3.8b shows ΔCS effects calculated for ^{13}C spins in a lysine side-chain that approaches a TiO_2 surface in a parallel orientation. The parallel orientation is much less conducive to hydrogen bond formation between the lysine side-chain amine and surface hydroxyl groups. Accordingly, the DFT calculations in Figure 3.8b show that the pattern of ΔCS effects in the parallel side-chain orientation differs markedly from the pattern observed for the perpendicular side-chain orientation in Figure 3.8a. The most significant difference is that the 2-3 ppm upfield shift of the ^{13}Cε spin observed in the perpendicular orientation is not observed for the parallel orientation. In contrast the parallel orientation shows modest downfield shifts for the ^{13}Cγ and ^{13}Cε spins while the ^{13}Cδ spin shows large upfield shifts. The upfield shift observed for the ^{13}Cδ spin is due to the proximity of the ^{1}Hδ spin to the TiO_2 surface, although the 2.5 ppm upfield shift corresponding to a N-O distance of 3 Angstroms is somewhat too small for an H-bond interaction. For a more realistic N-O distance of 3.8-4.0 Angstroms, the upfield shift for ^{13}Cδ is calculated to be in the range 0.5-1.0 ppm.

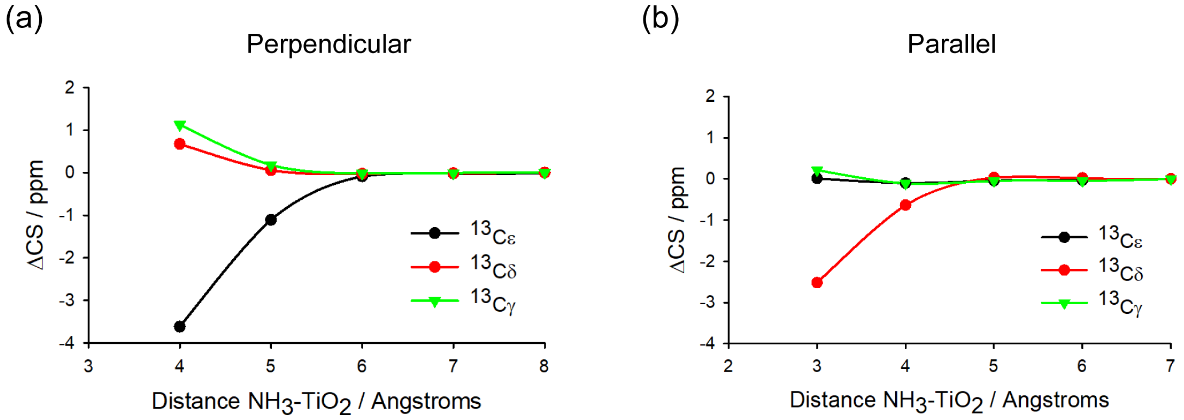

Figure 3.8. DFT calculation of lysine side-chain ^{13}C chemical shift perturbations (ΔCS) as a function of the distance between the lysine amine nitrogen and the surface hydroxyl oxygen for (a) a perpendicular orientation of the lysine side-chain relative to the TiO_2 surface and (b) a parallel orientation of the lysine side-chain relative to the TiO_2 surface. An upfield perturbation of a ^{13}C chemical shift is indicated by ΔCS<0 and a downfield perturbation is therefore indicated by ΔCS>0.

3.7 DISCUSSION.

^{13}CO, ^{13}Cα, and ^{13}Cβ chemical shift data indicate both S-K peptides $SKSK_3SKS$ and KSSKK are in extended secondary structures in neat form and largely remain in extended structures in TiO_2 composites. Significant ΔCS effects observed for ^{13}CO, ^{13}Cα, and ^{13}Cβ spins are confined to the termini of both the $SKSK_3SKS$ and KSSKK peptides. For the KSSKK system, perturbations of the ^{13}Cα and ^{13}Cβ of S2 are accompanied by a small conformational change at S2-K4 as well as a ΔCS for ^{13}Cδ of K4. It is possible that the structural rearrangement at S2-K4 acts to better orient the side-chain of K4 for interactions with the TiO_2 surface.

The pattern of side-chain ^{13}C chemical shift perturbations in K1 differs from the pattern observed in K4. For K1, the chemical shift of ^{13}Cε is perturbed upfield by about 1 ppm (i.e.

ΔCS=-1 ppm), the chemical shift of ^{13}Cδ is also perturbed upfield by about 1 ppm, while the upfield perturbation of ^{13}Cγ is somewhat larger at about 1.8 ppm. In the case of ^{13}Cε the ΔCS= -1ppm is in the range expected for a N-O distance of about 4-5 Å, assuming the side-chain approaches the TiO_2 surface with the three-fold symmetry axis of the side-chain amine group directed perpendicular to the surface as shown in Figure 3.8. On the other hand, the upfield ΔCS effects observed at ^{13}Cγ and ^{13}Cδ for K1 do not agree with what is expected if the lysine side-chain maintains an all-trans conformation when oriented with the amine group directed toward the TiO_2 surface as shown in Figure 3.8a. The upfield ΔCS effects observed at ^{13}Cγ and ^{13}Cδ are likely due to a conformational change of the side-chain as it approaches the TiO_2 surface.

In the case of K4, the ^{13}Cε chemical shift is only weakly perturbed while 1-4 ppm upfield ΔCS effects are observed at ^{13}Cγ and ^{13}Cδ. The negligible change in the chemical shift of ^{13}Cε precludes a close association with the TiO_2 surface at least not in the orientation assumed in the DFT calculations shown in Figure 3.8a. The fact that both ^{13}Cδ and ^{13}Cγ are shifted upfield precludes an orientation of the type shown in Figure 3.8b. This pattern of ΔCS effects likely indicates conformational change of the K4 side-chain upon co-precipitation with TiO_2, possibly involving a change of the CαCβ-CγCδ dihedral angle in the range ±60 degrees, which would exert only a small downfield change in the chemical shift of ^{13}Cε.

Chemical shift trends observed for the five lysine side-chains in $SKSK_3SKS$ indicate a more complex interaction with the TiO_2 mineral phase than is the case with KSSKK. ΔCS trends for ^{13}CO, ^{13}Cα, and ^{13}Cβ in the S1-K4 region indicate a backbone conformational change upon co-precipitation with TiO_2, but the rest of the backbone maintains an extended secondary structure. The ΔCS values observed for the ^{13}Cε, ^{13}Cδ, and ^{13}Cγ spins in the five lysine side-chains vary. For example, upon co-precipitation with TiO_2, the side-chain of K2 ^{13}Cε is shifted upfield by about 2 ppm (ΔCS=-2ppm) while ^{13}Cδ and ^{13}Cγ show upfield chemical shift perturbations of about 3-3.5 ppm. The upfield perturbation of the ^{13}Cε chemical shift again very likely indicates an interaction with the TiO_2 surface. Assuming an orientation as shown in Figure 3.8a, the observed ca. 2ppm upfield shift corresponds to a N-O distance of about 4.5 Å. The 3-3.5 ppm upfield chemical shift perturbations observed for the ^{13}Cγ and ^{13}Cδ spins in K2 may be due to a conformational change of the side-chain, most likely a ca. 60 degree change of the CαCβ-CγCδ dihedral angle.

The ΔCS trends observed for ^{13}Cγ/^{13}Cδ/^{13}Cε in K4 differ markedly from those observed in K2. ΔCS effects are small for both ^{13}Cε and ^{13}Cδ with a 1.0 ppm upfield shift of ^{13}Cγ. At K5 the chemical shift of ^{13}Cε changes in the upfield direction by 2.0 ppm (ΔCS=-2.0ppm) upon co-precipitation with TiO_2, and a change of the chemical shifts of ^{13}Cδ and ^{13}Cγ by -1 ppm and 2 ppm, respectively. K6 shows a small change in the chemical shift of ^{13}Cε upon co-precipitation with TiO_2, while both ^{13}Cγ and ^{13}Cδ show downfield shifts of between 2-3 ppm. The trend in K8 is different still with ^{13}Cγ and ^{13}Cδ showing upfield chemical shift perturbations in the 2-3 ppm range upon co-precipitation with TiO_2 while ^{13}Cε shows a large downfield shift.

Although the ^{13}C chemical shift data are not conclusive with regard to the nature of interactions between these $SKSK_3SKS$ and TiO_2, DFT calculations reported in this work and experimental and computational studies reported elsewhere indicate that lysine side-chains interact strongly with TiO_2 surfaces.[72,89,111] Therefore it is not surprising that in many cases upfield perturbations are observed for ^{13}Cε spins in $SKSK_3SKS$ peptide-TiO_2 co-precipitates. However, if the $SKSK_3SKS$ peptides were dispersed as monomers within a matrix of TiO_2, it might be expected that the ^{13}Cε spins would experience similar electronic environments and in such cases all lysine side-chains would display chemical shift trends of the types shown in Figure

3.8. But in the $SKSK_3SKS$ peptide the chemical shift perturbations observed for $^{13}C\varepsilon$ spins in the lysine side-chains vary considerably with K2 and K5 showing upfield perturbations expected for side-chains in close proximity to TiO_2 surfaces with perpendicular orientations, while K4 and K6 show only weak perturbations indicating these spins are remote from the surface or deviate from perpendicular orientation. The large downfield perturbation to the chemical shift of $^{13}C\varepsilon$ in K8 is striking because none of the DFT results in Table 3.4 or Figure 3.8 account for the significant downfield shifts for lysine side-chain ^{13}C spins. Downfield perturbations of side-chain spins have been observed in peptide-silica composites and have been attributed to peptide-peptide aggregation.[17,23,32,43]

Self-assembly of high phosphorylated silaffins has been observed and proposed as a mechanism for catalyzing silica formation[72]. The self-assembly hypothesis has been extended to the silaffin-derived peptide R5 to explain its SiO_2 forming[30] and TiO_2 forming[21] activities. The ΔCS data obtained in this study do not provide direct proof of the existence of SK peptide aggregates in TiO_2 composites, but in the recent ssNMR study of the R5 peptide in SiO_2 and TiO_2 composites[22], the variation in lysine side-chain chemical shift perturbations is suggestive of differential exposure of the protein side-chains to TiO_2, which in turn may be the result of self assembly of the monomeric peptides into aggregates which persist in the solid composite.

This interpretation of the ΔCS data for the two peptides is supported by DFT calculations, and also by the precipitation curves in Figure 3.1. In Figure 3.1c, the precipitation curve of KSSKK is hyperbolic in form, with TiO_2-peptide composite precipitating at extremely low concentrations of peptide, before reaching saturation at a peptide concentration of about 2mM. In contrast the precipitation curve for $SKSK_3SKS$, shown in Figure 3.1f, is sigmoidal, with no appreciable amounts of precipitate forming until a peptide concentration of 2mM is reached. The curve for SKSK$_3$SKS saturates at about 8mM. The higher activity of SKSK$_3$SKS is not surprising given the larger number of K residues, but the different curve shapes requires explanation. Various factors have been discussed as causes for variation in peptide isotherm curve shapes. For example, adsorption isotherms for small peptides onto negatively charged silica surfaces differ markedly for cationic versus anionic or uncharged peptides, with the cationic peptides adsorbing at low concentrations onto silica particles at higher levels than anionic or neutral peptides at similar concentrations.[73] Given that both peptides in this study are cationic, the difference in the precipitation curves of KSSKK and SKSK$_3$SKS may be better explained by other mechanisms, including the occurrence of an equilibrium between monomeric peptides and peptide aggregates.[74,75] In cases where interactions between peptide side-chains and inorganic oxide precursors compete with peptide-peptide interactions, sigmoidality of the isotherm is favored by higher populations of aggregate versus monomer, whereas hyperbolic behavior is favored by higher populations of monomer.[75] Also in self-aggregating systems, if aggregation does not result in a loss of peptide sites (lysine side-chains) for interacting with oxide precursors, hyperbolic behavior is approached as the affinities of precursor for monomer and polymer become equivalent. Departures from hyperbolic behavior increase as interactions between precursors and monomer and aggregate become inequivalent. Therefore, a plausible explanation for the difference between the precipitation curves of KSSKK and SKSK$_3$SKS is the existence of a monomer-aggregate equilibrium, where the populations of monomer versus aggregate differ between the two peptide samples, where affinities of oxide precursors for sites on the monomer versus aggregate may differ between the two samples, and where precursor-peptide interactions compete with peptide-peptide interactions. The latter condition would require that the sites on the peptide for interactions with precursors are close to or identical to sites for peptide-peptide interactions.[75]

3.8 CONCLUSION.

Although S-K peptides have been reported earlier to induce silica formation from solutions of silicic acid, this is the first study of S-K peptides as catalysts for the mineralization of a non-biological oxide, i.e. TiO_2. This study has assayed a series of S-K peptides of varying lengths, primary structures, K:S ratios, and TiO_2 precipitation activities. Two of these peptides ($SKSK_3SKS$ and KSSKK) have similar K:S ratios but different lengths, display very different precipitation activities, but produce similar TiO_2 morphologies, albeit with different particle size distributions. In addition, precipitation curves differ markedly; the curve for KSSKK has hyperbolic form and the curve for $SKSK_3SKS$ displays sigmoidal form.

Unlike silica or hydroxyapatite, TiO_2 lacks a nuclear spin species which can be incorporated into heteronuclear dipolar correlation experiments, so quantitative determination of distances between ^{13}C and ^{15}N spins in peptide side-chains to spins in the oxide surface via dipolar interactions is impractical. Instead, in this study the sensitivity of chemical shifts of lysine side-chain ^{13}C and ^{15}N spins to charged oxide surfaces have been used in place of dipolar recoupling experiments to determine peptide-surface proximity and orientation. Qualitative trends in ΔCS of side-chain spins observed upon co-precipitation with TiO_2 have been quantified using DFT computations and have enabled interpretation of side-chain spin ΔCS trends in terms of changes in peptide side-chain conformation, orientation and proximity to TiO_2 surfaces.

For both peptides upfield shifts for some lysine $^{13}C\varepsilon$ spins indicate contact between the mineral. But in both peptides some $^{13}C\varepsilon$ spins show little chemical shift perturbation or, in the case of lysine side-chains near the C-terminus in $SKSK_3SKS$, show downfield perturbations. These results indicate that the peptide side-chains are not uniformly exposed to the mineral but are possibly in aggregated states, which may as a result remove some side-chains from close contact with the mineral surface. Recent ssNMR studies indicate that R5 may similarly aggregate in the presence of phosphate to form TiO_2 from TiBALDH solutions.[23] That KSSKK shows a hyperbolic precipitation curve may indicate that this peptide has a lower population of aggregate versus monomer than is the case with $SKSK_3SKS$, although there are alternative explanations such peptide-peptide and peptide-TiBALDH interactions occurring independently[75] while these interactions may occur competitively in $SKSK_3SKS$. If the chemical shift patterns observed for the S-K peptides in this study indicate that these peptides similarly aggregate in the course of forming TiO_2, then they do so in the absence of phosphate. The nature of peptide-peptide interactions in these composite systems is the subject of future studies.

Chapter 4. SURFACE ADSORPTION OF THE SN_A15 PEPTIDE.

4.1 INTRODUCTION.

Many organisms are capable of producing inorganic materials (i.e. calcite, silica, and hydroxyapatite) through a process known as biomineralization. These organisms contain specialized proteins, which interact with biomineral surfaces to accelerate[112], inhibit[113,114], or shape[19,20,28,29,115–117] the nucleation, growth, and structure of hard tissues, such as bone, teeth, and shells. However, it is often not clear how these proteins interact with the mineral surface, although it is thought that protein secondary structure is crucial.[99,118,119] Furthermore, NMR, SFG, and NEXAFS studies suggest that amino acid side-chains directly interaction with biominerals.[34,38–40,120–127] Studying the molecular-level interactions between proteins and inorganic minerals is crucial to understanding the processes of biomineral surface recognition and control of hard tissue growth. Furthermore, an enhanced understanding of how proteins recognize and adhere to mineral surfaces could lead to the development of new materials with enhanced biocompatibility.

Statherin, a small 43-residue salivary protein with the sequence DpSpSEEKFLRRIGRFGYGYGPYQPVPEQPLYPQPYQPQYQQYTF, inhibits the precipitation of calcium phosphate minerals and hydroxyapatite (HAP) crystal growth.[128] Statherin has been widely studied by adsorption isotherms,[33,129] solution NMR,[130,131] ssNMR,[17,34–36,38–40,122,124,126,127,132] and circular dichroism,[33,133] and its structure is known neat and adsorbed onto HAP.[33–36] Upon adsorption, the N-terminal binding domain adopts an α-helical conformation.[36,134,135]

The N-terminus of statherin contains acidic residues, including phosphoserine (pS), aspartic acid (D), and glutamic acid (E), which have been shown to be essential for HAP binding.[33] $^{13}C\{^{31}P\}$ REDOR experiments measured the distance between the δ-carboxyl ^{13}C spins of residues E4, E5, and E26 and ^{31}P spins on the HAP surface.[122] Ndao et. al. found that E4 and E26 were farther from the surface than E5, which had a ^{13}C-^{31}P distance of about 4.25 Å.[122] Furthermore, $T_{1\rho}$ experiments show that E4 and E5 have more restricted motion than E26.[122] The internuclear distances paired with the relaxation experiments indicate that E5 is closely interacting with the HAP surface, while E26 is likely far from the surface of HAP. Another $^{13}C\{^{31}P\}$ REDOR experiment modeled the binding of poly-aspartic acid (PD) to HAP,[136] and the strong dephasing of the side-chain γ-carboxyl ^{13}C spin indicates close binding to the surface. This can be extrapolated to glutamic acid residues, as the only difference in the side-chains is a methylene group, thus supporting Ndao's results. The random coil conformation in the acidic domain of statherin could allow most of these residues to interact with the HAP surface, an observation supported by rigid dynamics in this region.[134]

The effects of basic residues on HAP binding have also been studied. Mutations of the basic residues to alanine lowered the binding affinity, but did not affect the surface coverage or the adsorption enthalpy.[34] However, simultaneous replacement of all of the basic residues (K6, R9, R10, and R13) with alanine did significantly lower the adsorption equilibrium and surface coverage. Goobes et. al. hypothesized that individually, the basic residues were not essential for binding, but as a group, they acted to decrease the overall peptide charge and reduce repulsive interactions.[34]

Many studies have also been conducted on the role of the phenylalanine residues,[38,39,126,137] which have the highest affinity to HAP of the four hydrophobic residues (L, I, G, F).[137] The side-chain of F14 is closer to the surface than F7, and is also more constrained, indicating that F14 likely interacts with the HAP surface via its aromatic ring.

Many of these studies have focused on the first 15 residues of statherin, referred to as SN15. Adsorption studies have shown that SN15 has nearly the same binding affinity for HAP, even when the phosphoserine residues are replaced by aspartic acid (SNa15).[33] Despite this, not much research has been conducted on SNa15. This thesis uses adsorption isotherms and ssNMR to study the binding of SNa15 to multiple inorganic surfaces, including HAP, SiO_2, and TiO_2. It aims to answer the following questions:

- What is the structure of surface-bound SNa15?
- What part of SNa15 interacts with each surface?
- How is SNa15 oriented on each surface?
- How does the structure/interactions of adsorbed SNa15 change as a function of mineral surface?

^{13}C and ^{15}N CP MAS and ^{13}C-^{13}C DARR experiments and TALOS-N[59] –predicted torsion angles are used to characterize the secondary structures of SNa15 neat (i.e. lyophilized from Millipore water) and adsorbed to each of the three surfaces. The perturbation of side-chain ^{13}C and ^{15}N chemical shifts is used to obtain information on the proximity of various residues and on the orientation of SNa15 to each surface. Finally, the results for each surface are compared to each other and to recent work on the structure of statherin and SN15 adsorbed on HAP.

4.2 EXPERIMENTAL METHODS.

All natural amino acids were purchased from Sigma Aldrich (St. Louis, MO). All uniformly ^{13}C and ^{15}N labeled amino acids were purchased from Cambridge Isotope Laboratories (Tewksbury, MA). Preloaded FMOC-protected Wang resin was purchased from EMD Millipore

(Billerica, MA). All other reagents were purchased from Sigma Aldrich (St. Louis, MO) and used without purification.

4.2.1 *Peptide Synthesis.*

Peptides were synthesized on a CEM Liberty Blue peptide synthesizer using a standard 9-fluorenylmethoxycarbonyl (FMOC) and *tert*-butyl protection scheme. Preloaded FMOC-protected Wang resin was used for solid phase synthesis. Peptides were cleaved from the resin in a 10 mL solution of 95:2.5:2.5 trifluoroacetic acid (TFA): triisopropylsilane (TIS): water mixture per 1.0 gram of peptide/resin. The resulting filtrate was added dropwise into cold tert-butyl methyl ether, followed by centrifugation and three rinses of the resulting solids with 40 mL of cold tert-butyl methyl ether. Peptides were purified using RP-HPLC (Varian ProStar HPLC, Alltima WP C4 column, 5 mL/min, eluent A: water with 0.2% TFA, eluent B: acetonitrile with 0.2% TFA), using a gradient of 15-50% B over 40 minutes. Chromatograms were generated by observing the UV absorbance at 254 nm, and the analyte was verified by mass spectrometry. The fractions were then lyophilized, resulting in the pure peptide.

4.2.2 *Surface Area Determination.*

The surface area of the HAP, SiO_2, and TiO_2 nanoparticles was determined using a Nova 4200e Surface Area and Pore Size Analyzer from Quantachrome Instruments. BET measurements showed a surface area of 34.4 m^2/g for HAP, 331.9 m^2/g for SiO_2, and 28.6 m^2/g for TiO_2 nanoparticles.

4.2.3 *Adsorption Isotherms.*

Known concentrations of SNa15 (1ml) were equilibrated with 10 mg of HAP, SiO_2, or TiO_2 nanoparticles for 4 hours in phosphate buffer (100mM, pH=7.4). After adsorption, the solid nanoparticles were separated from the mixture via centrifugation at 13000 x g for 15 minutes. The peptide concentrations in the supernatant solutions were measured using an Agilent 8453 Diode Array UV-Vis Spectrophotometer and compared with the initial concentrations.

4.2.4 *Solid-state NMR Sample Preparation.*

SNa15 (2mM, 5ml) was equilibrated with 60 mg of mineral nanoparticle for 4 hours in phosphate buffer (100mM, pH=7.4). After adsorption, the solid was separated from the mixture via centrifugation at 13000 x g for 15 minutes. The supernatant was discarded, and the remaining solid was dried *in vacuo*.

4.2.5 *Solid-state NMR.*

All solid-state NMR experiments were conducted using a 16.4 T magnetic field (proton resonant field of 700.18 MHz) on a Bruker Avance III spectrometer fitted with a ^{1}H {^{13}C,^{15}N} 3.2 mm MAS probe. The Larmour frequency at this field is 176.07 MHz for ^{13}C and is 70.95 MHz for ^{15}N. The spinning speed for all experiments is 15 kHz ± 5Hz, and is regulated by a Bruker MAS controller unit. All experiments were run at room temperature.

The basic CP pulse program is shown in Figure 1.5. For ^{15}N CP MAS, the second channel (labeled ^{13}C in Figure 1.5) was switched to ^{15}N. Pulse lengths and powers were optimized on ^{13}C, ^{15}N -enriched glycine. 1D ^{13}C CP MAS experiments were collected using a 4 μs proton $\pi/2$ pulse, a contact time of 1.2 ms, and a recycle delay of 2 s. Neat samples required 2k scans while adsorbed samples required 8k scans. 1D ^{15}N CP MAS experiments were collected using a 4 μs proton $\pi/2$ pulse, a contact time of 2 ms, and a recycle delay of 2 s. Neat samples required 4k scans while adsorbed samples required 32 k scans. All ^{13}C chemical shifts reported were indirectly referenced to tetramethylsilane (TMS) in the solid-state using adamantane (δ=38.48 ppm).[80] All ^{15}N chemical shifts reported were indirectly referenced to NH_3^+ in the solid-state using glycine (δ=33.4 ppm).[138]

2D ^{13}C-^{13}C DARR experiments were collected with a 1.2 ms contact time, a 4 μs proton π/2 pulse, and a 4 μs ^{13}C π/2 pulse. Mixing times were 60 ms. For neat samples, there were 256 points in the indirectly detected dimension (F1) and 1k points in the directly detected dimension (F2). For adsorbed samples, there were 128 points in F1 and 1k points in F2. The chemical shifts reported were indirectly referenced to tetramethylsilane (TMS) in the solid-state using adamantane (δ=38.48 ppm).[80]

4.3. ADSORPTION ISOTHERMS.

To determine how SNa15 interacts with the SiO_2 and TiO_2 surfaces, Langmuir adsorption isotherm curves were measured (Figure 4.1). Isotherms for SNa15 interacting with HAP can be

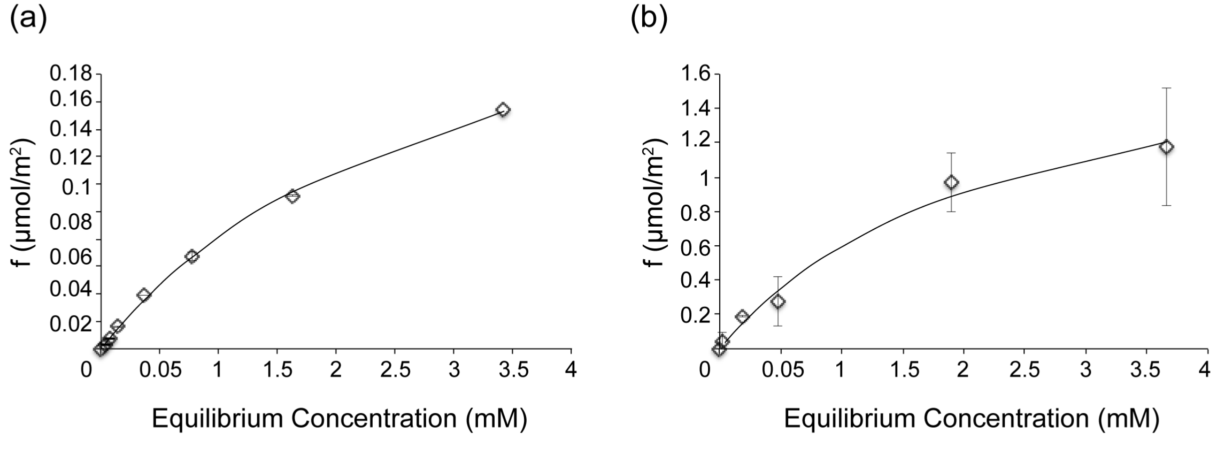

Figure 4.1. Adsorption isotherms for SNa15 interacting with (a) SiO_2 and (b) TiO_2. Data are a mean from two independent repeats, and the standard deviation is shown. The disassociation constants obtained from the fitting are: $K_d = 2.98$ mM for SiO_2 and $K_d = 2.30$ mM for TiO_2.

found in the literature.[33] The curves were fit with Equation 4.1, where K_d is the disassociation constant, f is the fractional saturation, A is a scaling factor, and [SNa15] is the concentration of free SNa15 (equilibrium concentration). The K_d obtained from these data were 2.98 mM and

$$f = A\frac{[SNa15]}{[SNa15]+K_d} \tag{4.1}$$

2.30 mM for SNa15 adsorbing onto SiO_2 and TiO_2, respectively. The maximum amounts of SNa15 adsorbed were 0.2 μmol/m² and 1.2 μmol/m² for SiO_2 and TiO_2, respectively.

4.4. CHEMICAL SHIFT ASSIGNMENTS.

1D ^{15}N CP MAS and 1D ^{13}C CP MAS experiments were performed in conjunction with 2D ^{13}C-^{13}C DARR experiments in order to obtain site-specific chemical shift assignments. We resolved and assigned most of the ^{13}C spins and the side-chain ^{15}N spins in SNa15 containing up to two uniformly ^{13}C- and ^{15}N-enriched amino acids. The structures of the amino acids examined are shown in Figure 4.2.

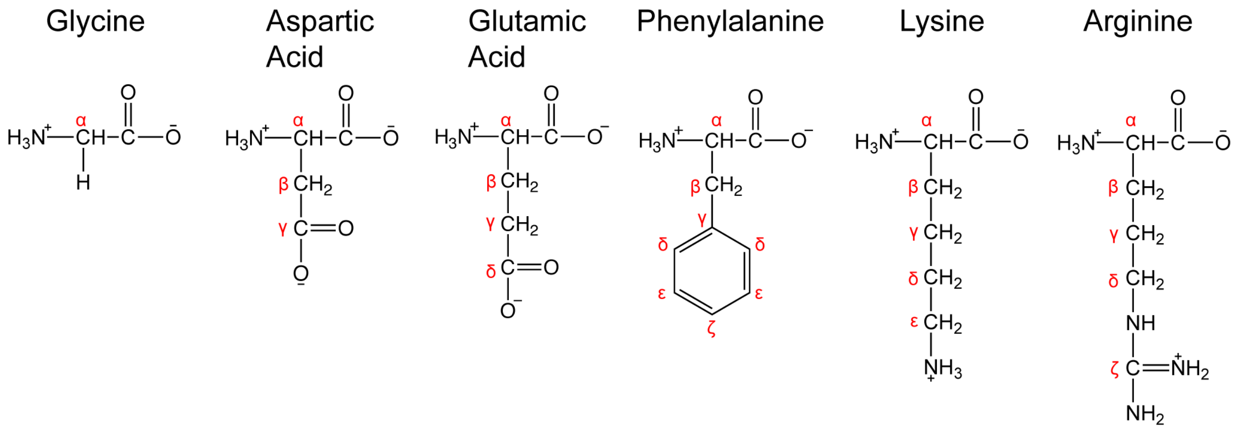

Figure 4.2. Structures of the amino acids for which chemical shift assignments are made in SNa15. Structures are shown for neutral pH (pH=7). Conventional side-chain atom labels are shown.

To assign the chemical shifts for the entire peptide, seven isotopically enriched samples were analyzed, as shown in Table 4.1. The only amino acids not assigned by this study are D1, L8, I11, and the C-terminal G15.

Table 4.1. SNa15 peptides synthesized in this study. (*) Indicates that the preceding amino acid is uniformly ^{13}C and ^{15}N enriched.

Sample Name	Label Position
D2R9	DD*DEEKFLR*RIGRFG
D3R10	DDD*EEKFLRR*IGRFG
E4F7	DDDE*EKF*LRRIGRFG
E5F14	DDDEE*KFLRRIGRF*G
K6	DDDEEK*FLRRIGRFG
G12	DDDEEKFLRRIG*RFG
R13	DDDEEKFLRRIGR*FG

An example of the data collected for each sample is shown in Figure 4.3. A 1D ^{15}N CP MAS (Figure 4.3a), 1D ^{13}C CP MAS (Figure 4.3b), and 2D ^{13}C-^{13}C DARR (Figure 4.3c) spectrum was collected for each sample in order to make complete, unambiguous chemical shift assignments. The ^{15}N amide spins had too much overlap and were therefore not able to be unambiguously assigned, so only the ^{15}N side-chain spins were assigned.

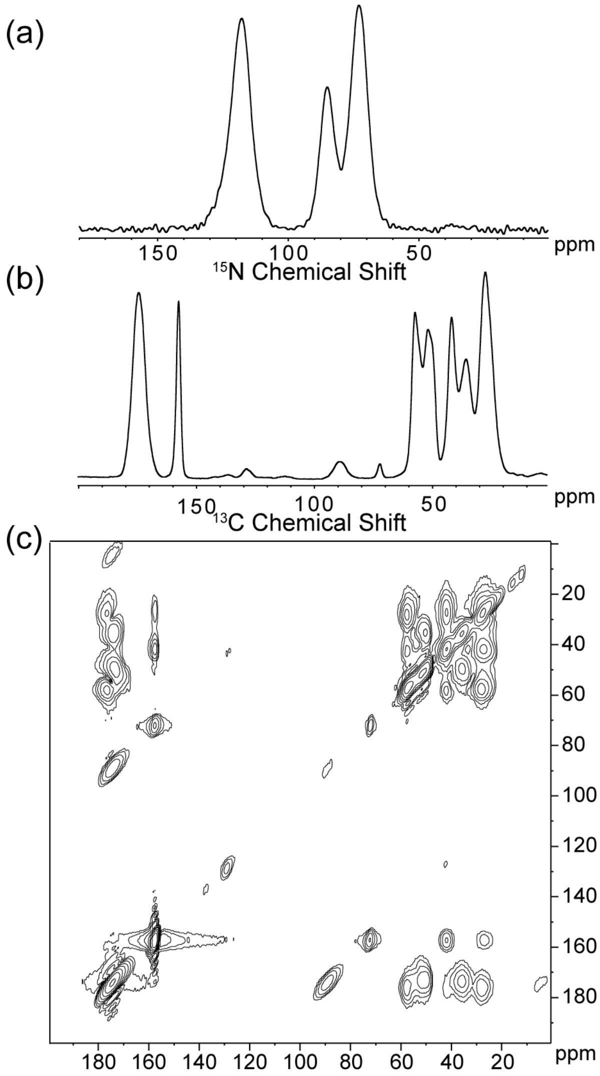

Figure 4.3. Representative set of the data collected for each labeled SNa15 peptide in each of the studied phases: neat and adsorbed on HAP, SiO_2, and TiO_2. The data shown are for neat D2R9 and are the following: (a) ^{15}N CP MAS, (b) ^{13}C CP MAS, and (c) ^{13}C-^{13}C DARR.

As evident in Figure 4.3, the broad nature of the ^{13}C lineshapes and the overlap in both carbonyl and aliphatic regions renders 2D spectroscopy necessary. Figure 4.4 illustrates how all chemical shift assignments are made for the entire neat SNa15 peptide. As discussed in Chapter 1, Section 3.3, the diagonal peaks in a DARR spectrum divide the spectrum into two nearly symmetrical halves. On either side of the diagonal are the cross-peaks, which result from the interaction of two distinct nuclei. The cross-peak interactions are highlighted by the dashed red lines and labeled with the corresponding ^{13}C spins. These correlations allow for the assignment of unique chemical shifts. All ^{13}C chemical shift assignments were made via this method for the entire SNa15 peptide in the four phases studied: neat, adsorbed on HAP, adsorbed on SiO_2, and adsorbed on TiO_2.

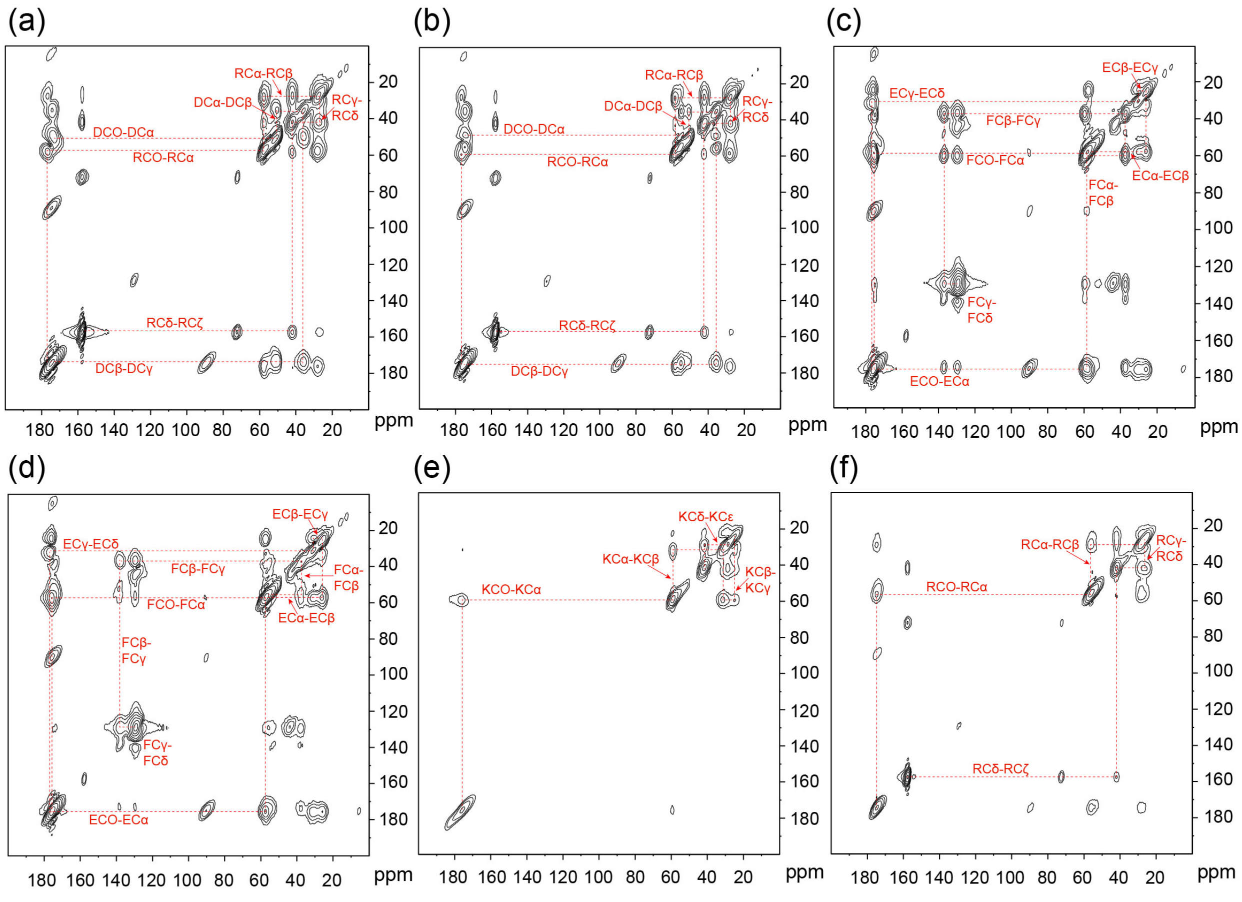

Figure 4.4. ^{13}C-^{13}C DARR spectra of neat (a) D2R9, (b) D3R10, (c) E4F7, (d) E5F14, (e) K6, and (f) R13. The dashed lines show the correlation of spins.

Chemical shift changes (ΔCS) for backbone and side-chain ^{13}C nuclei can provide information on the structural changes of the peptide as well as the changes in local environment experienced upon adsorption. Figure 4.5 shows the differences in ^{13}C chemical shifts of D2R9 in the four phases studied. The dashed lines emphasize the more obvious chemical shift differences between these spectra. It should also be noted that upon adsorption, the resolution in the aliphatic region significantly decreases. This is yet another reason why 2D spectroscopy was required.

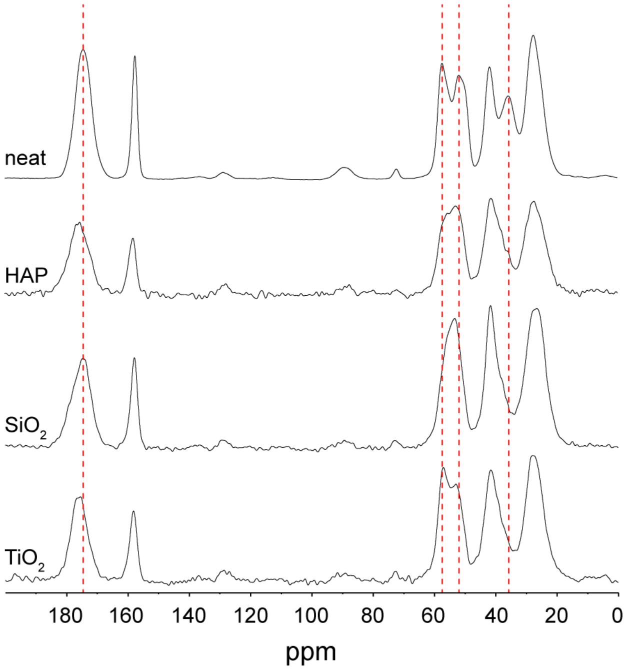

Figure 4.5. ^{13}C CP MAS spectra of D2R9 in four phases: neat, adsorbed to HAP, adsorbed to SiO_2, and adsorbed to TiO_2. The dashed lines highlight some of the more obvious chemical shift differences between the four spectra.

ΔCS for backbone and side-chain ^{13}C nuclei in the neat versus in adsorbed samples occur to varying degrees at sites along the peptide backbone and side-chains. The ^{13}C chemical shift perturbations of the backbone ^{13}CO, ^{13}Cα, and ^{13}Cβ chemical shifts are typically associated with a change in secondary structure as a result of adsorption. To systematically study the degree to which SNa15 ^{13}C chemical shifts are perturbed upon adsorption to HAP, SiO_2, and TiO_2, ΔCS values are calculated. ΔCS is obtained by subtracting the chemical shift of the ^{13}C spin in neat SNa15 from the corresponding ^{13}C spin in the adsorbed SNa15 peptide. A positive ΔCS indicates a downfield perturbation of the chemical shift (higher ppm, less shielded), while a negative ΔCS indicates an upfield perturbation of the chemical shift (lower ppm, more shielded). Bar charts of backbone ΔCS values are shown in Figure 4.6.

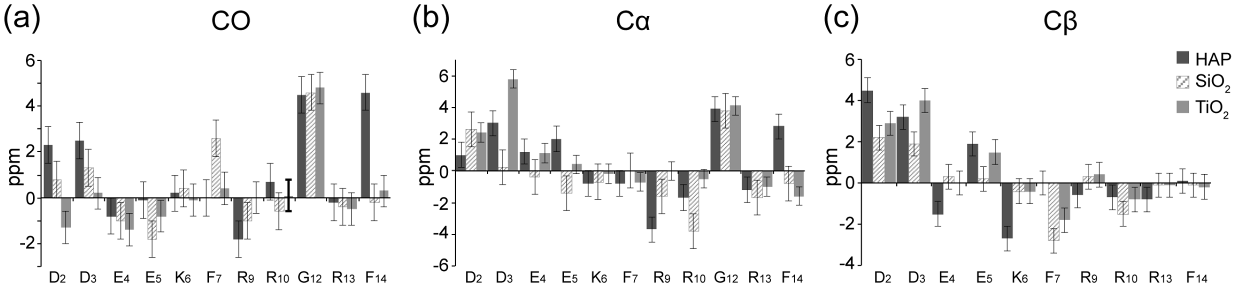

Figure 4.6. Backbone ΔCS plots showing chemical shift perturbations for (a) ^{13}CO shifts, (b) ^{13}Cα shifts, and (c) ^{13}Cβ shifts. ΔCS for SNa15 on HAP (black), SiO_2 (hatched), and TiO_2 (gray) are in reference to neat SNa15. Positive changes indicate a downfield shift while negative changes indicate an upfield shift relative to the neat peptide.

Commonalities in ΔCS for ^{13}CO between the three adsorbed phases occur at E4 (all upfield shifts) and G12 (all downfield shifts). All three adsorbed phases also experience a large downfield shift for G12 ^{13}Cα. Additionally, they all experience a pronounced downfield shift for the ^{13}Cα spin of D2 and the ^{13}Cβ spins of D2 and D3 and a pronounced upfield shift for the ^{13}Cα spin of R13 and the ^{13}Cβ spin of R10. The similarities in ΔCS in these residues indicate similar structural changes in these regions between neat SNa15 and SNa15 adsorbed on each surface.

Specifically, the N-terminus (D2-E4) and the C-terminus (R10, G12, and R13) experience similar conformational changes upon adsorption to HAP, SiO_2, and TiO_2.

There are also pronounced backbone ΔCS changes for SNa15 that are unique to each mineral phase, or shared only between 2 of the mineral phases. These differences highlight the unique regional conformation of SNa15 adsorbed to each mineral phase. This will be explored further in Sections 4.5 and 4.6.

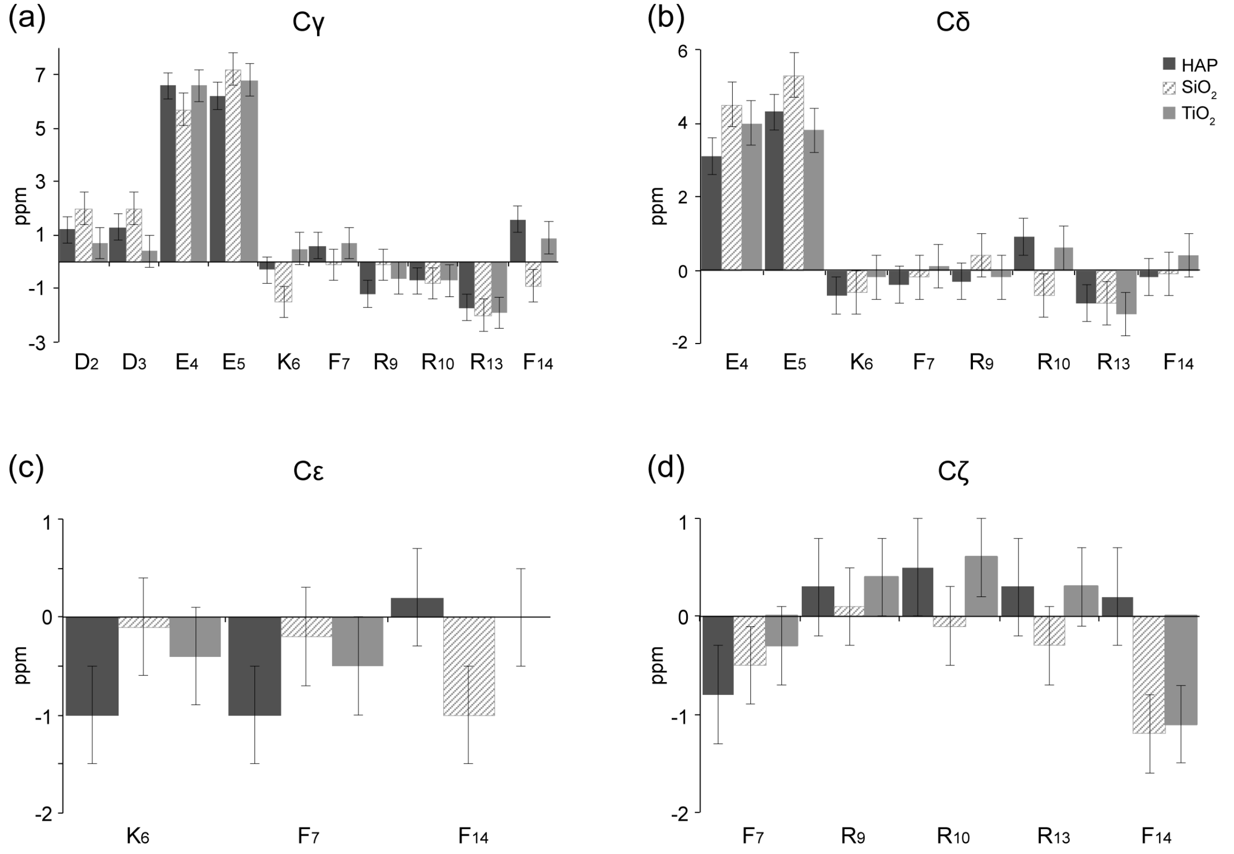

Figure 4.7. Side-chain ΔCS plots showing chemical shift perturbations for (a) ^{13}Cγ shifts, (b) ^{13}Cδ shifts, (c) ^{13}Cε shifts, and (d) ^{13}Cζ ΔCS. ΔCS for SNa15 on HAP (black), SiO_2 (hatched), and TiO_2 (gray) are in reference to neat SNa15. Positive changes indicate a downfield shift while negative changes indicate an upfield shift relative to the neat peptide.

Bar charts of ^{13}C side-chain ΔCS values are shown in Figure 4.7. SNa15 experiences downfield shifts for the ^{13}Cγ of D2 and D3 and the ^{13}Cδ of E4 and E5 upon adsorption to all three mineral surfaces. These spins correspond to the side-chain carboxyl groups in the aspartic acid and glutamic acid residues in the N-terminus of SNa15. The acidic N-terminus of statherin is widely accepted as essential to binding. A study of poly-L-glutamic acid (PG) showed that the side-chain carboxyl group (^{13}Cδ) experiences downfield shifts upon adsorption to SiO_2 and HAP.[83] The decreased shielding of the carboxyl groups indicates an interaction with positively-charged surface sites.[83] These results can also be extrapolated to aspartic acid. The side-chain carboxyl chemical shift changes for D2, D3, E4, and E5 suggest similar close associations with each of the mineral surfaces. The carboxyl ^{13}C shifts of E4 and E5 are also accompanied by large downfield shifts of the ^{13}Cγ spins for SNa15 upon adsorption to all three mineral surfaces. This is also likely due to close proximity to each mineral surface.

The basic residues of SNa15 (K6, R9, R10, and R13) generally experience less pronounced and less consistent perturbations across the three surfaces. There is a consistent upfield shift for both the ^{13}Cγ and ^{13}Cδ spins of R13 in SNa15 adsorbed to each mineral surface. There is also an upfield shift of the ^{13}Cε spin of K6 upon adsorption to HAP and TiO_2, although not SiO_2. Typically, upfield shifts of lysine ^{13}Cε spins indicate proximity to a negatively-charged mineral surface.[83] These modest perturbations likely indicate a minimal role in surface-adsorption. Mutation studies of the 4 basic residues (K6, R9, R10, R13) of statherin have shown that individually, none are crucial to binding.[34] However, as a group they act to decrease the overall charge of statherin, thus reducing repulsive protein-protein interactions and promoting a higher surface affinity and coverage.[34]

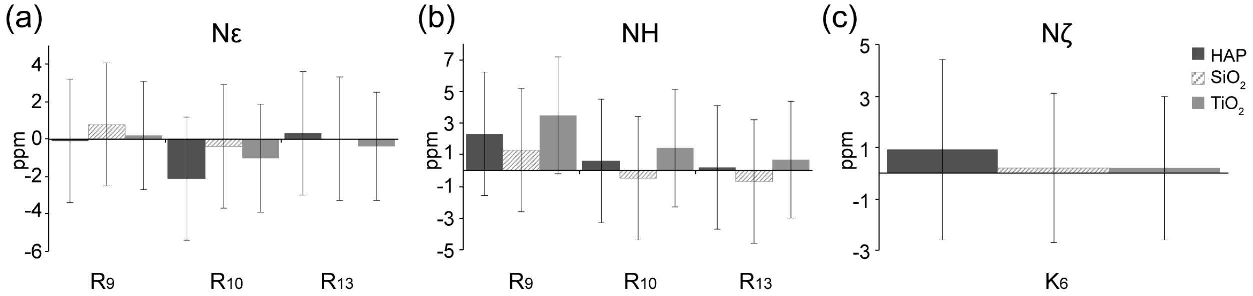

Figure 4.8. Side-chain ΔCS plots showing chemical shift perturbations for (a) ^{15}Nε, (b) ^{15}NH, and (c) ^{15}Nζ. ΔCS for SNa15 on HAP (black), SiO_2 (hatched), and TiO_2 (gray) are in reference to neat SNa15. Positive changes indicate a downfield shift while negative changes indicate an upfield shift relative to the neat peptide.

Bar charts of ^{15}N side-chain ΔCS values are shown in Figure 4.8. Due to the broad nature of peaks in nitrogen spectra, the error bars are quite large. However, the peaks were Gaussian in shape, and a clear chemical shift could be assigned for each ^{15}N spin. Downfield perturbations are observed for R9 ^{15}NH shifts upon adsorption to HAP (2.3 ppm), SiO_2 (1.3 ppm), and TiO_2 (3.5 ppm), indicating interactions with the phosphate buffer and/or the surfaces. The K6 ^{15}Nζ spin also experiences a downfield perturbation, albeit less pronounced, upon adsorption to HAP (0.9 ppm), SiO_2 (0.2 ppm), and TiO_2 (0.2 ppm).

4.5. SNA15 SECONDARY STRUCTURE.

The backbone ^{13}C chemical shifts for neat SNa15, SNa15-HAP, SNa15-SiO_2, and SNa15-TiO_2 were input into TALOS-N.[59] The ϕ/ψ torsion angles predicted by TALOS-N[59] (Appendix C) were used to visualize the secondary structures of SNa15 in each phase using Chimera[64] (Figure 4.9 and Figure 4.10). SNa15 exhibits α-helical structure in each state, although only in the K6-R9 region when adsorbed to SiO_2. For neat SNa15, the ϕ/ψ torsion angles for E4-I11 are clustered around the accepted α-helical values (-57/-47), while the ϕ/ψ torsion angles for R13 and F14 are clustered around the accepted β-sheet values (-80/+150). For the most part, the torsion angles remain similar upon adsorption to HAP; residues E5-I11 exhibit α-helical character, while residues D2, and R13-F14 exhibit β-sheet characteristics. There are large changes in ϕ/ψ at D3-E4, which manifests as a lack of helical character in this region. In TiO_2, the α-helix is extended farther into the N-terminus; the ϕ/ψ angles for D2-I11 are all clustered around -57/-47. The C-terminus remains β-sheet in nature. The structure of SNa15 differs greatly upon adsorption to SiO_2, as reflected in the many differences in ϕ/ψ angles in neat SNa15 and SNa15-SiO_2. The helical region of SNa15 is limited to K6-R9 while the β-sheet region is extended to R10-F14, with the N-terminus in random coil.

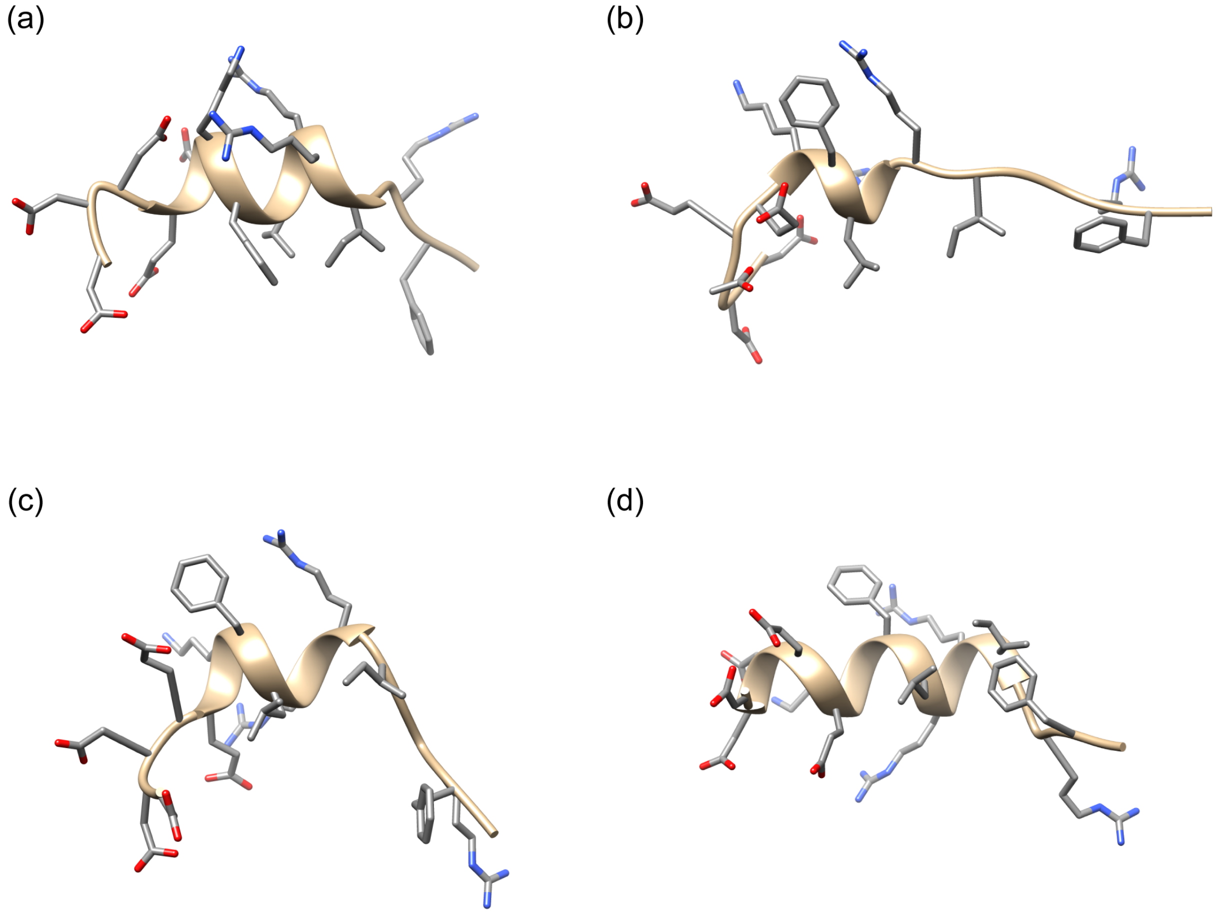

Figure 4.9. Chimera[64]-generated models of (a) SNa15-neat, (b) SNa15-SiO_2, (c) SNa15-HAP, and (d) SNa15-TiO_2 using TALOS-N[59]-predicted torsion angles from experimentally obtained chemical shifts. Each peptide is shown from N-terminus to C-terminus right-to-left.

An end-view of each of the predicted SNa15 structures is shown in Figure 4.10. The end-views clearly show which sections of SNa15 are helical and which are not. It is also easier to compare side-chain orientations in this view. In SNa15-HAP, SNa15-SiO_2, and SNa15-TiO_2, F7 and F14 are pointing in different directions. This is consistent with chemical shift data and relaxation dynamics ($T_1/T_{1\rho}$)[39,126], $^{13}C\{^{31}P\}$ REDOR[126], ^2H ssNMR[39], and NEXAFS[38] data for SN15, which all conclude that F7 is far from the HAP surface (at least 7 Å) while F14 is close to (within 4 Å) and interacting with the surface. It has been posited that in SN15, F14 is in a near-parallel orientation to HAP, thus exposing the delocalized electrons in the phenyl ring.[137] The ΔCS values for the ^{13}C aromatic spins also support this theory for SNa15, as there are perturbations for $^{13}C\gamma$, $^{13}C\delta$, $^{13}C\varepsilon$, and $^{13}C\zeta$ of F14, yet typically much smaller perturbations for the same shifts of F7.

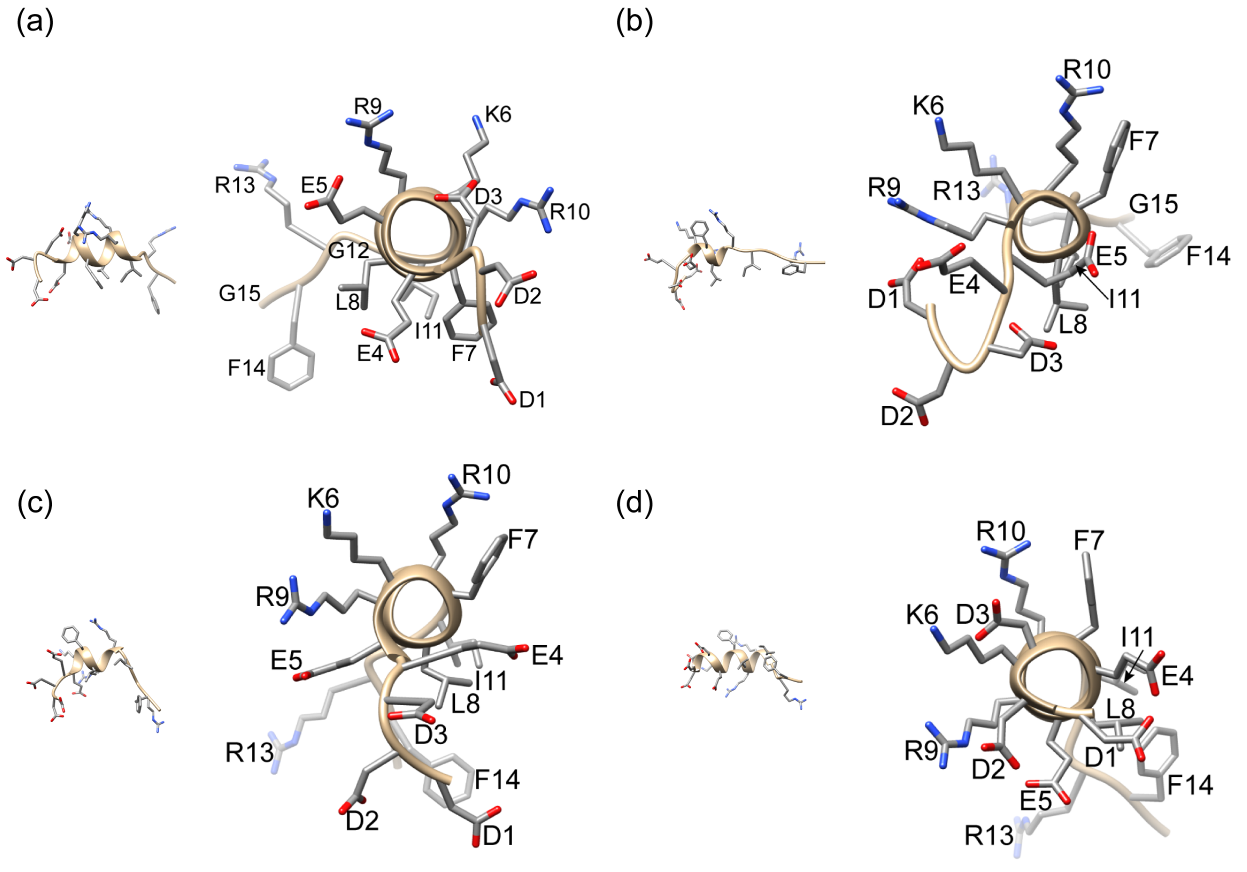

Figure 4.10. End-view of (a) SNa15-neat, (b) SNa15-SiO2, (c) SNa15-HAP, and (d) SNa15-TiO_2 with each residue labeled. Structures are visualized with Chimera[64] using torsion angles predicted by TALOS-N.[59]

The ΔCS values and perturbations in ϕ/ψ angles in the N-terminal region of SNa15 upon adsorption indicate that this region is essential for binding. The carboxyl groups of E4 and E5 experience the largest ΔCS and are likely strongly interacting with the surfaces. Furthermore, E4 and E5 are oriented on the same face of SNa15 (Figure 4.10) as F14 in SNa15-HAP, SNa15-SiO_2, and SNa15-TiO_2.

4.6. DISCUSSION.

Peptide secondary structure is integral to the recognition of biomineral surfaces, and amino acid side-chains play a crucial role in surface binding. Ergo the determination of secondary structures on surfaces, the changes in structure undergone upon adsorption, and the proximity of various amino acids to the surface are all foundational goals in this field. We have used 1D and 2D ssNMR techniques to determine the secondary structure of SNa15 neat and adsorbed to HAP, SiO_2, and TiO_2 surfaces. In addition to comparing these secondary structures, we have used ^{13}C chemical shifts to probe how SNa15 interacts with each surface, specifically which residues have side-chains likely in proximity to and interacting with each surface.

^{13}CO, $^{13}C\alpha$, and $^{13}C\beta$ chemical shift data and resulting TALOS-N[59] –predicted ϕ/ψ angles indicate that SNa15-neat, SNa15-HAP, and SNa15-TiO_2 are mostly α-helical in nature with an unraveling of the helix at each terminus, while SNa15-SiO_2 only has a short α-helical character around K6-R9. ΔCS are calculated for the side-chain ^{13}C spins, which provide important insight into how SNa15 interacts with each surface.

Most notably, ΔCS suggest that E4, E5, and F14 are interacting with each surface. There are large downfield perturbations for the side-chain $^{13}C\gamma$ and $^{13}C\delta$ spins of E4 and E5 (Figure 4.7a-b). In a study of PG adsorbed on HAP and SiO_2, the $^{13}C\delta$ spins experienced downfield shifts of about 2ppm.[83] This CS perturbation is attributed to the decreased shielding of the carboxyl group due to its interaction with the surface. This is consistent with the ΔCS data shown in

Figure 4.7b. For SNa15-HAP, E4 experiences a downfield perturbation of about 3 ppm while E5 is perturbed 4.3 ppm. The ΔCS for SNa15-SiO_2 and SNa15-TiO_2 are also downfield and range from 3.8-5.3 ppm. Furthermore, $^{13}C\{^{31}P\}$ REDOR and $T_{1\rho}$ experiments have determined the distances between the E4 and E5 side-chains of SN15 to the HAP surface and their mobility.[122] The REDOR data determined that E5 was closest to the surface, at a distance of about 4.25 Å, while $T_{1\rho}$ experiments demonstrated a slower relaxation rate for E5 than E4, indicating a restriction in side-chain dynamics and thus a closer proximity to the surface of HAP.[122] For SNa15, it is likely that both E4 and E5 are interacting with the mineral surfaces, as both experience large downfield ΔCS upon adsorption with HAP, SiO_2, and TiO_2. The perturbations are roughly the same magnitude within error for both residues, suggesting a similar amount of contact. This differs from the studies with SN15 and statherin, where only E5 was proposed to interact with HAP.

It is also likely that F14 is interacting with the mineral surfaces based on the large side-chain ΔCS. The role of phenylalanine residues in the binding of statherin to HAP has been studied extensively.[38,39,126] Gibson and coworkers[126] studied the role of F7 and F14 in SN15 adsorption to HAP through isotropic chemical shift perturbations, $^{13}C\{^{31}P\}$ REDOR, and $T_{1\rho}$ relaxation measurements. They found that F14 is closer to the surface and is more dynamically constrained than F7, which is oriented away from the HAP surface. A study by Weidner and coworkers[38] used NEXAFS and SFG to determine that the phenyl ring of F14 points toward the HAP surface, while the phenyl ring of F7 points away. This is consistent with our data for HAP, where there are large ΔCS for F14 and minimal ΔCS for F7 (Figure 4.6, Figure 4.7).

The side-chain ΔCS for the basic residues also provide information as to how SNa15 is binding. There are negligible perturbations for most of the side-chain ^{13}C spins for K6, R9, and

R10. However, the R13 $^{13}C\gamma$ and $^{13}C\delta$ spins experience significant perturbations in the range of -0.9 to -2 ppm. This suggests that R13 interacts with the surfaces while the remaining basic residues do not. This is supported by the structures shown in Figure 4.9 and Figure 4.10. The R13 side-chain is oriented on the same face of SNa15 as D2, E4, E5, and F14, all residues that are hypothesized to interact with the surfaces. This is true for SNa15 adsorbed to HAP, SiO_2, and TiO_2.

Furthermore, for SNa15-HAP, D2 and D3 are oriented along the hypothesized binding face of SNa15. These residues experience a $^{13}C\gamma$ downfield shift of 1.2 and 1.3 ppm, respectively, upon adsorption. This is also true for SNa15-SiO_2, and D2 and D3 both experience a $^{13}C\gamma$ downfield shift of 2 ppm. However, only D2 is oriented along the binding face for SNa15-TiO_2, and only D2 experiences a significant ΔCS for the $^{13}C\gamma$ spin. Based on these perturbations, it is likely that the aspartic acid residues are interacting with the surfaces. Specifically, D2 is involved in the binding of SNa15 to HAP, SiO_2, and TiO_2, while D3 is involved in the binding of SNa15 to HAP and SiO_2.

Based on the secondary structures and side-chain ΔCS information, we hypothesize that the binding domain of SNa15 consists of the D2, D3, E4, E5, R13, and F14 residues for binding to HAP and SiO_2 and consists of the D2, E4, E5, R13, and F14 residues for binding to TiO_2. The residues composing the hypothesized binding domain are all oriented on the same face of SNa15 and all experience significant side-chain chemical shift perturbations upon adsorption. The lack of α-helical character in the N-terminus allows consecutive acidic residues to all be positioned along the same face, thus allowing for maximum interactions of these residues with each surface.

4.7. CONCLUSION.

This is the first ssNMR study of the structure and binding of SNa15 as a function of mineral surface. This study has produced site-specific chemical shift assignments for most of the backbone ^{13}C spins in neat SNa15 and SNa15 adsorbed to HAP, SiO_2, and TiO_2, enabling a comparison of secondary structures between the four systems. Based on the torsion angles predicted by TALOS-N[59], SNa15 adopts a mostly α-helical structure, with deviations around the termini, in its neat form and when adsorbed to HAP and TiO_2. However, upon adsorption to SiO_2, SNa15 unravels and only retains its α-helical nature in a small central region (K6-R9).

Site-specific chemical shift assignments were also obtained for most of the side-chain ^{13}C spins and all of the side-chain ^{15}N spins. The ΔCS with respect to neat SNa15 provides information about the side-chain interactions. Residues with large perturbations, for example the side-chain carboxyl groups of the aspartic and glutamic acid residues, are interpreted as interacting with the surface. This interpretation is based on chemical shift and heteronuclear correlation experiments previously conducted on PD, PG, and SN15 adsorbed to HAP and/or SiO_2. A hypothesized binding domain of SNa15 is proposed, and despite the differences in secondary structure upon adsorption to the different mineral surfaces, remains relatively consistent throughout each system.

Chapter 5. CONCLUSION.

The study of biomineralization proteins has relevance to many fields, ranging from the development of new materials to catalysis to medical implant devices. There has recently been a push to both identify biomineralization proteins and discover their mechanism(s) of action. The proteins involved in these processes interact with mineral surfaces to mediate hard tissue growth, yet these interactions are not yet well understood. Studying the molecular-level interactions between proteins and inorganic minerals is a crucial step towards understanding how these proteins recognize the biomineral surface and ultimately control its growth. ssNMR is well suited for the study of biomineralization proteins, as it can probe their structure when neat and when complexed with an inorganic mineral. This thesis utilizes various ssNMR experiments to probe the secondary structures of R5, S-K peptides, and SNa15 in their neat forms and when interacting with mineral phases such as HAP, SiO_2, and TiO_2. The work presented here approaches peptide-mineral interactions from two facets: biomineralization (i.e. R5 and S-K peptides) and surface adsorption (i.e. SNa15).

Chapter 2 presented the comparative study of R5's role in biosilica and titania formation. The structures of the resultant mineral materials were compared, as were the structures of R5 upon co-precipitation. ^{13}C backbone chemical shifts were used to determine ϕ/ψ torsion angles, which provide information on peptide secondary structure. The secondary structures for neat R5, R5-SiO_2, and R5-TiO_2 were determined and compared. ΔCS was used to quantitatively assess the perturbations in secondary structure upon co-precipitation with each mineral. Furthermore, ^{13}C side-chain chemical shifts and ΔCS were used to assess the proximity of various amino acid side-chains to the SiO_2 and TiO_2 surfaces, providing information on which residues are interacting closely with the mineral, and are thus likely to be essential in mineral recognition, nucleation, and growth.

Chapter 3 presented the design and activity of a series of S-K peptides. The two peptides with the highest and lowest TiO_2-precipitating activities, $SKSK_3SKS$ and KSSKK, respectively, were studied on a molecular level via ssNMR. Akin to the R5 project, ^{13}C backbone chemical shifts and ΔCS were used to probe the secondary structures of the peptides neat and co-precipitated with TiO_2. Additionally, ^{13}C side-chain chemical shifts and ΔCS were used to determine which residues were likely interacting with the TiO_2 surface. Since Ti is not a practical NMR nucleus, DFT calculations were conducted to support the analysis of lysine side-chain ΔCS.

Finally, Chapter 4 presented the study of SNa15 adsorbed to three mineral surfaces: HAP, SiO_2, and TiO_2. Adsorption isotherms were conducted to determine the disassociation constants and the maximum coverage on each surface. Then, both ^{13}C and ^{15}N NMR experiments were conducted to probe the secondary structure of SNa15 on each surface as well as the side-chain interactions with the surfaces. Probing the structure of SNa15 as a function of surface provides key information on the binding domain of SNa15 and how it changes or is altered between surfaces.

In summary, this thesis uses 1D $^{13}C/^{15}N$ and 2D ^{13}C NMR experiments to study: (1) the secondary structures of peptides when in contact with minerals, either in a co-precipitate or when adsorbed to a surface and (2) amino-acid side-chain proximities and interactions with buffer, other peptide monomers, or mineral phases. This data is crucial to furthering the atomic-level understanding of biomineral recognition, nucleation, and growth.

BIBLIOGRAPHY

(1) Fujishima, A.; Honda, K. Electrochemical Photolysis of Water at a Semiconductor Electrode. *Nature* **1972**, *238*, 37–38.

(2) Hoffmann, M. R.; Martin, S. T.; Choi, W.; Bahnemannt, D. W.; Keck, W. M. Environmental Applications of Semiconductor Photocatalysis. *Chem. Rev* **1995**, *95*, 69–96.

(3) Linsebigler, A. L.; Lu, G.; Yates, J. T. J. Photocatalysis on TiO2 Surfaces: Principles, Mechanisms, and Selected Results. *Chem. Rev.* **1995**, *95*, 735–758.

(4) Abo-Farha, S. A. Photocatalytic Degradation of Monoazo and Diazo Dyes in Wastewater on Nanometer-Sized TiO 2. *J. Am. Sci.* **2010**, *6* (611), 130–142.

(5) Li, G.; Gray, K. A. The Solid–solid Interface: Explaining the High and Unique Photocatalytic Reactivity of TiO 2 -Based Nanocomposite Materials. *Chem. Phys.* **2007**, *339*, 173–187.

(6) Adachi, M.; Murata, Y.; Wang, F.; Jiu, J. Synthesis of Titania Nanocrystals: Application for Dye-Sensitized Solar Cells. In *Self-Organized Nanoscale Materials*; Springer New York: New York, NY, 2006; pp 71–100.

(7) Acevedo, A.; Carpio, E. A.; Rodríguez, J.; Manzano, M. A. Disinfection of Natural Water by Solar Photocatalysis Using Immobilized TiO2 Devices: Efficiency in Eliminating Indicator Bacteria and Operating Life of the System. *J. Sol. Energy Eng.* **2012**, *134* (1), 11008.

(8) Varghese, O. K.; Grimes, C. A. Metal Oxide Nanoarchitectures for Environmental Sensing. *J. Nanosci. Nanotechnol.* **2003**, *3*, 277–293.

(9) Wintermantel, E.; Eckert, K.-L.; Huang, N.-P.; Textor, M.; Brunette, D. M. Titanium Ceramics for Cell-Carriers and for Medical Applications; Springer Berlin Heidelberg, 2001; pp 649–671.

(10) Chen, X.; Mao, S. S. Titanium Dioxide Nanomaterials: Synthesis, Properties, Modifications, and Applications. *Chem. Rev* **2007**, *107*, 2891–2959.

(11) Qian, Y.; Chen, Q.; Chen, Z.; Fanb, C.; Zhou, G. Preparation of Ultrafine Powders of TiO, by Hydrothermal H202 Oxidation Starting from Metallic Ti. *J. MATER. CHEM* **1993**, *3* (2), 203–205.

(12) Chhabra, V.; Pillai, V.; Mishra, B. K.; Morrone, A.; Shah, D. 0. Synthesis, Characterization, and Properties of Microemulsion-Mediated Nanophase Ti02 Particles. *Langmuir* **1995**, *11*, 3307–3311.

(13) Cheng, H.; Ma, J.; Zhao, Z.; Qi, L. Hydrothermal Preparation of Uniform Nanosize Rutile and Anatase Particles. *Chem. Mater* **1995**, *7*, 663–671.

(14) Jang, H. D.; Kim, S.-K. Controlled Synthesis of Titanium Dioxide Nanoparticles in a Modified Diffusion Flame Reactor. *Mater. Res. Bull.* **2001**, *36*, 627–637.

(15) Wang, C.-C.; Ying, J. Y. Sol-Gel Synthesis and Hydrothermal Processing of Anatase and Rutile Titania Nanocrystals. *Chem. Mater* **1999**, *11*, 3113–3120.

(16) Mann, S.; Archibald, D. D.; Didymus, J. M.; Douglas, T.; Heywood, B. R.; Meldrum, F. C.; Reeves, N. J. Crystallization at Inorganic-Organic Interfaces: Biominerals and Biomimetic Synthesis. *Science* **1993**, *261* (September), 1286–1292.

(17) Roehrich, A.; Drobny, G. P. Solid-State NMR Studies of Biomineralization Peptides and Proteins. *Acc. Chem. Res.* **2013**, *46* (9), 2136–2144.

(18) Belton, D. J.; Patwardhan, S. V; Perry, C. C. Spermine, Spermidine and Their Analogues

Generate Tailored Silicas. *J. MATER. CHEM* **2005**, *15*, 4629–4638.

(19) Kröger, N.; Deutzmann, R.; Sumper, M. Polycationic Peptides from Diatom Biosilica That Direct Silica Nanosphere Formation. *Science (80-.).* **1999**, *286* (5442), 1129–1132.

(20) Kröger, N.; Deutzmann, R.; Bergsdorf, C.; Sumper, M. Species-Specific Polyamines from Diatoms Control Silica Morphology. *PNAS* **2000**, *97* (26), 14133–14138.

(21) Knecht, M. R.; Wright, D. W. Functional Analysis of the Biomimetic Silica Precipitating Activity of the R5 Peptide from Cylindrotheca fusiformisElectronic Supplementary Information (ESI) Available: HPLC and MALDI of Peptides (11 Pgs); EMs of Silica Particles (4 Pgs); IR Data (3 Pgs); *Chem. Commun.* **2003**, No. 24, 3038.

(22) Lopez, P.; Gautier, C.; Livage, J.; Coradin, T. Mimicking Biogenic Silica Nanostructures Formation. *Curr. Nanosci.* **2005**, *1* (1), 73–83.

(23) Buckle, E. L.; Roehrich, A.; Vandermoon, B.; Drobny, G. P. Comparative Study of Secondary Structure and Interactions of the R5 Peptide in Silicon Oxide and Titanium Oxide Coprecipitates Using Solid-State NMR Spectroscopy. *Langmuir* **2017**, *33* (40), 10517–10524.

(24) Otzen, D. The Role of Proteins in Biosilicification. *Scientifica (Cairo).* **2012**, *2012*.

(25) Dujardin, E.; Mann, S. Bio-Inspired Materials Chemistry. *Adv. Mater.* **2002**, *14* (11), 775–788.

(26) Mann, S.; Ozin, G. A. Synthesis of Inorganic Materials with Complex Form. *Nature* **1996**, *382* (25), 313–318.

(27) Naik, R. R.; Whitlock, P. W.; Rodriguez, F.; Brott, L. L.; Glawe, D. D.; Clarson, S. J.; Stone, M. O. Controlled Formation of Biosilica Structures in Vitro. *Chem. Commun.* **2003**, 238–239.

(28) Kröger, N.; Poulsen, N. Diatoms-from Cell Wall Biogenesis to Nanotechnology. *Annu. Rev. Genet.* **2008**, *42*, 83–107.

(29) Kroger, N. Self-Assembly of Highly Phosphorylated Silaffins and Their Function in Biosilica Morphogenesis. *Science (80-.).* **2002**, *298* (5593), 584–586.

(30) Kröger, N.; Deutzmann, R.; Sumper, M. Silica-Precipitating Peptides from Diatoms THE CHEMICAL STRUCTURE OF SILAFFIN-1A FROM CYLINDROTHECA FUSIFORMIS*. *J. Biol. Chem.* **2001**, *276* (28), 26066–26070.

(31) Kröger, N.; Sandhage, K. H. From Diatom Biomolecules to Bioinspired Syntheses of Silica-and Titania-Based Materials Silica Formation In Vitro Using Biomolecules from Diatoms. *MRS Bull.* **2010**, *35*, 122–126.

(32) Zane, A. C.; Michelet, C.; Roehrich, A.; Emani, P. S.; Drobny, G. P. Silica Morphogenesis by Lysine-Leucine Peptides with Hydrophobic Periodicity. *Langmuir* **2014**, *30* (24), 7152–7161.

(33) Raj, P. A.; Johnsson, M.; Levine, M. J.; NancollaslllI, G. H. Salivary Statherin DEPENDENCE ON SEQUENCE, CHARGE, HYDROGEN BONDING POTENCY, AND HELICAL CONFORMATION FOR ADSORPTION TO HYDROXYAPATITE AND INHIBITION OF MINERALIZATION*. *J. Biol. Chem.* **1992**, *267* (9), 5968–5976.

(34) Goobes, R.; Goobes, G.; Shaw, W. J.; Drobny, G. P.; Campbell, C. T.; Stayton, P. S. Thermodynamic Roles of Basic Amino Acids in Statherin Recognition of Hydroxyapatite. *Biochemistry* **2007**, *46*, 4725–4733.

(35) Goobes, G.; Goobes, R.; Schueler-Furman, O.; Baker, D.; Stayton, P. S.; Drobny, G. P. Folding of the C-Terminal Bacterial Binding Domain in Statherin upon Adsorption onto Hydroxyapatite Crystals. *PNAS* **2006**, *103* (44), 16083–16088.

(36) Long, J. R.; Shaw, W. J.; Stayton, P. S.; Drobny, G. P. Structure and Dynamics of Hydrated Statherin on Hydroxyapatite As Determined by Solid-State NMR. *Biochemistry* **2001**, *40* (51), 15451–15455.

(37) Goobes, G.; Stayton, P. S.; Drobny, G. P. Solid State NMR Studies of Molecular Recognition at Protein–mineral Interfaces. *Prog. Nucl. Magn. Reson. Spectrosc.* **2007**, *50* (2–3), 71–85.

(38) Weidner, T.; Dubey, M.; Breen, N. F.; Ash, J.; Baio, J. E.; Jaye, C.; Fischer, D. A.; Drobny, G. P.; Castner, D. G. Direct Observation of Phenylalanine Orientations in Statherin Bound to Hydroxyapatite Surfaces. *J. Am. Chem. Soc.* **2012**, *134*, 8750–8753.

(39) Li, K.; Emani, P. S.; Ash, J.; Groves, M.; Drobny, G. P. A Study of Phenylalanine Side-Chain Dynamics in Surface-Adsorbed Peptides Using Solid-State Deuterium NMR and Rotamer Library Statistics. *J. Am. Chem. Soc.* **2014**, *136*, 11402–11411.

(40) Masica, D. L.; Ash, J. T.; Ndao, M.; Drobny, G. P.; Gray, J. J. Toward a Structure Determination Method for Biomineral-Associated Protein Using Combined Solid- State NMR and Computational Structure Prediction. *Structure* **2010**, *18*, 1678–1687.

(41) Shaw, W. J.; Ferris, K.; Tarasevich, B.; Larson, J. L. The Structure and Orientation of the C-Terminus of LRAP. *Biophys. J.* **2008**, *94*, 3247–3257.

(42) Shaw, W. J. Solid-State NMR Studies of Proteins Immobilized on Inorganic Surfaces. *Solid State Nucl. Magn. Reson.* **2015**, *70*, 1–14.

(43) Geiger, Y.; Gottlieb, H. E.; Akbey, Ü.; Oschkinat, H.; Goobes, G. Studying the Conformation of a Silaffin-Derived Pentalysine Peptide Embedded in Bioinspired Silica Using Solution and Dynamic Nuclear Polarization Magic-Angle Spinning NMR. *J. Am. Chem. Soc.* **2016**, *138* (17), 5561–5567.

(44) Mirau, P. A.; Naik, R. R.; Gehring, P. Structure of Peptides on Metal Oxide Surfaces Probes by NMR. *J. Am. Chem. Soc.* **2011**, *133*, 18243–18248.

(45) Keeler, J. *Understanding NMR Spectroscopy*; John Wiley and Sons Ltd.: Chichester, England, 2005.

(46) Duer, M. J. *Solid-State NMR Spectroscopy: Principles and Applications*; Blackwell Science Ltd: Oxford, 2002.

(47) Andrew, E. R. Magic Angle Spinning in Solid State N.m.r. Spectroscopy. *Philos. Trans. R. Soc. London. Ser. A, Math. Phys. Sci.* **1981**, *299* (1452), 505–520.

(48) Takegoshi, K.; Nakamura, S.; Terao, T. 13C-1H Dipolar-Assisted Rotational Resonance in Magic-Angle Spinning NMR. *Chem. Phys. Lett.* **2001**, *344* (5–6), 631–637.

(49) Takegoshi, K.; Nakamura, S.; Terao, T. 13C–1H Dipolar-Driven 13C–13C Recoupling without 13C Rf Irradiation in Nuclear Magnetic Resonance of Rotating Solids. *J. Chem. Phys.* **2003**, *118* (5), 2325–2341.

(50) Takegoshi, K.; Nakamura, S.; Terao, T. Dipolar-Driven Recoupling without Rf Irradiation in Nuclear Magnetic Resonance of Rotating Solids Chemical Shift Correlation Spectroscopy in Rotating Solids: Radio Frequency-Driven Dipolar Recoupling and Longitudinal Exchange H Dipolar-Driven C Rf Irradiation in Nuclear Magnetic Resonance of Rotating Solids. *J. Chem. Phys. J. Chem. Phys. J. Chem. Phys. J. Chem. Phys. J. Chem. Phys. J. Chem. Phys. J. Chem. Phys.* **2003**, *1181* (10), 2325–245101.

(51) Crocker, E.; Patel, A. B.; Eilers, M.; Jayaraman, S.; Getmanova, E.; Reeves, P. J.; Ziliox, M.; Khorana, H. G.; Sheves, M.; Smith, S. O. Dipolar Assisted Rotational Resonance NMR of Tryptophan and Tyrosine in Rhodopsin. *J. Biomol. NMR* **2004**, *29* (1), 11–20.

(52) Hovmöller, S.; Zhou, T.; Ohlson, T. Conformations of Amino Acids in Proteins. *Acta*

Crystallogr. D. Biol. Crystallogr. **2002**, *58* (Pt 5), 768–776.

(53) de Dios, A. C.; Pearson, J. G.; Oldfield, E. Secondary and Tertiary Structural Effects on Protein NMR Chemical Shifts: An Ab Initio Approach. *Science* **1993**, *260* (5113), 1491–1496.

(54) Wishart, D.; Sykes, B. The 13C Chemical-Shift Index: A Simple Method for the Identification of Protein Secondary Structure Using 13C Chemical-Shift Data. *J. Biomol. NMR* **1994**, *4* (2).

(55) Wishart, D. S. Interpreting Protein Chemical Shift Data. *Prog. Nucl. Magn. Reson. Spectrosc.* **2011**, *58* (1–2), 62–87.

(56) Saitô, H. Conformation-dependent13C Chemical Shifts: A New Means of Conformational Characterization as Obtained by High-Resolution Solid-state13C NMR. *Magn. Reson. Chem.* **1986**, *24* (10), 835–852.

(57) Spera, S.; Bax, A. Empirical Correlation between Protein Backbone Conformation and C.alpha. and C.beta. 13C Nuclear Magnetic Resonance Chemical Shifts. *J. Am. Chem. Soc.* **1991**, *113* (14), 5490–5492.

(58) Robustelli, P.; Stafford, K. A.; Palmer, A. G.; III. Interpreting Protein Structural Dynamics from NMR Chemical Shifts. *J. Am. Chem. Soc.* **2012**, *134* (14), 6365–6374.

(59) Shen, Y.; Bax, A. Protein Backbone and Sidechain Torsion Angles Predicted from NMR Chemical Shifts Using Artificial Neural Networks. *J. Biomol NMR* **2013**, *56* (3), 227–241.

(60) Ulrich, E. L.; Akutsu, H.; Doreleijers, J. F.; Harano, Y.; Ioannidis, Y. E.; Lin, J.; Livny, M.; Mading, S.; Maziuk, D.; Miller, Z.; et al. BioMagResBank. *Nucleic Acids Res.* **2008**, *36* (SUPPL. 1), D402–D408.

(61) Berman, H. M.; Westbrook, J.; Feng, Z.; Gilliland, G.; Bhat, T. N.; Weissig, H.; Shindyalov, I. N.; Bourne, P. . The Protein Data Bank. *Nucleic Acids Res.* **2000**, *28*, 253–242.

(62) Ramakrishnan, C.; Ramachandran, G. N. STEREOCHEMICAL CRITERIA FOR POLYPEPTIDE AND PROTEIN CHAIN CONFORMATIONS II. ALLOWED CONFORMATIONS FOR A PAIR OF PEPTIDE UNITS. *Biophys. J.* **1965**, *5* (6), 909–933.

(63) Ramachandran, G.; Ramakrishnan, C.; Sasisekharan, V. Stereochemistry of Polypeptide Chain Configurations. *J. Mol. Biol.* **1963**, *7*, 95–99.

(64) Pettersen, E. F.; Goddard, T. D.; Huang, C. C.; Couch, G. S.; Greenblatt, D. M.; Meng, E. C.; Ferrin, T. E. UCSF Chimera - A Visualization System for Exploratory Research and Analysis. *J. Comput. Chem.* **2004**, *25* (13), 1605–1612.

(65) Lovell, S. C.; Davis, I. W.; Arendall, W. B.; de Bakker, P. I. W.; Word, J. M.; Prisant, M. G.; Richardson, J. S.; Richardson, D. C. Structure Validation by Cα Geometry: Φ,ψ and Cβ Deviation. *Proteins Struct. Funct. Bioinforma.* **2003**, *50* (3), 437–450.

(66) Senior, L.; Crump, M. P.; Williams, C.; Booth, P. J.; Mann, S.; Perriman, A. W.; Curnow, P. Structure and Function of the Silicifying Peptide R5. *J. Mater. Chem. B* **2015**, *3* (13), 2607–2614.

(67) Lechner, C. C.; Becker, C. F. W. A Sequence-Function Analysis of the Silica Precipitating Silaffin R5 Peptide. *J. Pept. Sci.* **2014**, *20* (2), 152–158.

(68) Belton, D.; Paine, G.; Patwardhan, S. V; Perry, C. C. Towards an Understanding of (Bio)silicification: The Role of Amino Acids and Lysine Oligomers in Silicification. *J. MATER. CHEM* **2004**, *14*, 2231–2241.

(69) Rodríguez, F.; Glawe, D. D.; Naik, R. R.; Hallinan, K. P.; Stone, M. O. Study of the

Chemical and Physical Influences upon in Vitro Peptide-Mediated Silica Formation. *Biomacromolecules* **2004**, *5*, 261–265.

(70) Sumper, M.; Lorenz, S.; Brunner, E. Biomimetic Control of Size in the Polyamine-Directed Formation of Silica Nanospheres. *Angew. Chemie Int. Ed.* **2003**, *42* (42), 5192–5195.

(71) Deming, T. J.; Cha, J. N.; Stucky, G. D.; Morse, D. E. Biomimetic Synthesis of Ordered Silica Structures Mediated by Block Copolypeptides. *Nature* **2000**, *403* (6767), 289–292.

(72) Sano, K.-I.; Sasaki, H.; Shiba, K. Specificity and Biomineralization Activities of Ti-Binding Peptide-1 (TBP-1). *Langmuir* **2005**, *21*, 3090–3095.

(73) Cole, K. E.; Valentine, A. M. Spermidine and Spermine Catalyze the Formation of Nanostructured Titanium Oxide. *Biomacromolecules* **2007**, *8*, 1641–1647.

(74) Durupthy, O.; Bill, J.; Aldinger, F. Bioinspired Synthesis of Crystalline TiO 2 : Effect of Amino Acids on Nanoparticles Structure and Shape. *Cryst. Growth Des.* **2007**, *7* (12), 2696–2704.

(75) Dickerson, M. B.; Jones, S. E.; Cai, Y.; Ahmad, G.; Naik, R. R.; Kröger, N.; Sandhage, K. H. Identification and Design of Peptides for the Rapid, High-Yield Formation of Nanoparticulate TiO 2 from Aqueous Solutions at Room Temperature. *Chem. Mater* **2008**, *20*, 1578–1584.

(76) Kharlampieva, E.; Min Jung, C.; Kozlovskaya, V.; Tsukruk, V. V. Secondary Structure of Silaffin at Interfaces and Titania Formation. *J. MATER. CHEM* **2010**, *20*, 5242–5250.

(77) Hernández-Gordillo, A.; Hernández-Arana, A.; Campero, A.; Vera-Robles, L. I. Biomimetic Sol–Gel Synthesis of TiO 2 and SiO 2 Nanostructures. *Langmuir* **2014**, *30* (14), 4084–4093.

(78) Puddu, V.; Slocik, J. M.; Naik, R. R.; Perry, C. C. Titania Binding Peptides as Templates in the Biomimetic Synthesis of Stable Titania Nanosols: Insight into the Role of Bu Ff Ers in Peptide- Mediated Mineralization. *Langmuir* **2013**, *29* (30), 9464–9472.

(79) Sewell, S. L.; Wright, D. W. Biomimetic Synthesis of Titanium Dioxide Utilizing the R5 Peptide Derived from Cylindrotheca F Usiformis. *Chem. Mater.* **2006**, *18* (13), 3108–3113.

(80) Morcombe, C. R.; Zilm, K. W. Chemical Shift Referencing in MAS Solid State NMR. *J. Magn. Reson.* **2003**, *162* (2), 479–486.

(81) Rueden, C.; Dietz, C.; Horn, M.; Schindelin, J.; Northan, B.; Berthold, M.; Eliceiri, K. ImageJ Ops. 2016.

(82) Patwardhan, S. V; Emami, F. S.; Berry, R. J.; Jones, S. E.; Naik, R. R.; Deschaume, O.; Heinz, H.; Perry, C. C. Chemistry of Aqueous Silica Nanoparticle Surfaces and the Mechanism of Selective Peptide Adsorption. *J. Am. Chem. Soc.* **2012**, *134*, 6244–6256.

(83) Fernandez, V. L.; Reimer, J. A.; Denn, M. M. Magnetic Resonance Studies of Polypeptides Adsorbed on Silica and Hydroxyapatite Surfaces. *J. Am. Chem. SOC* **1992**, *114*, 9634–9642.

(84) Shir, I. Ben; Kababya, S.; Amitay-Rosen, T.; Balazs, Y. S.; Schmidt, A. Molecular Level Characterization of the Inorganic-Bioorganic Interface by Solid State NMR: Alanine on a Silica Surface, a Case Study. *J. Phys. Chem. B* **2010**, *114* (18), 5989–5996.

(85) Wisser, D.; Bruckner, S. I.; Wisser, F. M.; Althoff-Ospelt, G.; Getzschmann, J.; Kaskel, S.; Brunner, E. 1H-13C-29Si Triple Resonance and REDOR Solid-State NMR- A Tool to Study Interactions between Biosilica and Organic Molecules in Diatom Cell Walls. *Solid State Nucl. Magn. Reson.* **2015**, *66–67*, 33–39.

(86) Schug, K. A.; Lindner, W. Noncovalent Binding between Guanidinium and Anionic Groups:? Focus on Biological- and Synthetic-Based Arginine/Guanidinium Interactions with Phosph[on]ate and Sulf[on]ate Residues. *Chem. Rev.* **2005**, *105* (1), 67–114.

(87) Su, Y.; Doherty, T.; Waring, A. J.; Ruchala, P.; Hong, M. Roles of Arginine and Lysine Residues in the Translocation of a Cell-Penetrating Peptide from13C, 31P, and19F Solid-State NMR. *Biochemistry* **2009**, *48* (21), 4587–4595.

(88) Sano, K.-I.; Shiba, K. A Hexapeptide Motif That Electrostatically Binds to the Surface of Titanium. *J. Am. Chem. SOC* **2003**, *125*, 14234–14235.

(89) Hayashi, T.; Sano, K.-I.; Shiba, K.; Iwahori, K.; Yamashita, I.; Hara, M. Critical Amino Acid Residues for the Specific Binding of the Ti-Recognizing Recombinant Ferritin with Oxide Surfaces of Titanium and Silicon. *Langmuir* **2009**, *25* (18), 10901–10906.

(90) Roddick-Lanzilotta, A. D.; Connor, P. A.; Mcquillan, A. J. An In Situ Infrared Spectroscopic Study of the Adsorption of Lysine to TiO 2 from an Aqueous Solution.

(91) Roddick-Lanzilotta, A.; McQuillan, A. An in Situ Infrared Spectroscopic Study of Glutamic Acid and of Aspartic Acid Adsorbed on TiO(2): Implications for the Biocompatibility of Titanium. *J. Colloid Interface Sci.* **2000**, *227* (1), 48–54.

(92) Lechner, C. C.; Becker, C. F. W. Modified Silaffin R5 Peptides Enable Encapsulation and Release of Cargo Molecules from Biomimetic Silica Particles. *Bioorganic Med. Chem.* **2013**, *21* (12), 3533–3541.

(93) Poulsen, N.; Scheffel, A.; Sheppard, V. C.; Chesley, P. M.; Kroğer, N. Pentalysine Clusters Mediate Silica Targeting of Silaffins in Thalassiosira Pseudonana. *J. Biol. Chem.* **2013**, *288* (28), 20100–20109.

(94) Li, N.; Zhang, X.; Wang, Q.; Wang, F.; Shen, P. Biomimetic Synthesis of Silica Hollow Spheres Using Poly (L-Lysine) and Mechanism Research{. *RSC Adv.* **2012**, *2*, 3288–3297.

(95) Bommel, K. J. C. van; Jung, J. H.; Shinkai, S. Poly(L-Lysine) Aggregates as Templates for the Formation of Hollow Silica Spheres. *Adv. Mater.* **2001**, *13* (19), 1472–1476.

(96) Mizutani, T.; Nagase, H.; Ogoshi, H. Silicic Acid Polymerization Catalyzed by Amines and Polyamines. *Chem. Lett.* **1998**, 133–134.

(97) Sumper, M.; Lorenz, S.; Brunner, E. Biomimetic Control of Size in the Polyamine-Directed Formation of Silica Nanospheres. *Angew. Chemie Int. Ed.* **2003**, *42* (42), 5192–5195.

(98) Kang, S. J.; Won, H. S.; Choi, W. S.; Lee, B. J. De Novo Generation of Antimicrobial LK Peptides with a Single Tryptophan at the Critical Amphipathic Interface. *J. Pept. Sci.* **2009**, *15* (9), 583–588.

(99) DeGrado, W.; Lear, J. Induction of Peptide Conformation at Apolar Water Interfaces. 1. A Study with Model Peptides of Defined Hydrophobic Periodicity. *J. Am. Chem. Soc.* **1985**, *107* (10), 7684–7689.

(100) Fang, Y.; Wu, Q.; Dickerson, M. B.; Cai, Y.; Shian, S.; Berrigan, J. D.; Poulsen, N.; Kröger, N.; Sandhage, K. H. Protein-Mediated Layer-by-Layer Syntheses of Freestanding Microscale Titania Structures with Biologically Assembled 3-D Morphologies. *Chem. Mater.* **2009**, *21* (24), 5704–5710.

(101) Sultan, A. M.; Hughes, Z. E.; Walsh, R. Binding Affinities of Amino Acid Analogues at the Charged Aqueous Titania Interface: Implications for Titania-Binding Peptides. *Langmuir* **2014**.

(102) Dickerson, M. B.; Sandhage, K. H.; Naik, R. R. Protein- and Peptide-Directed Syntheses of Inorganic Materials. *Chem. Rev.* **2008**, *108* (11), 4935–4978.

(103) Stote, R. E.; Filocamo, S. F.; Lum, J. S. Silaffin Primary Structure and Its Effects on the Precipitation Morphology of Titanium Dioxide. *J. Mater. Res.* **2016**, *31* (10), 1373–1382.

(104) Yoe, J. H.; Armstrong, A. R. Colorimetric Determination of Titanium with Disodium-1,2-Dihydroxybenzene-3,5-Disulfonate. *Anal. Chem.* **1947**, *19* (2), 100–102.

(105) Becke, A. D. Density‐functional Thermochemistry. III. The Role of Exact Exchange. *J. Chem. Phys.* **1993**, *98* (7), 5648–5652.

(106) Lee; Yang; Parr. Development of the Colle-Salvetti Correlation-Energy Formula into a Functional of the Electron Density. *Phys. Rev. B. Condens. Matter* **1988**, *37* (2), 785–789.

(107) Barone, V.; Cossi*, M. Quantum Calculation of Molecular Energies and Energy Gradients in Solution by a Conductor Solvent Model. *J. Phys. Chem. A* **1998**, *102* (11), 1995–2001.

(108) Cossi, M.; Rega, N.; Scalmani, G.; Barone, V. Energies, Structures, and Electronic Properties of Molecules in Solution with the C-PCM Solvation Model. *J. Comput. Chem.* **2003**, *24* (6), 669–681.

(109) M. J. Frisch, G. W. Trucks, H. B. Schlegel, G. E. Scuseria, M. A. Robb, J. R. Cheeseman, G. Scalmani, V. Barone, G. A. Petersson, H. Nakatsuji, X. Li, M. Caricato, A. V. Marenich, J. Bloino, B. G. Janesko, R. Gomperts, B. Mennucci, H. P. Hratchian, J. V., and D. J. F. Gaussian 16, Revision A.03. Gaussian, Inc: Wallingford, CT 2016.

(110) Guo, C.; Holland, G. P. Investigating Lysine Adsorption on Fumed Silica Nanoparticles. *J. Phys. Chem. C* **2014**, *118*, 25792–25801.

(111) Suzuki, Y.; Shindo, H.; Asakura, T. Structure and Dynamic Properties of a Ti-Binding Peptide Bound to TiO $_2$ Nanoparticles As Accessed by ^{1} H NMR Spectroscopy. *J. Phys. Chem. B* **2016**, *120* (20), 4600–4607.

(112) Elhadj, S.; De Yoreo, J. J.; Hoyer, J. R.; Dove, P. M. Role of Molecular Charge and Hydrophilicity in Regulating the Kinetics of Crystal Growth. *Proc. Natl. Acad. Sci. U. S. A.* **2006**, *103* (51), 19237–19242.

(113) Boskey, A. L.; Maresca, M.; Ullrich, W.; Doty, S. B.; Butler, W. T.; Prince, C. W. Osteopontin-Hydroxyapatite Interactions in Vitro: Inhibition of Hydroxyapatite Formation and Growth in a Gelatin-Gel. *Bone Miner.* **1993**, *22* (2), 147–159.

(114) Shiraga, H.; Min, W.; Vandusen, W. J.; Clayman Ii, M. D.; Miner, D.; Terrell, C. H.; Sherbotie, J. R.; Foreman, J. W.; Przysiecki, C.; Neilson, E. G.; et al. Inhibition of Calcium Oxalate Crystal Growth in Vitro by Uropontin: Another Member of the Aspartic Acid-Rich Protein Superfamily. *Med. Sci.* **1992**, *89*, 426–430.

(115) Naka, K.; Chujo, Y. Control of Crystal Nucleation and Growth of Calcium Carbonate by Synthetic Substrates. *Chem. Mater.* **2001**, *13* (10), 3245–3259.

(116) Sollner, C.; Burghammer, M.; Busch-Nentwich, E.; Berger, J.; Schwarz, H.; Riekel, C.; Nicolson, T. Control of Crystal Size and Lattice Formation by Starmaker in Otolith Biomineralization. *Science (80-.).* **2003**, *302* (5643), 282–286.

(117) Sumper, M.; Kröger, N. Silica Formation in Diatoms: The Function of Long-Chain Polyamines and Silaffins. *J. Mater. Chem.* **2004**, *14*, 2059–2065.

(118) Weiner, S.; Addadi, L. Design Strategies in Mineralized Biological Materials. *J. Mater. Chem* **1997**, *7* (5), 689–702.

(119) Goobes, G.; Goobes, R.; Shaw, W. J.; Gibson, J. M.; Long, J. R.; Raghunathan, V.; Schueler-Furman, O.; Popham, J. M.; Baker, D.; Campbell, C. T.; et al. The Structure, Dynamics, and Energetics of Protein Adsorption—lessons Learned from Adsorption of Statherin to Hydroxyapatite. *Magn. Reson. Chem.* **2007**, *45* (S1), S32–S47.

(120) Masica, D. L.; Gray, J. J.; Shaw, W. J. Partial High-Resolution Structure of

Phosphorylated and Non-Phosphorylated Leucine-Rich Amelogenin Protein Adsorbed to Hydroxyapatite. *J. Phys. Chem. C* **2011**, *115*, 13775–13785.

(121) Makrodimitris, K.; Masica, D. L.; Kim, E. T.; Gray, J. J. Structure Prediction of Protein-Solid Surface Interactions Reveals a Molecular Recognition Motif of Statherin for Hydroxyapatite. *J. Am. Chem. Soc.* **2007**, *129*, 13713–13722.

(122) Ndao, M.; Ash, J. T.; Breen, N. F.; Goobes, G.; Stayton, P. S.; Drobny, G. P. A 13 C{ 31 P} REDOR NMR Investigation of the Role of Glutamic Acid Residues in Statherin-Hydroxyapatite Recognition. *Langmuir* **2009**, *25* (20), 12136–12143.

(123) Weidner, T.; Breen, N. F.; Li, K.; Drobny, G. P.; Castner, D. G. Sum Frequency Generation and Solid-State NMR Study of the Structure, Orientation, and Dynamics of Polystyrene-Adsorbed Peptides. *Proc. Natl. Acad. Sci.* **2010**, *107* (30), 13288–13293.

(124) Ndao, M.; Ash, J. T.; Stayton, P. S.; Drobny, G. P. The Role of Basic Amino Acids in the Molecular Recognition of Hydroxyapatite by Statherin Using Solid State NMR. *SUSC* **2010**, *604*, L39–L42.

(125) Brandt, E. G.; Lyubartsev, A. P. Molecular Dynamics Simulations of Adsorption of Amino Acid Side Chain Analogues and a Titanium Binding Peptide on the TiO 2 (100) Surface. *J. Phys. Chem. C* **2015**, *119*, 18126–18139.

(126) Gibson, J. M.; Popham, J. M.; Raghunathan, V.; Stayton, P. S.; Drobny, G. P. A Solid-State NMR Study of the Dynamics and Interactions of Phenylalanine Rings in a Statherin Fragment Bound to Hydroxyapatite Crystals. *J. Am. Chem. Soc.* **2006**, *128*, 5364–5370.

(127) Gibson, J. M.; Raghunathan, V.; Popham, J. M.; Stayton, P. S.; Drobny, G. P. A REDOR NMR Study of a Phosphorylated Statherin Fragment Bound to Hydroxyapatite Crystals. *J. Am. Chem. Soc.* **2005**, *127*, 9350–9351.

(128) Schlesinger, D. H.; Hay, D. I. Complete Covalent Structure of Statherin, a Tyrosine-Rich Acidic Peptide Which Inhibits Calcium Phosphate Precipitation from Human Parotid Saliva*. *J. Biol. Chem.* **1977**, *252* (5), 1689–1695.

(129) Moreno, E. C.; Kresak, M.; Hay, D. I. Adsorption of Molecules of Biological Interest onto Hydroxyapatite. *Calcif. Tissue Int.* **1984**, *36* (1), 48–59.

(130) Elgavish, G. A.; Hay, D. I.; Schlesinger, D. H. 1H and 31P Nuclear Magnetic Resonance Studies of Human Salivary Statherin. *Int. J. Pept. Protein Res.* **1984**, *23* (3), 230–234.

(131) Naganagowda, G. A.; Gururaja, T. L.; Levine, M. J. Delineation of Conformational Preferences in Human Salivary Statherin by 1 H, 31 P NMR and CD Studies: Sequential Assignment and Structure-Function Correlations. *J. Biomol. Struct. Dyn.* **1998**, *16* (1), 91–107.

(132) Raghunathan, V.; Gibson, J. M.; Goobes, G.; Popham, J. M.; Louie, E. A.; Stayton, P. S.; Drobny, G. P. Homonuclear and Heteronuclear NMR Studies of a Statherin Fragment Bound to Hydroxyapatite Crystals. *J. Phys. Chem. B* **2006**, *110*, 9324–9332.

(133) Douglas, W. H.; Reeh, E. S.; Ramasubbu, N.; Raj, P. A.; Bhandary, K. K.; Levine, M. J. Statherin: A Major Boundary Lubricant of Human Saliva. *Biochem. Biophys. Res. Commun.* **1991**, *180* (1), 91–97.

(134) Shaw, W. J.; Long, J. R.; Campbell, A. A.; Stayton, P. S.; Drobny, G. P. A Solid State NMR Study of Dynamics in a Hydrated Salivary Peptide Adsorbed to Hydroxyapatite. *J. Am. Chem. Soc.* **2000**, *122*, 7118–7119.

(135) Shaw, W. J.; Long, J. R.; Dindot, J. L.; Campbell, A. A.; Stayton, P. S.; Drobny, G. P. Determination of Statherin N-Terminal Peptide Conformation on Hydroxyapatite Crystals. *J. Am. Chem. Soc.* **2000**, *122*, 1709–1716.

(136) Best, S. M.; Duer, M. J.; Reid, D. G.; Wise, E. R.; Zou, S. Towards a Model of the Mineral–organic Interface in Bone: NMR of the Structure of Synthetic Glycosaminoglycan- and Polyaspartate-Calcium Phosphate Composites. *Magn. Reson. Chem.* **2008**, *46* (4), 323–329.
(137) Koutsopoulos, S.; Dalas, E. Inhibition of Hydroxyapatite Formation in Aqueous Solutions by Amino Acids with Hydrophobic Side Groups. *Langmuir* **2000**, *16*, 6739–6744.
(138) Bertani, P.; Raya, J.; Bechinger, B. 15N Chemical Shift Referencing in Solid State NMR. *Solid State Nucl. Magn. Reson.* **2014**, *61–62*, 15–18.

APPENDIX A

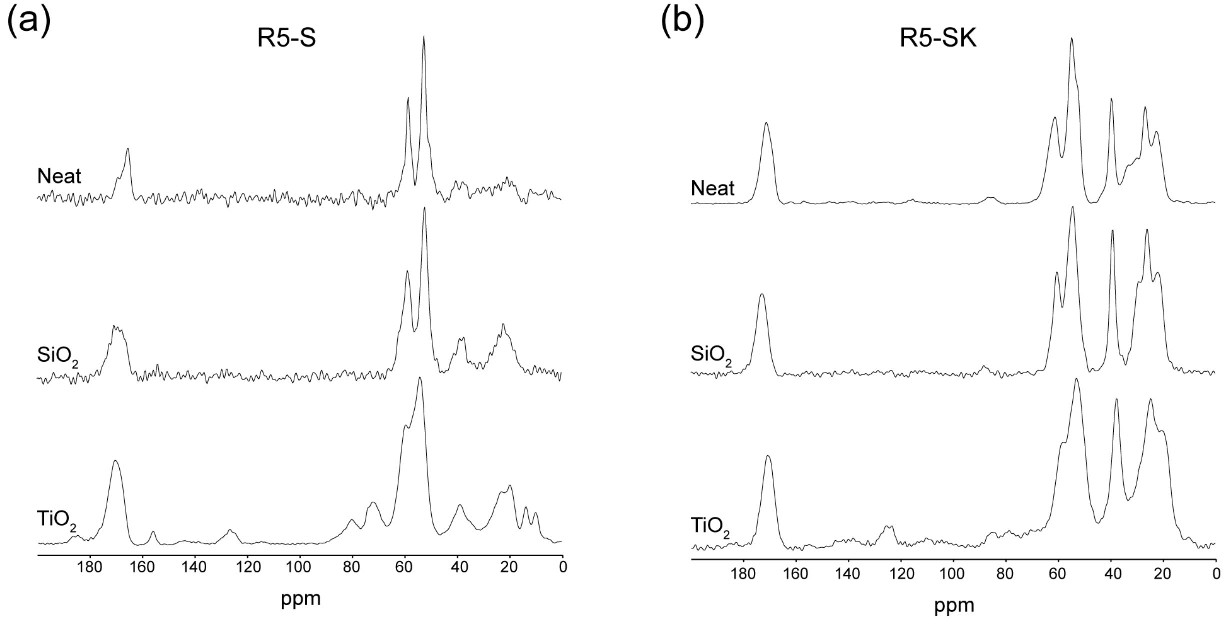

Figure A.1. Stacked 1D ^{13}C CP MAS spectra for (a) R5-S and (b) R5-SK in their neat, SiO$_2$, and TiO$_2$ co-precipitated forms.

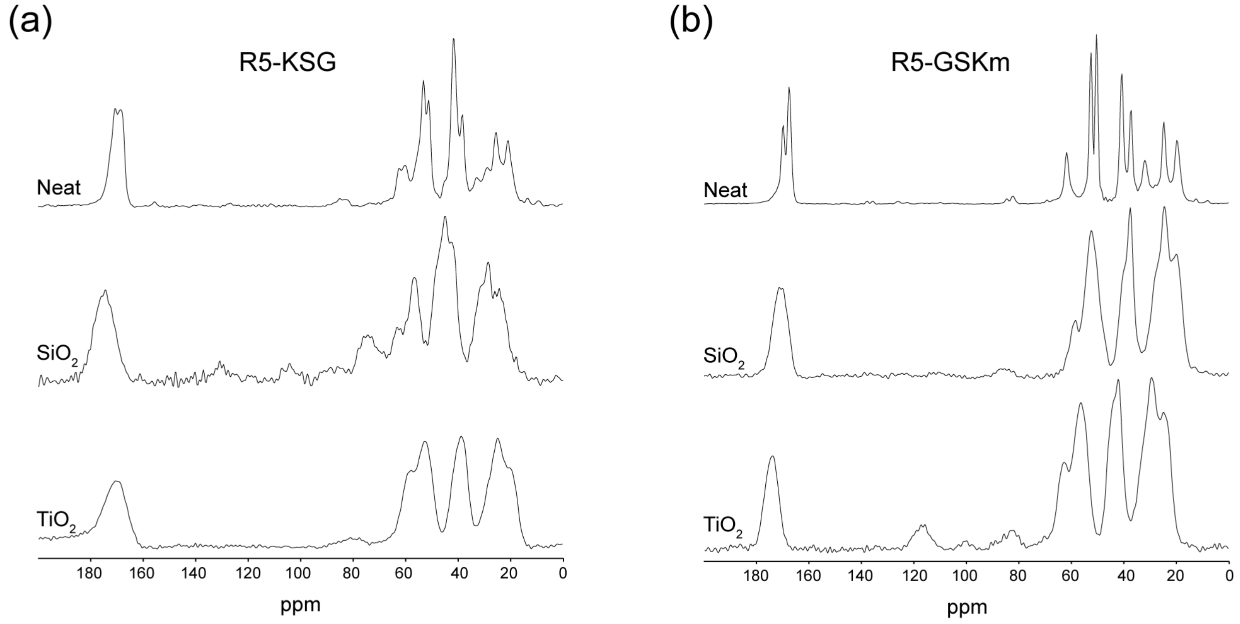

Figure A.2. Stacked 1D ^{13}C CP MAS spectra for (a) R5-KSG and (b) R5-GSKm in their neat, SiO$_2$, and TiO$_2$ co-precipitated forms.

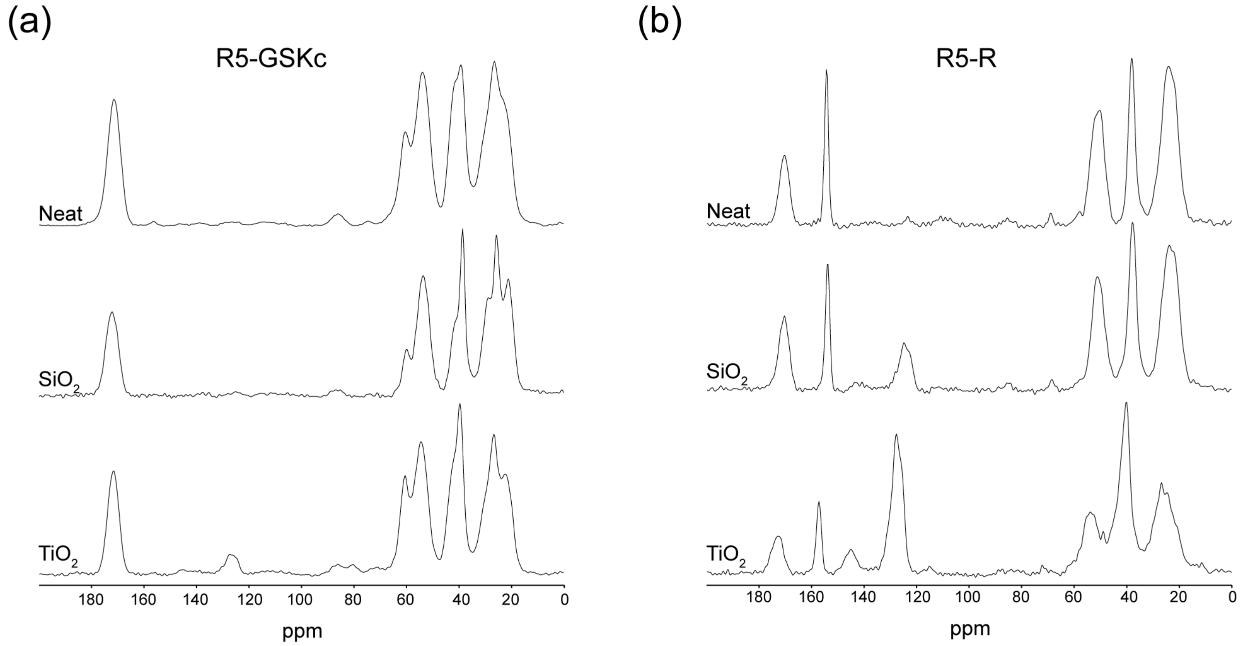

Figure A.3. Stacked 1D ^{13}C CP MAS spectra for (a) R5-GSKc and (b) R5-R in their neat, SiO$_2$, and TiO$_2$ co-precipitated forms.

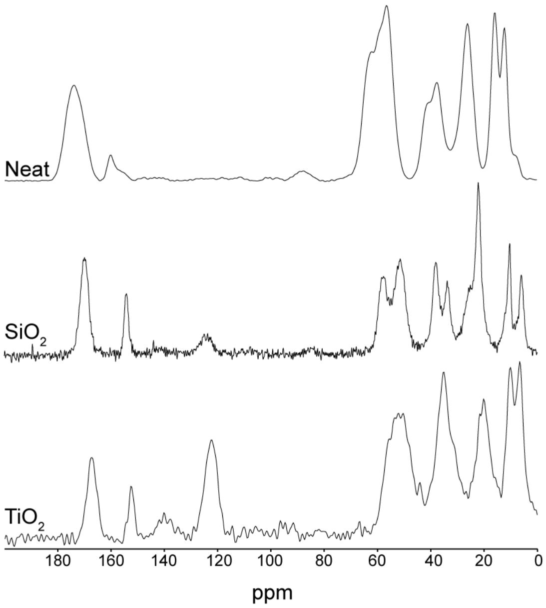

Figure A.4. Stacked 1D ^{13}C CP MAS spectra for R5-SRI in its neat, SiO_2, and TiO_2 co-precipitated forms.

Table A.1. ^{13}C chemical shift assignments for backbone residues in the neat R5 peptide.

Residue	**CO (ppm)**	**Cα (ppm)**	**Cβ (ppm)**
S1	165.6	52.6	58.7
S2	167.7	52.8	59.2
K3	169.1	37.6	27.9
K4	170.3	59.3	27.9
S5	168.5	61.5	64.7
G6	167.3	40.7	n/a
S7	169.7	56.5	59.4
S9	170.2	53.3	58.9
G10	167.0	40.8	n/a
S11	167.4	52.6	61.8
K12	169.8	50.4	32.0
G13	169.3	39.7	n/a
S14	167.4	58.9	73.1
K15	171.3	52.4	28.7
R16	170.7	50.7	24.5
R17	169.6	-	19.8
I18	164.3	55.5	34.4

Table A.2. ^{13}C chemical shift assignments for backbone residues in the R5-TiO_2 co-precipitate.

Residue	**CO (ppm)**	**Cα (ppm)**	**Cβ (ppm)**
S1	170.4	54.3	59.9
S2	170.9	53.4	58.6
K3	170.8	53.3	25.1
K4	173.1	53.7	27.9
S5	171.4	55.0	61.2
G6	169.5	42.2	n/a
S9	167.4	52.3	55.7
G10	169.5	40.0	n/a
S11	170.5	52.6	58.9
K12	171.6	51.8	33.0
G13	168.0	41.9	n/a
S14	169.3	59.2	60.5
K15	170.8	53.1	25.2
R16	172.9	53.9	26.9
R17	167.4	50.5	21.7
I18	167.4	53.8	35.3

Table A.3. ^{13}C chemical shift assignments for backbone residues in the R5-SiO_2 co-precipitate.

Residue	**CO (ppm)**	**Cα (ppm)**	**Cβ (ppm)**
S1	169.4	52.5	59.0
S2	173.4	52.8	58.8
K3	172.4	37.6	27.6
K4	171.3	52.2	24.1
S5	169.9	58.8	63.9
G6	168.1	40.5	n/a
S9	169.9	51.3	58.1
G10	169.8	40.2	n/a
S11	170.6	58.6	62.5
K12	171.4	55.3	28.1
G13	169.5	40.3	n/a
S14	171.0	58.9	-
K15	172.8	52.6	27.7
R16	169.5	50.3	22.9
R17	170.7	-	25.5
I18	170.3	52.3	34.2

Table A.4. ^{13}C chemical shift assignments for side-chain K and R residues in the neat R5 peptide.

Residue	**Cγ (ppm)**	**Cδ (ppm)**	**Cε (ppm)**	**Cζ (ppm)**
K3	20.4	24.8	31.3	n/a
K4	20.1	24.6	37.5	n/a
K12	19.8	24.8	37.4	n/a
K15	21.5	25.0	37.7	n/a
R16	22.8	38.6	n/a	154.7
R17	12.7	37.7	n/a	156.9

Table A.5. ^{13}C chemical shift assignments for side-chain K and R residues in the R5-TiO_2 co-precipitate.

Residue	**Cγ (ppm)**	**Cδ (ppm)**	**Cε (ppm)**	**Cζ (ppm)**
K3	20.7	25.2	38.1	n/a
K4	20.7	26.3	39.9	n/a
K12	19.7	25.9	38.1	n/a
K15	19.3	20.0	38.3	n/a
R16	24.7	40.2	n/a	157.6
R17	20.3	44.2	n/a	152.6

Table A.6. ^{13}C chemical shift assignments for side-chain K and R residues in the R5-SiO_2 co-precipitate.

Residue	**Cγ (ppm)**	**Cδ (ppm)**	**Cε (ppm)**	**Cζ (ppm)**
K3	20.4	24.4	29.5	n/a
K4	19.9	21.5	38.1	n/a
K12	20.2	24.8	37.8	n/a
K15	20.2	24.6	37.6	n/a
R16	21.2	36.9	n/a	152.9
R17	22.2	38.5	n/a	154.6

Table A.7. TALOS-N[38] –generated torsion angles for the neat R5 peptide obtained from experimental chemical shifts.

Residue	ϕ (deg)	ψ (deg)
S2	-82.9±29.1	113.6±43.3
K3	-87.4±18.4	55.2±56.8
K4	54.5±9.7	42.8±15.8
S5	-96.6±13.1	-26.3±12.6
G6	118.4±47.0	-177.3±12.8
S7	-81.2±9.0	104.4±22.0
Y8	-106.4±28.1	142.0±18.1
S9	-100.1±15.1	-11.8±17.2
G10	157.1±76.4	-172.8±15.4
S11	-115.5±38.3	138.3±28.8
K12	-135.0±13.3	154.5±8.0
G13	-142.5±38.6	174.1±24.2
S14	-145.7±9.2	147.1±9.2
K15	-106.7±11.7	124.6±11.5
R16	-114.7±25.3	137.5±25.3
R17	-99.5±18.9	122.6±18.1

Table A.8. TALOS-N[38] –generated torsion angles for R5-TiO_2 obtained from experimental chemical shifts.

Residue	**ϕ (deg)**	**ψ (deg)**
S2	-108.5±37.5	134.1±19.2
K3	58.4±5.4	40.2±8.5
K4	-88.9±10.2	98.0±23.6
S5	-146.1±9.8	155.7±11.9
G6	-177.6±26.5	-177.5±13.6
S9	-126.4±27.2	130.9±36.5
G10	-96.9±32.8	-159.8±32.1
S11	-87.6±14.4	97.6±16.6
K12	-116.3±27.3	97.6±59.6
G13	67.3±8.4	-130.4±14.0
S14	-96.7±13.8	2.2±23.0
K15	-113.7±19.7	152.2±17.1
R16	-104.3±22.3	128.9±17.1
R17	-90.0±9.5	108.4±15.7
I18	-102.9±15.1	130.1±12.1

Table A.9. TALOS-N[38] –generated torsion angles for R5-SiO_2 obtained from experimental chemical shifts.

Residue	**ϕ (deg)**	**ψ (deg)**
S2	-91.1±28.9	74.5±74.5
K3	-92.8±14.9	72.7±14.9
K4	-100.2±17.9	72.7±17.9
S5	-87.2±42.1	145.4±16.2
G6	-174.4±52.2	-177.4±13.8
S9	-106.9±18.9	114.6±37.8
G10	-159.5±59.5	-117.5±12.6
S11	-97.6±38.8	156.8±13.5
K12	-95.6±30.7	144.2±16.9
G13	92.6±14.4	-5.6±21.1
S14	-113.1±40.3	145.8±9.8
K15	-94.9±33.5	137.1±15.5
R16	-100.9±27.0	124.6±38.2
R17	-107.3±29.9	134.8±12.5
I18	-	-

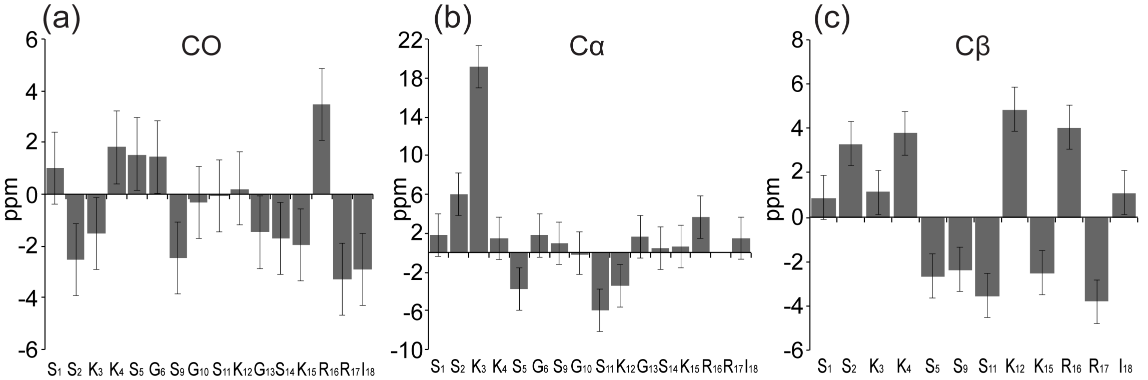

Figure A.5. Backbone ΔΔCS plots showing differences in chemical shift perturbations between the TiO_2 and SiO_2 systems for (a) ^{13}CO shifts, (b) ^{13}Cα shifts, and (c) ^{13}Cβ shifts. ΔΔCS are obtained by ΔCS(TiO_2)-ΔCS(SiO_2). ΔCS(TiO_2) and ΔCS(SiO_2) are the chemical shift perturbations obtained by subtracting the chemical shift of the ^{13}C spin in neat R5 from the corresponding ^{13}C shift in the R5-TiO_2 or R5-SiO_2 co-precipitate, respectively. A positive ΔΔCS corresponds to ΔCS(SiO_2) smaller than ΔCS(TiO_2), while a negative ΔΔCS corresponds to ΔCS(SiO_2) larger than ΔCS(TiO_2).

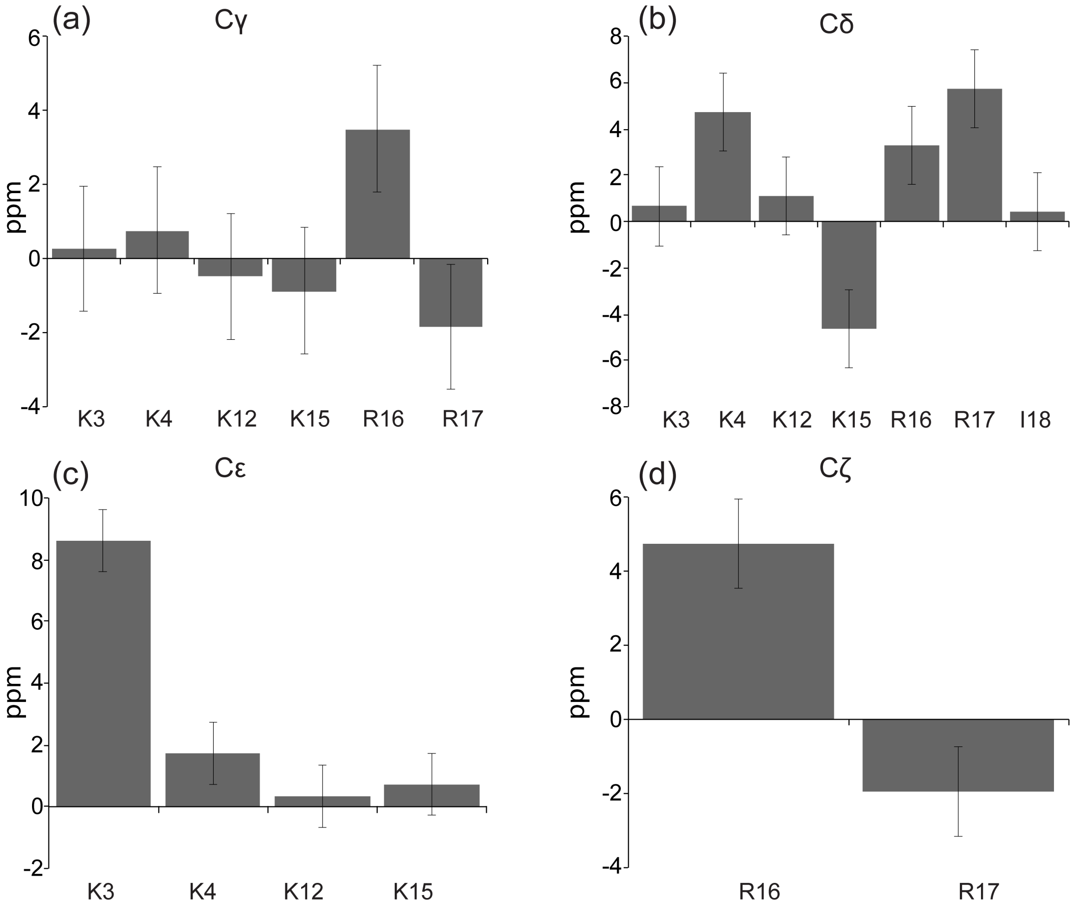

Figure A.6. Side-chain ΔΔCS plots showing differences in chemical shift perturbations between the TiO_2 and SiO_2 systems for (a) $^{13}C\gamma$ shifts, (b) $^{13}C\delta$ shifts, (c) $^{13}C\varepsilon$ shifts, and (d) $^{13}C\zeta$ shifts. ΔΔCS are obtained by ΔCS(TiO_2)-ΔCS(SiO_2). ΔCS(TiO_2) and ΔCS(SiO2) are the chemical shift perturbations obtained by subtracting the chemical shift of the ^{13}C spin in neat R5 from the corresponding ^{13}C shift in the R5-TiO_2 or R5-SiO_2 co-precipitate, respectively. A positive ΔΔCS corresponds to ΔCS(SiO_2) smaller than ΔCS(TiO_2), while a negative ΔΔCS corresponds to ΔCS(SiO_2) larger than ΔCS(TiO_2).

APPENDIX B

Peptide Design. The design of the S-K peptides used in the TiO_2-precipitation assay was based upon (1) the study of TiO_2-precipitating ability of R5 mutants and (2) work with K_n (n=2-5) peptides. While it is widely accepted that K residues play a vital role in initiating mineral precipitation, studies have shown that S residues are integral in the morphological control of the TiO_2 precipitate.[103] Therefore, we decided to include 2 or more S residues in each S-K peptide in the assay. Because S residues can be contiguous or separate in R5, we decided to test the affects of S placement on morphology in the S-K peptides. We designed peptides with contiguous S residues and then increased the number of K residues between them. Based upon our hypothesis that a greater number of lysine residues would help promote TiO_2 precipitation, we made the lysine residues more prevalent. The resulting K:S ratios range from 1.25-5.

We also observed TiO_2 precipitation from the K_5 peptide, but not from the K_2, K_3, or K_4 peptides. This led us to set our minimum peptide length at 5 residues. Our maximum length was set to 12 residues, as R5 has been shown to precipitate TiO_2 in a truncated mutant of 12 residues.[103]

The selection of peptides for further study was based upon amount of precipitate, morphology of the precipitate, and unique peptide primary structure.

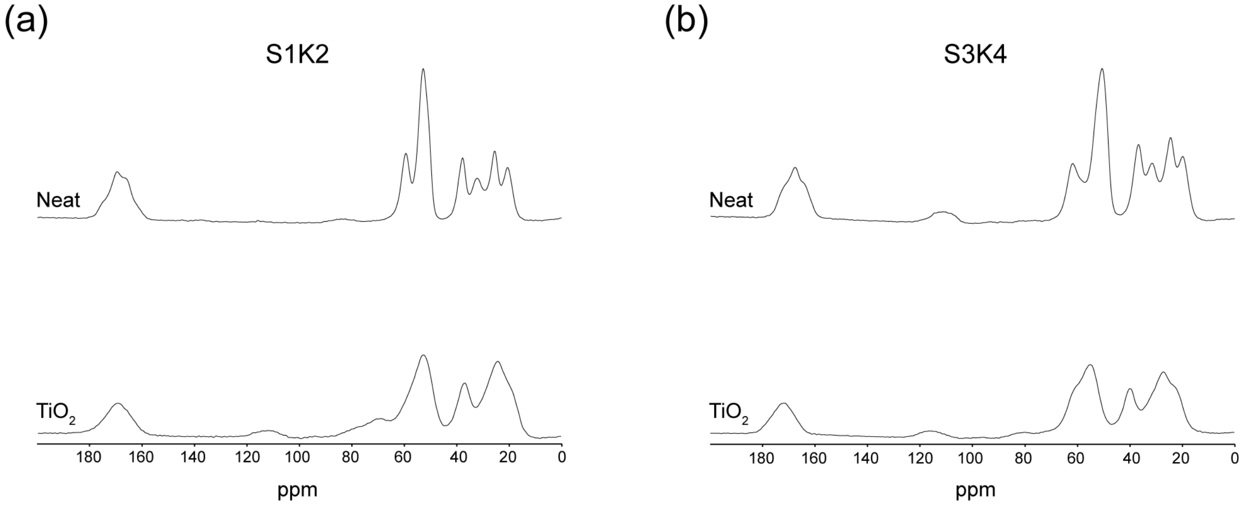

Figure B.1. Stacked 1D ^{13}C CP MAS spectra for (a) S1K2 and (b) S3K4 in their neat and TiO_2 co-precipitated forms.

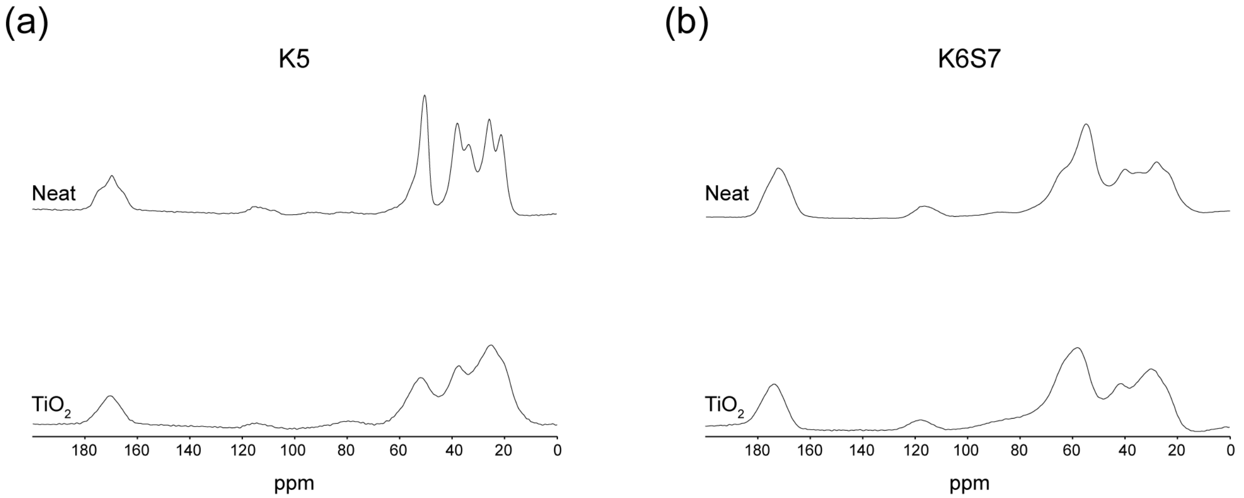

Figure B.2. Stacked 1D ^{13}C CP MAS spectra for (a) K5 and (b) K6S7 in their neat and TiO$_2$ co-precipitated forms.

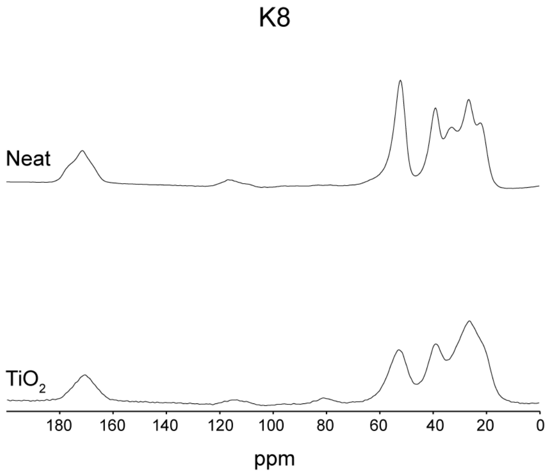

Figure B.3. Stacked 1D ^{13}C CP MAS spectra for K8 in its neat and TiO$_2$ co-precipitated form.

Table B.1. ^{13}C chemical shift assignments for backbone residues in the neat KSSKK peptide.

Residue	CO (ppm)	Cα (ppm)	Cβ (ppm)
K1	170.8	55.1	31.5
S2	170.7	55.2	62.7
S3	171.8	53.7	60.7
K4	176.3	53.6	29.1

Table B.2. ^{13}C chemical shift assignments for backbone residues in the KSSKK-TiO_2 co-precipitate.

Residue	**CO (ppm)**	**Cα (ppm)**	**Cβ (ppm)**
K1	170.5	53.5	29.8
S2	169.7	61.0	71.8
S3	171.2	58.1	61.1
K4	173.8	53.9	29.2

Table B.3. ^{13}C chemical shift assignments for side-chain residues in the neat KSSKK peptide.

Residue	**Cγ (ppm)**	**Cδ (ppm)**	**Cε (ppm)**
K1	23.4	28.0	40.7
K4	21.7	26.0	39.0

Table B.4. ^{13}C chemical shift assignments for side-chain residues in the KSSKK-TiO_2 co-precipitate.

Residue	**Cγ (ppm)**	**Cδ (ppm)**	**Cε (ppm)**
K1	21.5	26.8	39.7
K4	20.6	21.7	39.1

Table B.5. ^{13}C chemical shift assignments for backbone residues in the neat SKSK$_3$SKS peptide.

Residue	**CO (ppm)**	**Cα (ppm)**	**Cβ (ppm)**
S1	166.6	60.3	61.1
K2	170.0	53.8	33.3
S3	165.7	59.9	63.8
K4	169.9	52.5	33.5
K5	169.8	52.0	37.7
K6	175.1	51.3	38.6
S7	170.4	52.6	53.4
K8	171.5	52.3	33.2

Table B.6. ^{13}C chemical shift assignments for backbone residues in the SKSK$_3$SKS-TiO$_2$ peptide.

Residue	**CO (ppm)**	**Cα (ppm)**	**Cβ (ppm)**
S1	168.2	52.2	52.9
K2	169.3	51.9	24.1
S3	171.6	59.2	60.3
K4	174.1	53.8	26.9
K5	170.5	52.0	37.6
K6	173.9	54.0	39.6
S7	170.6	55.5	59.5
K8	170.8	52.9	37.9

Table B.7. ^{13}C chemical shift assignments for side-chain residues in the neat SKSK$_3$SKS co-precipitate.

Residue	Cγ (ppm)	Cδ (ppm)	Cε (ppm)
K2	21.3	26.6	39.0
K4	21.1	26.4	38.5
K5	22.4	26.9	39.1
K6	25.0	25.9	39.2
K8	22.2	26.6	39.1

Table B.8. ^{13}C chemical shift assignments for side-chain residues in the SKSK$_3$SKS-TiO$_2$ co-precipitate.

Residue	Cγ (ppm)	Cδ (ppm)	Cε (ppm)
K2	17.4	23.1	37.2
K4	19.9	25.8	39.1
K5	25.2	25.3	37.7
K6	28.1	28.2	39.6
K8	19.5	24.7	49.8

Table B.9. TALOS-N[38] –generated torsion angles for the neat KSSKK peptide obtained from experimental chemical shifts.

Residue	ϕ (deg)	ψ (deg)
S2	-107.0±23.3	133.5±19.0
S3	-92.7±9.2	105.2±18.4
K4	-86.9±9.3	92.1±12.2

Table B.10. TALOS-N[38] –generated torsion angles for the KSSKK-TiO_2 co-precipitate obtained from experimental chemical shifts.

Residue	**ϕ (deg)**	**ψ (deg)**
S2	-138.9±10.2	149.3±13.2
S3	-109.8±40.0	139.6±30.9
K4	-102.2±38.8	38.8±87.0

Table B.11. TALOS-N[38] –generated torsion angles for the neat $SKSK_3SKS$ peptide obtained from experimental chemical shifts.

Residue	**ϕ (deg)**	**ψ (deg)**
K2	-104.3±43.4	149.9±14.7
S3	-65.6±24.5	139.6±9.5
K4	-123.4±28.8	146.8±17.7
K5	-131.8±14.2	144.8±8.6
K6	-130.1±8.5	150.8±8.6
S7	-140.4±17.1	153.6±20.6
K8	-134.0±8.4	157.3±8.4

Table B.12. TALOS-N[38] –generated torsion angles for the SKSK$_3$SKS-TiO$_2$ co-precipitate obtained from experimental chemical shifts.

Residue	**ϕ (deg)**	**ψ (deg)**
K2	-83.5±14.6	-11.3±31.5
S3	-114.5±32.9	145.3±14.5
K4	-94.1±28.7	146.1±21.2
K5	-135.7±10.0	152.0±9.4
K6	-140.1±9.7	148.9±7.9
S7	-134.9±20.8	155.8±18.2
K8	-137.6±11.1	150.7±8.9

APPENDIX C

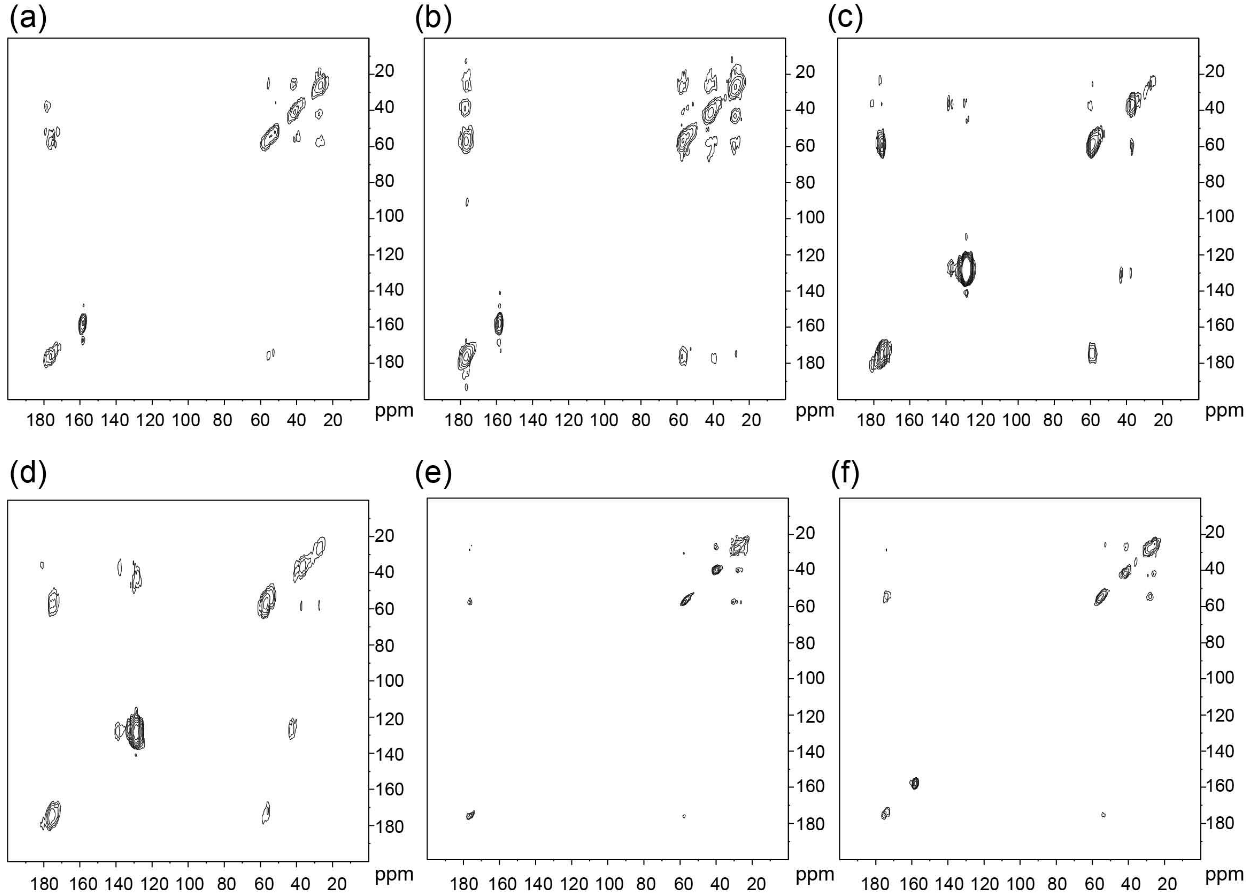

Figure C.1. ^{13}C-^{13}C DARR spectra of HAP-adsorbed (a) D2R9, (b) D3R10, (c) E4F7, (d) E5F14, (e) K6, and (f) R13.

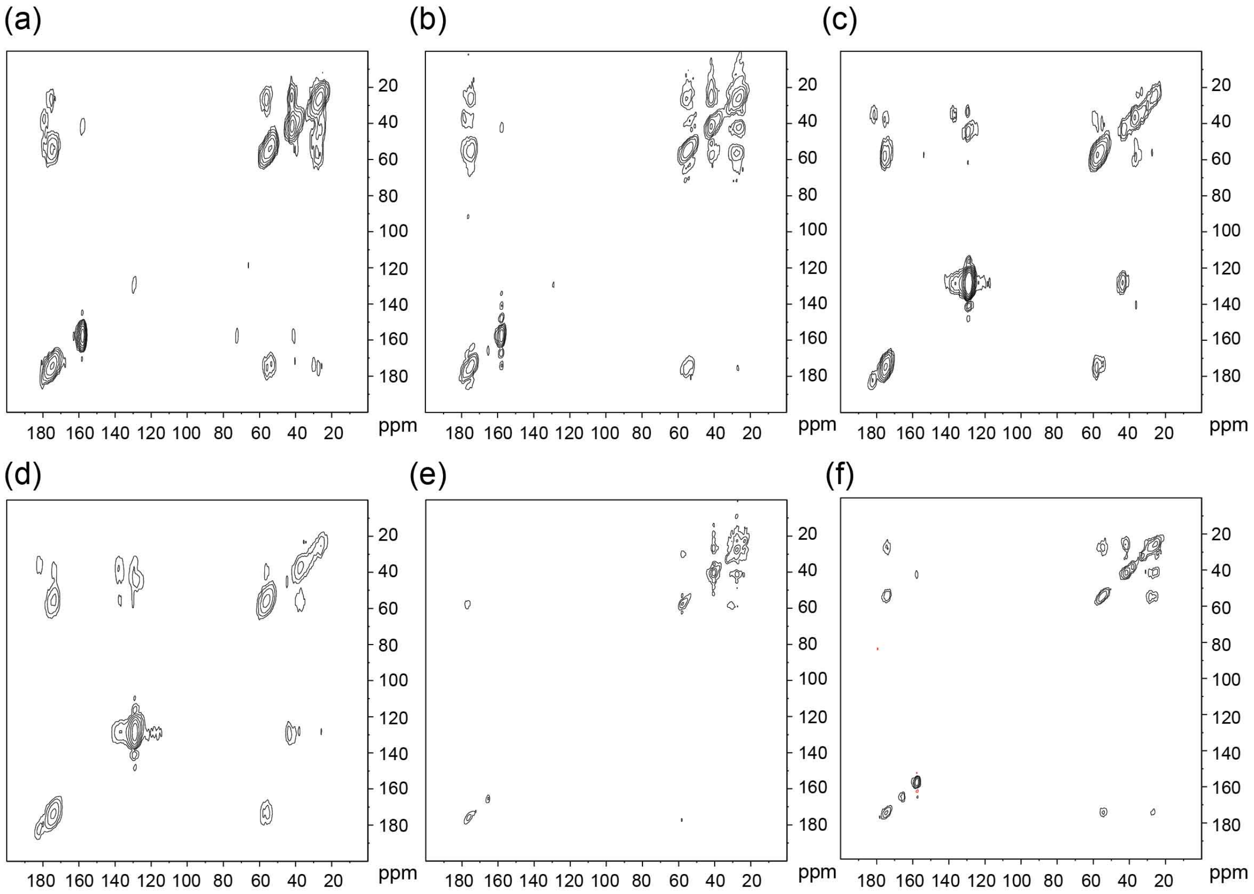

Figure C.2. ^{13}C-^{13}C DARR spectra of SiO_2-adsorbed (a) D2R9, (b) D3R10, (c) E4F7, (d) E5F14, (e) K6, and (f) R13.

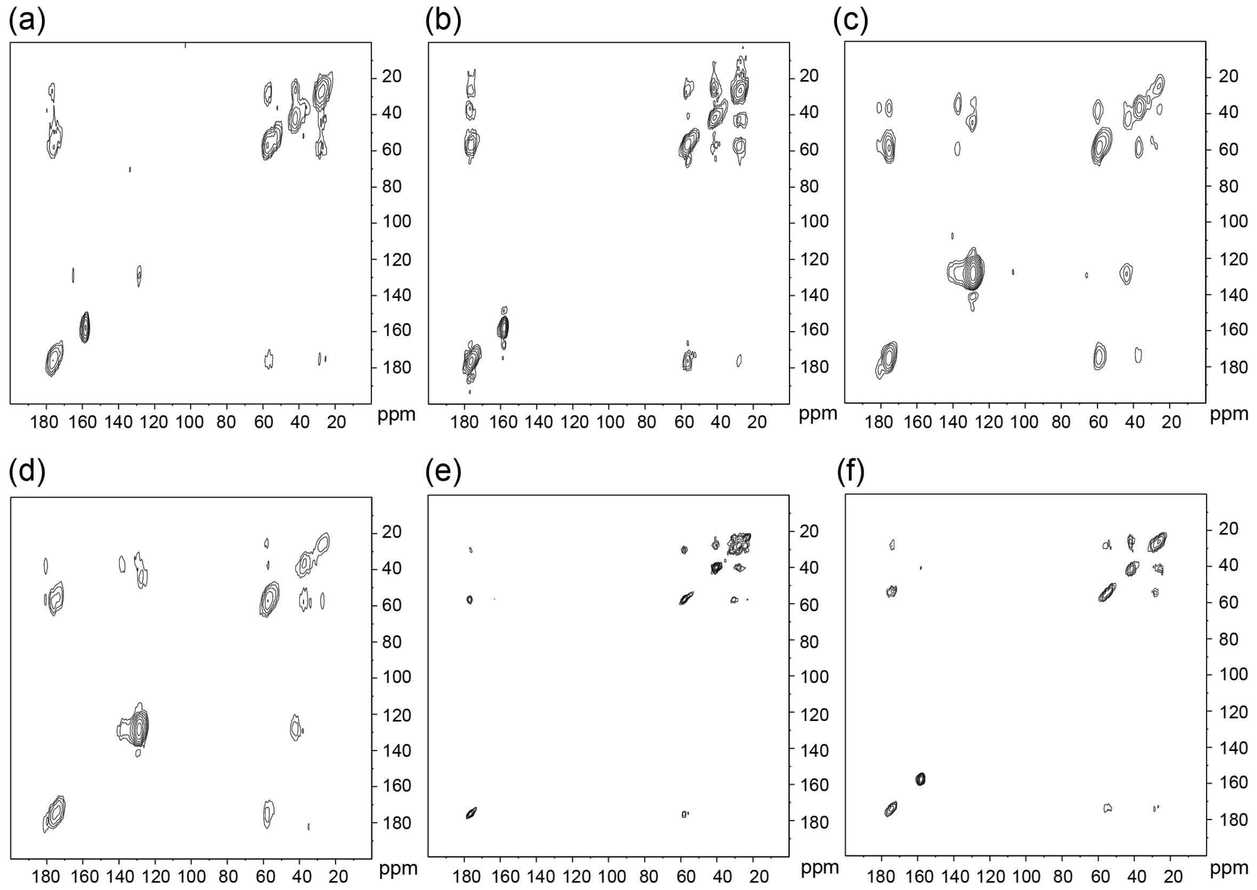

Figure C.3. ^{13}C-^{13}C DARR spectra of TiO_2-adsorbed (a) D2R9, (b) D3R10, (c) E4F7, (d) E5F14, (e) K6, and (f) R13.

Table C.1. ^{13}C chemical shift assignments for backbone residues in the neat SNa15 peptide.

Residue	**CO (ppm)**	**Cα (ppm)**	**Cβ (ppm)**
D2	174.1	51.1	36.1
D3	175.1	51	35.9
E4	176.4	58.4	26.8
E5	176.3	57.2	25.9
K6	175.8	58.4	31.3
F7	175.3	60.4	37.4
R9	176.4	57.9	28.1
R10	176.5	58.9	28.4
G12	168.4	39.3	n/a
R13	174.8	56.4	28.6
F14	174	55.8	37.3

Table C.2. ^{13}C chemical shift assignments for backbone residues in the HAP-adsorbed SNa15 peptide.

Residue	**CO (ppm)**	**Cα (ppm)**	**Cβ (ppm)**
D2	176.4	52.1	40.6
D3	177.6	54	39.1
E4	175.6	59.6	25.3
E5	176.2	59.2	27.8
K6	176	57.6	28.6
F7	175.3	59.6	37.4
R9	174.6	54.2	27.5
R10	177.2	57.2	27.7
G12	172.9	43.2	n/a
R13	174.6	55.2	27.8
F14	178.6	58.6	37.4

Table C.3. ^{13}C chemical shift assignments for backbone residues in the SiO_2-adsorbed SNa15 peptide.

Residue	CO (ppm)	Cα (ppm)	Cβ (ppm)
D2	174.9	53.7	38.3
D3	176.4	51.2	37.8
E4	175.4	58	27.1
E5	174.5	55.8	26.1
K6	176.2	57.7	30.9
F7	177.9	60.4	34.6
R9	175.4	56.3	28.4
R10	175.9	55.1	26.9
G12	173	43.1	n/a
R13	174.4	54.7	28.5
F14	173.8	55	37.2

Table C.4. ^{13}C chemical shift assignments for backbone residues in the TiO_2-adsorbed SNa15 peptide.

Residue	CO (ppm)	Cα (ppm)	Cβ (ppm)
D2	172.8	53.5	39
D3	175.3	56.8	39.9
E4	175	59.5	26.8
E5	175.5	57.6	27.4
K6	175.7	58.2	30.9
F7	175.7	59.7	35.6
R9	176.4	57.9	28.5
R10	176.6	58.4	27.6
G12	173.2	43.4	n/a
R13	174.3	55.4	28.5
F14	174.3	54.2	37.1

Table C.5. ^{13}C chemical shift assignments for side-chain residues in the neat SNa15 peptide.

Residue	Cγ (ppm)	Cδ (ppm)	Cε (ppm)	Cζ (ppm)
D2	177.2	n/a	n/a	n/a
D3	176.7	n/a	n/a	n/a
E4	30.5	177.3	n/a	n/a
E5	30.9	176.8	n/a	n/a
K6	24.2	28.1	40.7	n/a
F7	136.8	129.7	129.5	129.3
R9	27.3	42.3	n/a	158
R10	26.8	42.4	n/a	157.6
R13	27.5	42.5	n/a	157.8
F14	137.8	129.7	129.3	129.3

Table C.6. ^{13}C chemical shift assignments for side-chain residues in the HAP-adsorbed SNa15 peptide.

Residue	Cγ (ppm)	Cδ (ppm)	Cε (ppm)	Cζ (ppm)
D2	178.4	n/a	n/a	n/a
D3	178	n/a	n/a	n/a
E4	37.1	180.4	n/a	n/a
E5	37.1	181.1	n/a	n/a
K6	23.9	27.4	39.7	n/a
F7	137.4	129.3	128.5	128.5
R9	26.1	42	n/a	158.3
R10	26.1	43.3	n/a	158.1
R13	25.8	41.6	n/a	158.1
F14	139.4	129.5	129.5	129.5

Table C.7. ^{13}C chemical shift assignments for side-chain residues in the SiO_2-adsorbed SNa15 peptide.

Residue	**Cγ (ppm)**	**Cδ (ppm)**	**Cε (ppm)**	**Cζ (ppm)**
D2	179.2	n/a	n/a	n/a
D3	178.7	n/a	n/a	n/a
E4	36.2	181.8	n/a	n/a
E5	38.1	182.1	n/a	n/a
K6	22.7	27.5	40.6	n/a
F7	136.7	129.5	129.3	128.8
R9	27.2	42.7	n/a	158.1
R10	26	41.7	n/a	157.5
R13	25.5	41.6	n/a	157.5
F14	136.9	129.6	128.3	128.1

Table C.8. ^{13}C chemical shift assignments for side-chain residues in the TiO_2-adsorbed SNa15 peptide.

Residue	**Cγ (ppm)**	**Cδ (ppm)**	**Cε (ppm)**	**Cζ (ppm)**
D2	177.9	n/a	n/a	n/a
D3	177.1	n/a	n/a	n/a
E4	37.1	181.3	n/a	n/a
E5	37.7	180.6	n/a	n/a
K6	24.7	27.9	40.3	n/a
F7	137.5	129.8	129	129
R9	26.7	42.1	n/a	158.4
R10	26.1	43	n/a	158.2
R13	25.6	41.3	n/a	158.1
F14	138.7	130.1	129.3	128.2

Table C.9. ^{15}N chemical shift assignments for side-chain residues in the neat SNa15 peptide.

Residue	**Nε (ppm)**	**NH (ppm)**	**Nζ (ppm)**
K6	n/a	n/a	33.7
R9	85.1	72.9	n/a
R10	85.7	73.1	n/a
R13	85.4	72.9	n/a

Table C.10. ^{15}N chemical shift assignments for side-chain residues in the HAP-adsorbed SNa15 peptide.

Residue	**Nε (ppm)**	**NH (ppm)**	**Nζ (ppm)**
K6	n/a	n/a	34.6
R9	85	75.2	n/a
R10	83.6	73.7	n/a
R13	85.7	73.1	n/a

Table C.11. ^{15}N chemical shift assignments for side-chain residues in the SiO_2-adsorbed SNa15 peptide.

Residue	**Nε (ppm)**	**NH (ppm)**	**Nζ (ppm)**
K6	n/a	n/a	33.9
R9	85.9	74.2	n/a
R10	85.3	72.6	n/a
R13	85.4	72.2	n/a

Table C.12. ^{15}N chemical shift assignments for side-chain residues in the TiO_2-adsorbed SNa15 peptide.

Residue	**Nε (ppm)**	**NH (ppm)**	**Nζ (ppm)**
K6	n/a	n/a	33.9
R9	85.3	76.4	n/a
R10	84.7	74.5	n/a
R13	85	73.6	n/a

Table C.13. TALOS-N[38] –generated torsion angles for the neat SNa15 peptide obtained from experimental chemical shifts.

Residue	**ϕ (deg.)**	**Ψ (deg.)**
D3	-99±14.9	61.7±31.2
E4	-59.7±4	-41.9±7.1
E5	-62.4±4.9	-39.1±6.7
K6	-63.8±9.3	-40.5±8.6
F7	-63.9±7.1	-40.4±8.7
L8	-66±5.6	-36.8±8.1
R9	-63.1±5.4	-34.6±5.4
R10	-69.3±7.5	-28.1±8.6
I11	-90.2±16.3	-20.8±15.6
G12	88.9±15.8	-168±22.6
R13	-82.8±27.5	137.1±10.3
F14	-84±10.4	123±12.9

Table C.14. TALOS-N[38] –generated torsion angles for the HAP-adsorbed SNa15 peptide obtained from experimental chemical shifts.

Residue	**ϕ (deg.)**	**Ψ (deg.)**
D3	-53.2±61.2	162.2±33.6
E4	62.8±8.8	27.5±12.4
E5	-57±23	-34±17
K6	-62.4±6	-38.1±9
F7	-69.3±6.7	-33.5±8.7
L8	-82.1±15.2	-12.6±16.6
R9	-77.2±14.7	-7.8±37.9
R10	-90.3±24.2	-19.1±24.1
I11	-75.7±14.1	-26.9±20
G12	92.4±19.2	-164.7±20.9
R13	-78.7±13.4	110.4±21.3
F14	-65.3±7.8	138.6±10.2

Table C.15. TALOS-N[38] –generated torsion angles for the SiO_2-adsorbed SNa15 peptide obtained from experimental chemical shifts.

Residue	**ϕ (deg.)**	**Ψ (deg.)**
D3	-98.5±9.2	16.2±17.8
E4	57.7±6.7	39.8±8.4
E5	-95.1±19.6	81.1±23.3
K6	-62.4±7	-35.2±8.3
F7	-61.7±4.6	-30.6±7.9
L8	-66.2±5.7	-27.2±7.9
R9	-81.1±12.9	-5.8±11.6
R10	-87.3±15.9	53.6±65.2
I11	-103.1±22.1	139.5±13.2
G12	-114.1±20.4	159.9±19.9
R13	-82.9±13.7	129±13.7
F14	-88.8±8.6	118.6±12.3

Table C.16. TALOS-N[38] –generated torsion angles for the TiO_2-adsorbed SNa15 peptide obtained from experimental chemical shifts.

Residue	**ϕ (deg.)**	**Ψ (deg.)**
D3	-73.7±17	-22.8±29.2
E4	-69.3±13	-34.3±19.5
E5	-69±13	-25.2±45.1
K6	-60±5.6	-35±6.2
F7	-68.4±7.7	-33.5±11.8
L8	-64.9±7.9	-35.1±9.4
R9	-63.3±6.3	-30.6±9.2
R10	-74.9±11.8	-21.9±16.9
I11	-82.9±19.3	-21.8±19.6
G12	88.2±15.8	-166.7±24.9
R13	-75±12.3	131.8±10.1
F14	-90.7±9.1	115.5±15.4

VITA

Erika Buckle is from Boxborough, Massachusetts. She graduated with her B.A. in Chemistry and a Minor in Mathematics from Wellesley College in 2012. While attending Wellesley College, she conducted research with Professor David Haines and participated in an NSF-REU program at Duke University with Professor Jiyong Hong. After graduation, she moved to Seattle, Washington to work towards her Ph.D in Chemistry at the University of Washington, where she conducted research with Professor Gary Drobny.